GAIN RESOLUTION STUDIES AND FIRST DARK MATTER SEARCH WITH NOVEL 3D NUCLEAR RECOIL DETECTORS

A THESIS SUBMITTED TO THE GRADUATE DIVISION OF THE UNIVERSITY OF HAWAIʻI AT MĀNOA IN PARTIAL FULFILLMENT OF THE REQUIREMENTS FOR THE DEGREE OF

DOCTOR OF PHILOSOPHY

IN

PHYSICS

DECEMBER 2018

By

Thomas Thorpe

Thesis Committee:

Sven Vahsen, Chairperson
Thomas Browder
Jason Kumar
Philip Von Doetinchem
Jonathan Williams

Keywords: directional dark matter detection, 3D vector tracking, head-tail, nuclear recoils, Fano factor, avalanche gain, gain resolution, gas detectors, GEMs

To my parents:

I understand that it was probably never clear what I would do in life,
and maybe it still isn't.
But, I think everything will work out.

ACKNOWLEDGMENTS

There are many people without whose support, whether directly or indirectly, this thesis would not have been possible. I am grateful to my advisor, Sven Vahsen, whose drive and eternal optimism have helped me keep focus throughout the years. I would like to thank the BEAST II collaboration, as the work in chapter five was produced with data from their phase 2 run. Specifically, Jeffrey Schueler for recording and preparing the data sets, and Peter Lewis, Michael Hedges, and Ilsoo Seong for work on the analysis.

Additionally, I would like to thank Jason Kumar and Patrick Stengel for their useful guidance concerning dark matter. And I would like to thank my committee for their feedback and patience during this process. I would also like to thank Xerxes Tata for his perseverance in teaching me quantum mechanics, I know more now than I did before. Finally, I would like to thank my friends and family, who hopefully realize that there is a reason why I have been ignoring them.

To my Mom, Frances Thorpe, thank you for all your support. This wouldn't have happened without it and I am grateful. To my Dad, Elmer Thorpe, thank you for teaching me about working hard. It has been put to good use.

ABSTRACT

Dark matter remains one of nature's cruelest puzzles and a world wide effort has been underway for many years to directly detect it in the laboratory. To date, however, no convincing signal has been observed. The race is on to figure out novel and better ways of detecting it, which will be the topic of this thesis. Traditional terrestrial detectors measure the energy and arrival time of interactions, but more information exists. If the angular distribution of the events resulting from these interactions could also be measured then this could be used to prove, unambiguously, the cosmological origin of dark matter. This directional detection is gaining traction and R&D efforts exist around the world. We present some of our own R&D efforts with small prototype gas Time Projection Chambers (TPCs) with Gas Electron Multiplier (GEM) charge amplification, and high resolution 3D pixel charge readout. These include gain and gain resolutions measurements with multiple GEM stages and various gases including our first gain measurements with Sulfur Hexafluoride (SF_6), a Negative Ion (NI) gas. The advantages of a high-gain/low-noise detector are discussed and some remarks about the target gas choice in future detectors are made. We also unveil our first WIMP-nucleon scattering cross limit obtained from a series of small TPCs and discuss what still needs to be done, including using the measured event angular distribution, to improve our limit. Finally, we discuss our result in the context of the direct, and directional, communities by anticipating future larger directional dark matter detectors.

TABLE OF CONTENTS

LIST OF TABLES

LIST OF FIGURES

CHAPTER 1
INTRODUCTION

The nature of dark matter remains one of the biggest puzzles in particle physics today. Our current understanding of the universe holds that the energy density is roughly composed as follows: 68% dark energy, 27% dark matter, and 5% baryonic matter [73]. To date, all evidence for dark matter has been through its gravitational effects. But if the dark matter consists of particles we can devise ways of detecting these particles, and, generally, three categories of detection are described: 1) Indirect detection, which involves measuring the standard model (SM) products produced by dark matter (DM) interacting with itself. 2) Collider searches, which involve measuring the "missing" energy carried off by dark matter created by colliding standard model particles. 3) Direct detection, which will be the focus of this thesis.

Direct detection involves building a vessel and filling it with a target material that the dark matter will interact with, causing target nuclei to recoil. These recoils are the result of the relative velocity between the detector target and the dark matter, as the Earth moves through the galactic dark matter halo. The cross section of a dark matter particle scattering off a detector target nucleus is very small, so these detectors must have extremely low background rates in order to measure an interaction. In addition to being manufactured from very low-radioactivity components these detectors are also placed underground to reduce the backgrounds induced by cosmic rays. Shielding is added outside of the detector to reduce the backgrounds from neutron and gamma rays. Some detectors consist of multiple detectors inside one another, like a complicated matryoshka doll, to actively veto background processes. Then, at the analysis level, a background-free fiducial region still needs to be selected from within the active region to look for a possible signal. This is not an easy task but detectors like this are currently operating around the world [11] [19] [8] [31] [41] [15] [111].

Generally these detectors measure the time that an event occurs and the energy of that event, however more information exists. If a detector can measure the angular distribution of the recoiling nuclei it records in addition to the time and energy, then this information could be used to constrain the direction the source is coming from. Due to the galactic disk motion through the dark matter halo, a highly anisotropic signal is predicted that no terrestrial background can mimic. In order to measure such a directional signal, directional detectors are needed. After a brief introduction to Weakly Interacting Particle (WIMP) dark matter, these detectors are the topic of this thesis.

Our detectors are gaseous Time Projection Chambers (TPCs) that use Gas Electron Multipliers (GEMs) for charge amplification and pixel charge readout electronics. This high-gain/low-noise combination allows for high resolution vector 3D ionization distribution measurements. This thesis goes into the detail of the gain and gain resolution of GEM-based detectors by studying different gain stages and different gases. In doing so, a heuristic model is developed, with the aid of various

historical formulae found in the literature, which allows for the description of the gain of any GEM-based detector over a wide range of operational parameter space, including different numbers of GEMs, various GEM avalanching electric field strengths, and a wide range of gas pressures.

The gain resolution is also discussed in some detail, and its crucial role in determining the energy resolution of a GEM-based detector is presented. We then put this into context within the directional detection field, where we discuss the unique features that directional detectors possess, which are dependent on the gain resolution. The most powerful particle dark matter signal, the dipole signal which is discussed in Sec. 2.3.2, can only be measured by detectors with directional sensitivity and is considered the "smoking gun" for confirming particle dark matter of cosmological origin. In order to fully exploit the dipole signal, the directional detector needs to be able to measure in which direction a given recoiling nucleus is traveling. Discriminating the nucleus's direction of travel is called the head-tail measurement, or signal, and it is discussed in Sec. 2.3.1. To emphasize the importance of the gain resolution we briefly note that in order for a detector to effectively measure the head-tail signal, the detector must possess an energy resolution that is good enough to discriminate whether more charge exists in one portion of an ionization distribution than in another.

We also present our first gain measurements with Sulfur Hexafluoride (SF_6), a Negative Ion (NI) gas, and discuss the implications of these measurements within the context of the directional detection field. The results of the gain for electron and NI gases are also compared and discussed as they relate to the design considerations of future larger detectors. Finally, 3D ionization distribution measurements, obtained with our TPCs using ATLAS pixel chips, are used to set our first Spin Independent WIMP-nucleon scattering cross section upper limit. We discuss what still needs to be done and provide an outlook should these detectors be produced on a large scale.

CHAPTER 2
DARK MATTER AND ITS DETECTION

2.1 Dark matter

People have known about the existence of dark matter for nearly a century and yet no one knows the exact nature of it. This elusiveness only serves to drive physicists to come up with more sophisticated ways to detect it. What we do know is that it does not seem to interact electromagnetically, however there exists an abundance of cosmological and gravitational evidence of its existence. This chapter will briefly go over some of that evidence, followed by a discussion of how dark matter is detected terrestrially, directional detection, and some relevant detector physics.

2.1.1 Evidence

Gravitational evidence

Gravitational evidence for the existence of dark matter exists on vastly different scales. Back in the 1930s Zwicky used an 18" telescope to observe the Coma cluster, which consists of ≈ 1000 galaxies, and carried out a Doppler shift study [113]. Assuming that the system was virialized, he estimated the mass, and found that it must be much larger, $\sim \times 100$, than the value given by using light estimates. He called this non-lumious matter dark matter. On galactic scales it causes rotation curves to flatten off with increasing radius, see Fig. 2.1. Considering only the visible matter leads to the conclusion that the rotational velocity should decrease as the distance from the center is increased:

$$v \sim \sqrt{\frac{M(r)}{r}} \tag{2.1}$$

where $M(r)$ the mass enclosed within a radius, r. Thus if the mass density decreases as a function of r so should the rotational velocity, but Fig. 2.1 shows that the velocity becomes constant owing to some additional, non-luminous, matter.

Perhaps the most famous image including evidence for dark matter is that of the Bullet cluster, [39] see Fig. 2.2. The bullet cluster is actually two galactic clusters colliding, and the diffuse gas clouds associated with each cluster interact, heat up, and generate massive amounts of X-rays the pink areas in Fig. 2.2. By observing these X-rays, astronomers are able to locate where most of the baryonic matter is located, that is the matter that generates the X-rays when interacting with itself. The name Bullet cluster comes from the area of pink which has deformed into "shock-wave" on the right due to the high amount of interaction between the gas clouds.

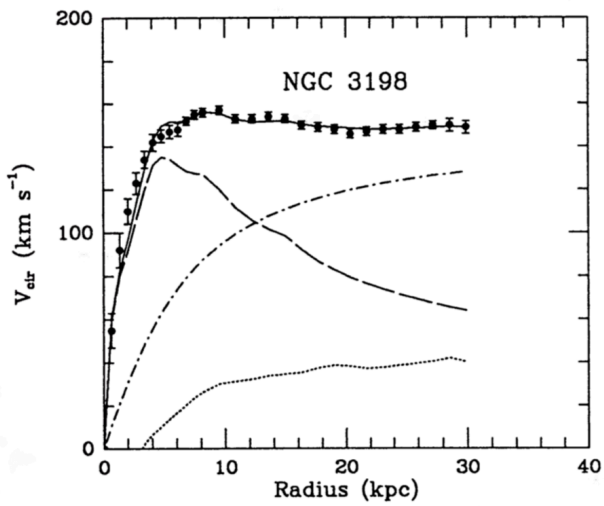

Figure 2.1: Galactic rotation curve for NGC 3198, Taken from Ref. [27]. The points are measured rotation velocities as function of distance from the center. The dotted, dashed, and dot-dash lines are contributions from the gas, galactic disk, and dark halo, respectively.

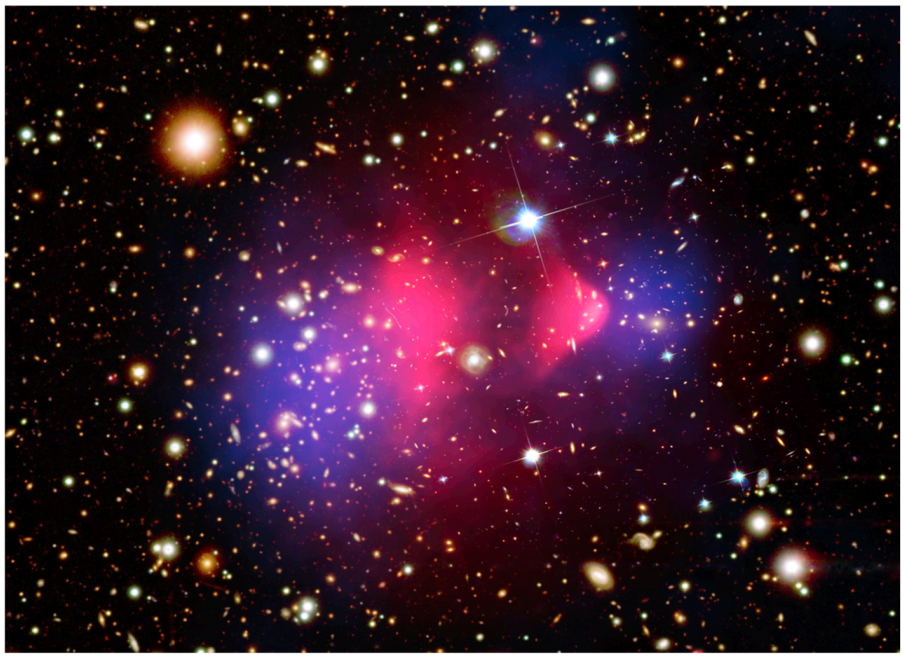

Figure 2.2: Composite image of the Bullet cluster. Pink areas are X-rays produced from the merging gas clouds indicating high density areas of gas. Blue areas are the dark matter distributions created from weak gravitational lensing surveys.

To realize the importance of this image, we must understand the blue areas which were created using the effect of weak gravitational lensing. Essentially, the large amount of mass in the merging clusters will distort the images we see of distant light sources located on the other side, behind, the clusters. Since we know how the distortion works, via general relativity, we can then correct for this effect and map out how this "distorting" matter is distributed. This matter distribution is the blue areas, and so there exists some other matter that does not contribute to the X-ray production in the way the gas clouds do. Another way to say this is this other matter distribution does not interact, or produce, light, and is "dark".

The Cosmic Microwave Background (CMB) and ΛCDM

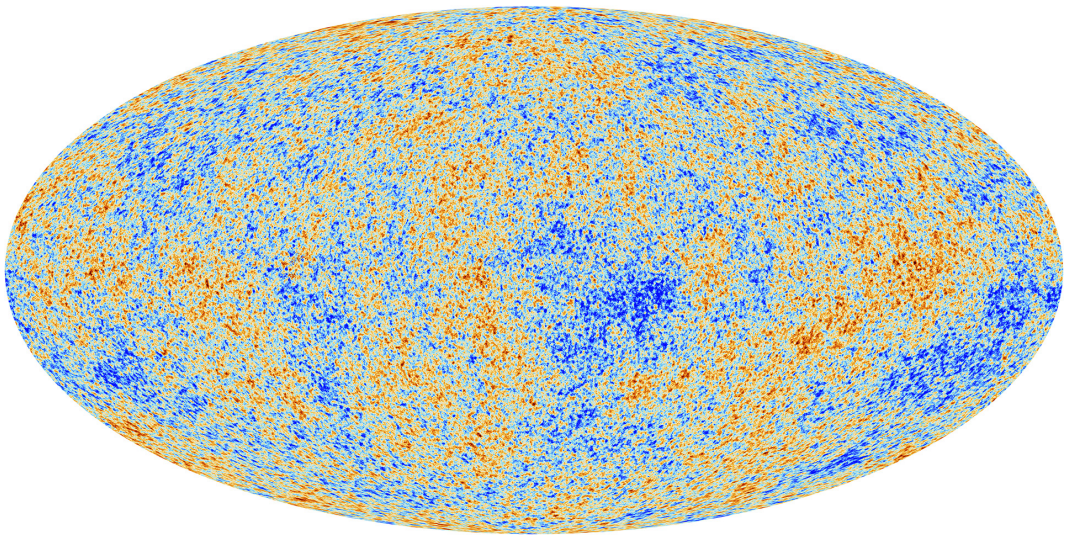

Figure 2.3: The Cosmic Microwave Background (CMB) radiation. The color corresponds to temperature. Taken from Ref. ESA and the Planck collaboration.

The Cosmic Microwave Background (CMB) radiation was first discovered by Penzias and Wilson in 1968, and they received the Nobel Prize for their discovery in 1978 as it changed how we view the history of the Universe. The Λ Cold Dark Matter (ΛCDM) model parameterizes the cosmological history of the Universe in terms of a cosmological constant, Λ, which is associated with dark energy and the expansion, and Cold Dark Matter, which consists of non-relativistic, cold, dark matter. The success of this model has earned it the name of the standard model of cosmology. It should be noted that ΛCDM assumes general relativity to be correct, and there are other models which rely on theories of modified gravity or MOdified Newtonian Dynamics (MOND), however this thesis is focused on the cold dark matter.

Briefly, once the Universe becomes ≈ seconds old various composite particles are allowed to form and, based on their nature, will decouple at different times with the weakly interacting decoupling

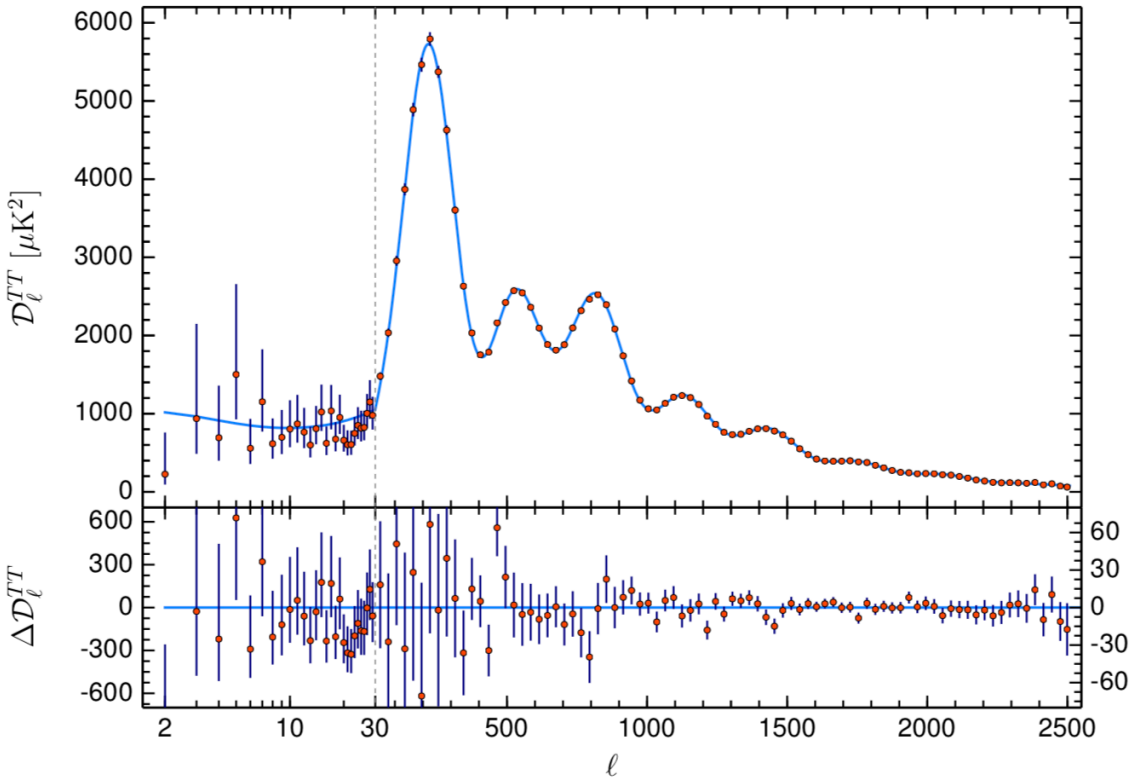

Figure 2.4: Temperature angular power spectrum of the CMB as a function of the monopole moment, l. Taken from Ref. [6]

first. Until this time, anything that interacts electromagnetically has been confined as result of the abundant free charges. Once the charged particles, and neutrons, coalesce into neutral atoms, photons are free to propagate. This "last scattering" imprinted itself and has been red-shifted into what we see today as the CMB, so the CMB contains information about this earlier time in the Universe. To summarize in one sentence: inflation set the initial conditions for the density fluctuations which yield the temperature fluctuations in the CMB at last scattering, which we can measure today.

Fig. 2.3 shows a sky map of the CMB and its fluctuations, which are of the order 10^{-5}. These temperature differences correspond to variations in the matter density, as the photons propagate more easily through the less dense areas these appear as cold spots, and inversely for the hot spots. Since we have an image of these non-uniformities across the entire sky we can relate the different hot and cold areas to their location (angle) on the sky, and decompose it into an angular power

spectrum using spherical harmonics, as shown in Fig. 2.4. The multipole moment, l, corresponds to the inverse angular scale and blue is a fit preformed using the ΛCDM cosmological model. The shape of the spectrum is related to the different densities of the various matter components of the Universe, and the fit parameters give us quantitative results for those different densities. The latest results from Planck are [6]:

$$\Omega_c h^2 = 0.120 \pm 0.001 \tag{2.2}$$

$$\Omega_b h^2 = 0.0224 \pm 0.0001 \tag{2.3}$$

where $\Omega_b h^2$ is the baryon density, which is consistent with Big Bang Nucleosynthesis (BBN) results [105], and $\Omega_c h^2$ is the dark matter density. This tells us that, of all the matter in the Universe, $\approx 84\%$ is dark matter.

2.1.2 Properties and candidates

Dark matter could exist without the need for Beyond the Standard Model (BSM) of particle physics solutions by taking the form of astronomical objects: 1) MAssive Compact Halo Objects (MACHOs) [34], which are becoming less viable [54]. Or 2) Primordial black holes [57], which could have been produced and decoupled in the early Universe. Dark could also exist as a particle(s) not contained within the Standard Model (SM) of particle physics, and the search for these particles will be the focus here.

We now state what properties this particle must have:

- Electrically neutral
- Weakly interacting, both with itself and other particles.
- Stable
- Non-relativistic
- Interacts gravitationally
- Correct relic abundance
- Accessible experimentally

There are essentially two categories of BSM particles that are regarded as solutions to the dark matter problem. Axions, which are constrained to very small masses, and Weakly Interacting Massive Particles (WIMPs), which is a generic term for a class of non-baryonic cold dark matter and will be discussed more below. Sterile neutrinos [29] are also mentioned, but due to there mass constraint < 10 keV/c^2 it is unlikely that they are responsible for the entirety of the dark matter

Axions were first introduced to solve the strong CP problem [86]. Accelerator searches have since ruled the original Axion candidates out, and new models with very small couplings were proposed essentially making them invisible [88]. Other models were proposed, [68] [52], and the

so-called Primakoff interaction was introduced. This allowed for an experimentally accessible decay rate into two photons and this is the basis for experimental work today. Bounds have been placed on the mass of the Axion, m_a, [100]: 0.5 μeV/c^2 $< m_a <$ 1 - 10 meV/c^2. Axions have all the properties a dark matter would have and, despite their small mass, are a viable option.

2.1.3 Weakly Interacting Massive Particles (WIMPs)

Weakly Interacting Massive Particles (WIMPs) compose a class of dark matter candidates which are proposed to interact with SM particles gravitationally and via the weak force. Many BSM physics models can produce WIMPs, for example, the Minimal SuperSymmetric Model (MSSM) can contain a stable weak scale particle, the neutralino, which is considered a WIMP. WIMPs gained popularity because they arise in many models for BSM physics and because such weak scale particles can satisfy all of the conditions for a good dark matter candidate.

Consider a new particle, χ, which is stable. In the early Universe, when the temperature was high, SM particles would annihilate into WIMPs at the same rate that WIMPs would annihilate into SM particles, i.e. they were in thermal equilibrium. As the Universe cools below the WIMP mass, m_χ, the number density, n_χ, falls exponentially (Boltzmann suppression). Then as the WIMP annihilation rate falls below the expansion rate the number density will reach a constant, relic, density. This is known as thermal freeze out, or the thermal freeze out mechanism.

This can all be made quantitative via a Boltzmann equation for the evolution of the WIMP number density [63] [100]:

$$\frac{dn_\chi}{dt} + 3Hn_\chi = -\langle\sigma_A v\rangle[n_\chi^2 - (n_\chi^{eq})^2] \tag{2.4}$$

where $H = \frac{\dot{a}}{a}$ is the Hubble parameter, a is the scale factor of the Universe, and $\langle\sigma_A v\rangle$ is the thermally averaged self-annihilation cross section. The first term on the right of Eq. 2.4 represents the WIMP number depleting from annihilation and the second term is from WIMPs being created via the inverse reaction. The second term on the left is the expansion of the Universe and if the right hand side were zero, meaning the number of WIMPs (co-moving number density) is not changing, then $n_\chi \sim a^{-3}$ as expected for non-relativistic matter.

When the temperature falls below the WIMP mass $(n_\chi^{eq})^2$ becomes suppressed, the condition for freeze out is $n_\chi\langle\sigma_A v\rangle = H$. And the thermal relic density can be approximated by:

$$\Omega_\chi h^2 \sim \frac{0.1\text{pb}}{\langle\sigma_A v\rangle} \tag{2.5}$$

And using dimensional analysis we can argue that:

$$\langle\sigma_A v\rangle \sim \frac{g^4}{m_\chi^2} \tag{2.6}$$

where g is a gauge coupling. If we assume g is the weak gauge coupling and $m_\chi \approx 100$ GeV then $\langle \sigma_A v \rangle \approx 10^{-26}$ cm$^3/s$. Now plugging the value for $\Omega_\chi h^2$ from the CMB power spectrum analysis, Eq. 2.2, into Eq. 2.6 also gives $\langle \sigma_A v \rangle \approx 10^{-26}$ cm$^3/s$. The fact that the WIMPs give the correct relic density is known as the WIMP miracle and is one of the reasons the experimental effort to detect them is vast. Note that this calculation is an estimate and the WIMP mass could exist in a range $\approx$ 1 GeV - 1 TeV. The remainder of this thesis will focus on their detection.

2.2 Direct detection

2.2.1 Introduction and alternative detection strategies

Since the details are not known, Fig. 2.5 shows a generic interaction between dark matter (DM) and standard model (SM) particles. This diagram can be viewed from three different ways corresponding to three different search methods: 1) From left to right we have DM coming in and only SM particles going out, which is referred to as indirect detection. 2) From right to left we have SM particles coming in and only DM going out, and this the method used at collider facilities. 3) From top to bottom we have a DM and a SM particle coming in and a DM and SM particle going out. This is know as direct detection because we see observe the direct result (target nuclei recoiling) of the DM-SM scattering inside the detector. This is a direct detection thesis and the focus will be on this method. It should be noted that a specific type of direct detection exists, called directional detection, which views the diagram in the same way. However, in addition to measuring the event time and energy seeks to additional directional information, the angular distribution of the recoil events. This additional information can help to constrain the direction of the incoming dark matter particles, providing unambiguous evidence of particle dark matter originating in the cosmos.

2.2.2 The WIMP halo

If the dark matter halo surrounding the disk of the Milky Way is composed of WIMPs, a flux of order $10^5 \times (100 \text{ GeV}/m_\chi)$ cm^{-2} s^{-1}, where m_χ is the WIMP mass, is expected on Earth. This should be measurable by observing the WIMP-nucleon elastic scattering in terrestrial detector target material. The so-called standard halo model (SHM) is a model of the WIMP velocity distribution. It assumes that the halo is an isothermal sphere with a density, ρ, such that $\rho \sim r^{-2}$. It can be described by a Maxwell-Boltzmann velocity distribution:

$$f(\vec{v}) = \frac{N}{(2\pi\sigma_v)^{3/2}} \exp\left(-\frac{|\vec{v}|^2}{2\sigma_v^2} \right) \tag{2.7}$$

where N is a normalization constant. The dispersion of the velocity, σ_v, is related to the galactic circular speed, v_c, via $\sigma_v = v_c/\sqrt{2}$. An upper cutoff is usually imposed on the velocity distribution due to the galactic escape velocity, v_{esc}. Commonly used values, and the values used in Sec. 5.4.5,

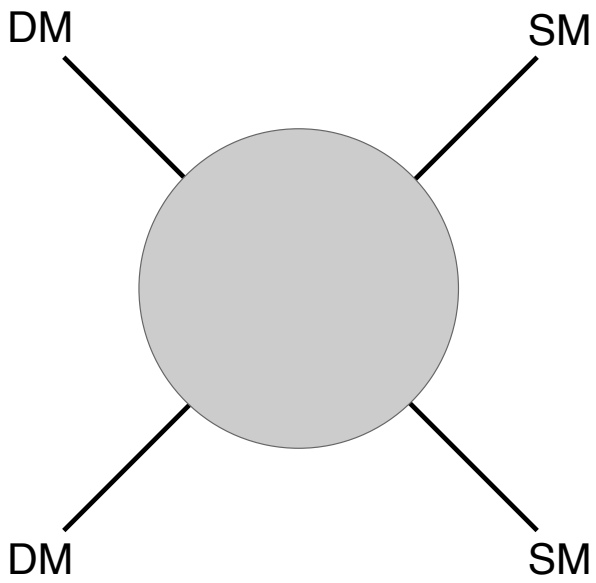

Figure 2.5: Generic diagram of dark matter and standard model particles interacting. From left to right: Indirect detection (looks for SM excess). From right to left: Collider searches (looks for missing momentum in collisions). From top to bottom, or bottom to top: Direct detection (looks for a SM particle which has had a "direct" interaction with a DM particle which has caused it to recoil).

are: $v_c = 220$ km/s, $v_{esc} = 533$ km/s, and $\rho = 0.4$ GeV/c^2 [78]. Speed distributions in both the galactic and Earth frame can be found in Fig. 5.2. It should be noted that there are large uncertainties in some of these astrophysical quantities, and a good summary of this topic can be found in Ref. [56]. The specific relevance of these uncertainties to directional detection will be discussed a bit more in Sec. 2.3.2.

The detectable signal which results, for Earth-based detectors, is due to relative velocity between the WIMPs and a detector's target material, and this is the direct detection signal. This is usually referred to as the "WIMP wind" and is contained within the flux previously mentioned. As observers on the Earth, the WIMPs look as if they are coming from a direction of the constellation CYGNUS, or the WIMP wind is coming from CYGNUS. Generally, direct detection experiments will measure the time an event occurs and the energy deposited in the detector associated with the interaction. As will be discussed in the next section, this allows for measurement of the differential energy spectra, see Eq. 2.17, which results in a detected number of events over a range of energy. We list the peculiar solar motion, in galactic coordinates, used in Sec. 5.4.5 here as well [100]: (v_x, v_y, v_z) = (11.1, 12.2, 7.2) km/s.

Additionally, since the Earth moves around the Sun, this detected rate will vary throughout the year in a predictable way. During one time of the year, the Earth will be moving into the WIMP wind and six months later it will be moving away from it, see Fig. 2.10 (Left). As a result, the

detectable number of WIMPs will vary throughout the year, and this is known as the annual rate modulation. Without more observables, the energy spectra is what we are interested in measuring, and the next section discusses some theoretical details of this.

2.2.3 Recoil rate and recoil energy spectra

Due to the galactic disk rotation speed, the expected relative velocity between WIMPs and a detector target is $\approx$ 200km/s and is non-relativistic. Using conservation of momentum and energy we can calculate the recoil energy of the target nuclei in the laboratory frame, E_r:

$$E_r = 2v^2 \frac{\mu_A^2}{m_A} \cos^2\theta_r \tag{2.8}$$

where v is the relative velocity, $\mu_A = m_\chi m_A/(m_\chi + m_A)$ is the specific WIMP-target reduced mass, m_A is the target mass, and θ_r is the angle between the initial WIMP direction $\hat{v}$ and the direction of the recoiling nuclei $\hat{r}$. It is useful to note that $\hat{v} \cdot \hat{r} = \cos(\theta_r)$. We can now see that the recoil energies expected are or generally below $\approx$ 100 keV, depending on the specific values of m_χ and m_A.

In general, the recoil rate is a function of both target recoil energy and direction. We can write the double differential energy spectrum per unit time and detector mass as [78]:

$$\frac{d^2R}{dE_r d\Omega_r} = \frac{\rho_{DM}}{m_\chi m_A} \int \frac{d^2\sigma_{\chi A}}{dE_r d\Omega_r} v f(\vec{v}) d^3v \tag{2.9}$$

where ρ_{DM} is the dark matter density, A is the number of nucleons in a target atom, and $f(\vec{v})$ is the WIMP velocity distribution. The double differential cross section, $\frac{d^2\sigma_{\chi A}}{dE_r d\Omega_r}$, can be decomposed as:

$$\frac{d^2\sigma_{\chi A}}{dE_r d\Omega_r} = \frac{d\sigma_{\chi A}}{dE_r} \frac{1}{2\pi} v \delta(\vec{v} \cdot \hat{r} - v_{\min}) \tag{2.10}$$

where

$$v_{\min} = \sqrt{(E_r m_A/2\mu_A^2)} \tag{2.11}$$

is the minimum velocity needed to induce a recoil with energy, E_r, and this can easily be seen by setting $\theta_r = 0$ in Eq. 2.8. The Dirac delta function encodes all of the angular information about the interaction while also imposing the minimum velocity constraint.

The differential cross section, $\frac{d\sigma_{\chi A}}{d_{E_r}}$, contains all of the particle physics of the interaction, and corresponding uncertainties. Fundamentally, it is dependent on the interaction strength of WIMPs and quarks, and this is calculated in terms of an effective Lagrangian since the exact interactions are not known. An entire framework has been developed where one writes down all possible quantum mechanical operators, composed of the low energy degrees of freedom of the system, and sums

the individual couplings to obtain the differential cross section. This is approach is referred to as an effective field theory and is quite general since each operator and nuclear response function is considered independently, and details can be found in Ref. [53].

For simplicity, the standard approach is to consider only two operators for which the transition probability, $|\mathcal{M}^2|$, where $\mathcal{M}$ is some matrix element, is not dependent on v: 1) A Spin Independent (SI) (scalar) contribution, and 2) A Spin Dependent (SD) contribution. These contributions add coherently to comprise the differential cross section:

$$\frac{d\sigma_{\chi A}}{dE_r} = \frac{\rho_{DM}}{m_A 2\mu_A^2 v^2}\left[\sigma_0^{SI} F_{SI}^2(E_r) + \sigma_0^{SD} F_{SD}^2(E_r)\right] \tag{2.12}$$

where σ_0^{SI} and σ_0^{SD} are the WIMP-nucleus cross sections in the limit of zero momentum transfer. F_{SI} and F_{SD} are the corresponding, spin-independent and spin-dependent, nuclear form factors and they account for any loss of coherence when the momentum transfer, $q = \sqrt{2m_A E_r}$ becomes large. For SI scattering we use the Helm form factor, [70], as is standard.

We can now rewrite the double differential scattering rate:

$$\frac{d^2R}{dE_r d\Omega_r} = \frac{\rho_{DM}}{4\pi m_\chi \mu_A^2}\left[\sigma_0^{SI} F_{SI}^2(E_r) + \sigma_0^{SD} F_{SD}^2(E_r)\right] \int \delta(\vec{v}\cdot\hat{r} - v_{\min}) f(\vec{v}) d^3v \tag{2.13}$$

where the integral on the right is the Radon transform. This is the 3D transformation of the WIMP velocity distribution and, in the limit of low momentum transfer, it is the only term that depends on the recoil energy, E_r. So, aside from scale factors, this is the recoil spectra of interest to experimenters. It should be noted that Eq. 2.13 will not be true for all interaction operators and specifically for those operators which have $|\mathcal{M}^2| \sim v^2$, $|\mathcal{M}^2|$ will have to be included inside the Radon transform [38].

We now consider the separate contributions. For SI scattering we can write [49]:

$$\sigma_0^{SI} = \frac{4\mu_A^2}{\pi}(Z f_p + (A-Z) f_n)^2 \approx \frac{4\mu_{p,n}^2 A^2 f_{p,n}^2}{\pi} \tag{2.14}$$

where f_n, f_p, μ_n, and μ_p are the WIMP-nucleon coupling constants, and reduced masses, for the neutron and proton, respectfully. The second equality is generally made under the assumption that $f_n \sim f_p$ and this is where the A^2 enhancement for SI scattering originates. We note that the couplings f_n and f_p are related to the WIMP-nucleon cross section by $\sigma_{n,p}^{SI} = 4\mu_{n,p}^2 f_{n,p}^2/\pi$, which is the quantity of interest for experimenters as it allows for comparison between detectors with various target materials.

The SD contribution can be written as [49]:

$$\sigma_0^{SD} = \frac{32}{\pi} G_F^2 \mu_A^2 \frac{J+1}{J}[a_p\langle S_p\rangle + a_n\langle S_n\rangle]^2 \tag{2.15}$$

where G is the Fermi constant, J is the angular momentum of the target, a_n (a_p) is the WIMP-neutron (WIMP-proton) spin dependent coupling constant, and $\langle S_{n,p} \rangle$ is the spin content of the target nucleus.

In an effort to put Eq. 2.13 into a useful form for calculating a specific rate we consider only the SI independent contribution and integrate out the angular distribution. The angular distribution must be integrated regardless unless the detector has the ability to measure it.

It can be shown [55] that:

$$\int_{\Omega} \int \delta(\vec{v} \cdot \hat{r} - v_{\min}) f(\vec{v}) d^3v d\Omega = 2\pi \int_{v>v_{\min}} \frac{f(\vec{v})}{v} d^3v \tag{2.16}$$

We can now use Eq. 2.16 and to manipulate Eq. 2.13 into a single differential rate. Then plugging Eq. 2.14 into Eq. 2.13, and utilizing the relationship between the WIMP-nucleon cross section and couplings noted above, we can write:

$$\frac{dR}{dE_r} = \frac{\rho_{DM} A^2 \sigma_{n,p}^{SI}}{2\mu_{n,p}^2 m_\chi} F_{SI}^2(q) \int_{v>v_{\min}} d^3v \frac{f(\vec{v})}{v} \tag{2.17}$$

The integral on the right is over the WIMP velocity distribution in the lab frame starting at the minimum velocity needed to induce a recoil, and we note that this is effectively a cut on the recoil energy, E_r.

Assuming the standard halo model for the WIMP velocity distribution we can employ the Heaviside function, Θ, to truncate it at the galactic escape velocity, v_{esc}, [38]:

$$f(\vec{v} + \vec{v}_e(t)) = \frac{1}{N_{esc}(2\pi\sigma_v^2)^{3/2}} \exp\left(|\vec{v} + \vec{v}_e| \right) \Theta(v_{esc} - |\vec{v} + \vec{v}_e|) \tag{2.18}$$

where N_{esc} is a normalization constant:

$$N_{esc} = \mathrm{erf}\left(\frac{v_{esc}}{\sqrt{2}\sigma_v} \right) - \sqrt{\frac{2}{\pi}} \frac{v_{esc}}{\sigma_v} \exp\left(-\frac{v_{esc}^2}{2\sigma_v^2} \right) \tag{2.19}$$

and σ_v is the velocity dispersion of the distribution. It should be noted in Eq. 2.18 the v_{esc} and $\vec{v}_e$ are measured in the halo frame whereas $\vec{v}$, the WIMP-nucleus relative velocity, is in the detector frame.

With the aid of Eq 2.16 we can evaluate the integral of the normalized WIMP velocity distribution described above [104]:

$$\int_{v>v_{\min}} d^3v \frac{f(\vec{v})}{v} = \frac{1}{2\pi} \int d\Omega \frac{1}{N_{\mathrm{esc}}\sqrt{2\pi\sigma_v^2}} \left\{ \exp\left[-\frac{(v_{\min} + |\vec{v}_e| \cos(\theta))^2}{2\sigma_v^2} \right] - \exp\left(-\frac{v_{esc}^2}{2\sigma_v^2} \right) \right\} \times \Theta[v_{esc} - (v_{\min} + |\vec{v}_e| \cos(\theta))] \tag{2.20}$$

$$= \frac{1}{N_{\rm esc}\sqrt{2\pi\sigma_v^2}} \int_{-1}^{1} d\cos(\theta) \left\{ \exp\left[-\frac{(v_{\rm min} + |\vec{v}_e| \cos(\theta))^2}{2\sigma^2} \right] - 2\exp\left(-\frac{v_{esc}^2}{2\sigma_v^2} \right) \right\} \times \Theta[v_{esc} - (v_{\rm min} + |\vec{v}_e| \cos(\theta))] \tag{2.21}$$

Using this result in Eq. 2.17, for $(v_{min} + |\vec{v}_e(t)| \cos(\theta)) < v_{esc}$, we are now in a position to evaluate the recoil energy spectra and calculate WIMP-nucleon scattering cross sections. We will refer back to this in Sec. 5.4.5.

2.2.4 Techniques and status of the field

Many groups use the scintillation light from liquid noble gases as their detection signal and the best WIMP-nucleon scattering cross section limits, above a WIMP mass of $\approx$ 20 GeV, come from these types of experiments. A simplistic description of this detection method is filling a tank with a scintillating liquid and surround it with an apparatus that can detect the scintillation light. This is an attractive approach because it scales to large sizes fairly straightforwardly because, as opposed to ionization, the signal isn't lost to diffusion over long drift distances, and these materials are self-shielding. The main concern as these detectors get larger is the radio-purity of the target material, and special facilities have been developed specifically for the manufacturing and purification of these liquid noble gases.

Cryogenic crystals

Solid state crystal experiments operating in the sub-Kelvin range are capable of very low energy thresholds and have excellent energy resolution. CDMSLite [7] quotes a threshold of 56 $\rm eV_{ee}$ and a resolution of $\approx 9\,\rm eV_{ee}$ at 0 keV to 101 $\rm eV_{ee}$ at $\approx 10\,\rm keV_{ee}$. According to the Debye law, there is a $\rm T^3$ dependance in the heat capacity of certain crystals and the idea is to exploit this for very low energy measurements. CRESST [17], EDELWEISS [21], and CDMS [10] are all successful implementations of this technique. It should be noted that ionization and scintillation are produced in addition to phonons in these crystals, and the detection of more than one signal can be used for background (electron) discrimination. EDELWIESS and CDMS, using a combined analysis, set a best upper limit of 3.3 $\times 10^{-44}$ $\rm cm^2$ at 90 GeV.

Scintillating crystals

The DAMA/LIBRA experiment consists of 250kg of NaI(Tl) crystals, and to date they claim an annual oscillating rate detection, which lies in the teal area in Fig. 2.6, with a significance of 9.3 σ which has been observed over 14 annual cycles [31]. It must be noted that many other experiments have ruled out this parameter space and DAMA/LIBRA is set to further investigate this signal using Photo Multiplier Tubes (PMTs) with higher quantum efficiencies [30]. The DM-

ICE collaboration has deployed similar crystal-based detectors to the South Pole to confirm or rule out the DAMA/LIBRA signal in the southern hemisphere, but to date no consistent signal has been observed [23].

Superheated fluids (bubble nucleation)

This technique involves operating detectors at a temperature which results in a metastable state in the liquid. An interacting particle will then deposit energy which can destroy this state causing bubbles to form which can be readout optically. These experiments have powerful electron discrimination because they can simply set the temperature above that which allows low energy events to cause a phase transition. There is also an acoustic signal accompanying the bubble nucleation which can help discriminate α-particles from nuclear recoils, as realized by the PICASSO experiment. SIMPLE [51], PICASSO [20], COUPP [28], and PICO [16] all operate using a liquid variant with a large ^{19}F content, which has an unpaired spin, allowing for constraints on the SD WIMP-nucleon scattering cross section, see Fig. 2.7.

Liquid noble gases

Liquid noble gas detectors have several advantages: 1) Large nucleon number to take advantage of the A^2 dependance in Eq. 2.14 2) High scintillation and ionization yield allowing for good background event discrimination and position reconstruction. 3) They are self-shielding which easily allows a fiducial volume to be defined in the center. 4) They are readily scaleable, and this is probably their biggest advantage. Setting the strongest limit is directly dependent on the exposure of the detector. Realistically, the amount of time any detector will operate is a few years. This leaves only the mass left to increase so the most straightforward strategy is to build large detectors relying on a simple operating procedure, and these types of detectors excel in this regard. Liquid Xenon is a popular target and is used by XENON1T, PANDAX [41], LUX [11] while others, DEAP-3600 [15], MiniCLEAN [109], and DarkSide [111] use liquid Argon. A few experiments, including DarkSide, use a dual-phase, liquid bulk and a thin gas layer at the end of the drift region, setup which aids in electron discrimination. For more details see Refs. [26] and [74].

Currently, XENON1T claims the best overall limit at 7.7×10^{-47} cm^2 with an exposure of $1042 \pm 12\,\text{kg} \times 34.2$ days [19]. This is shown in Fig. 2.6 along with other major experimental results. Many of the liquid noble experiments have plans for the next generation experiments consisting of multi-ton fiducial volumes and, as a specific example, DarkSide-20k is aiming for a SI cross section limit of 7.4×10^{-48} cm^2 ($6.9 \times 10^{-}47$ cm^2) for 1 TeV (10 TeV) WIMPs [3].

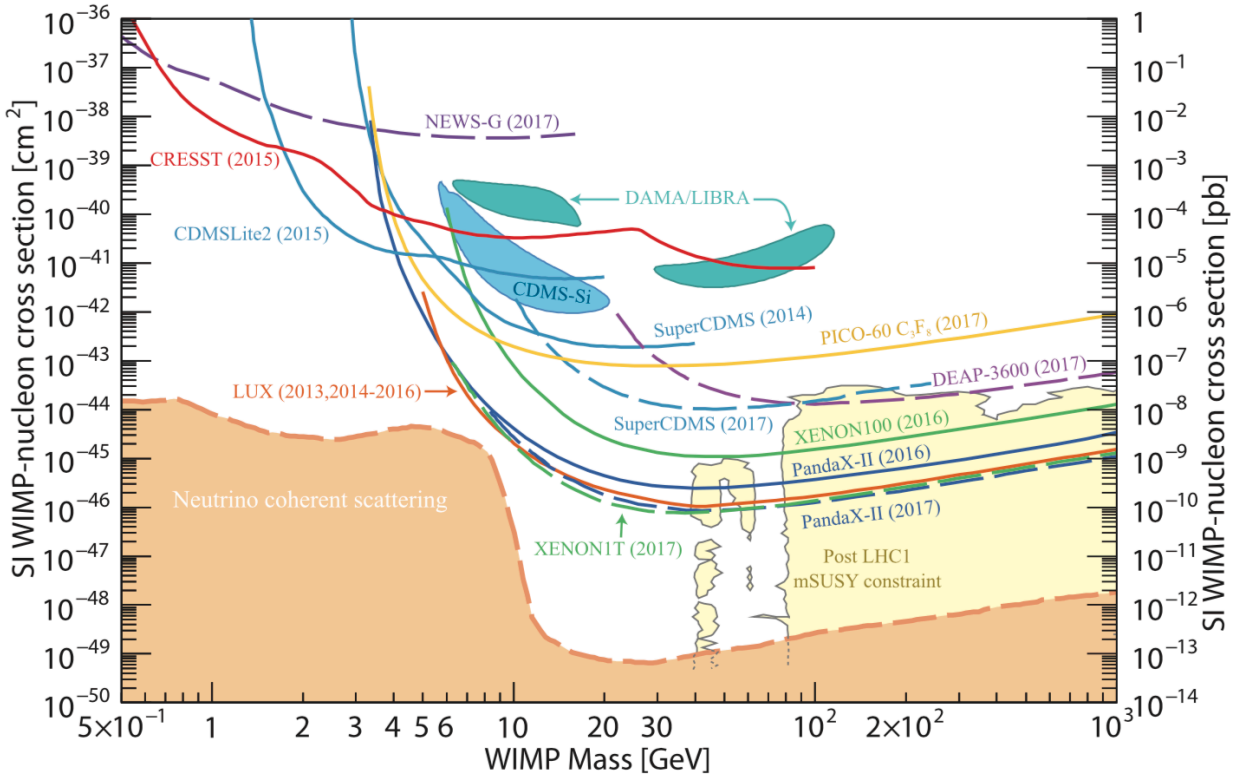

Figure 2.6: Spin independent WIMP-nucleon scattering cross section limits (current). Taken from Ref. [105].

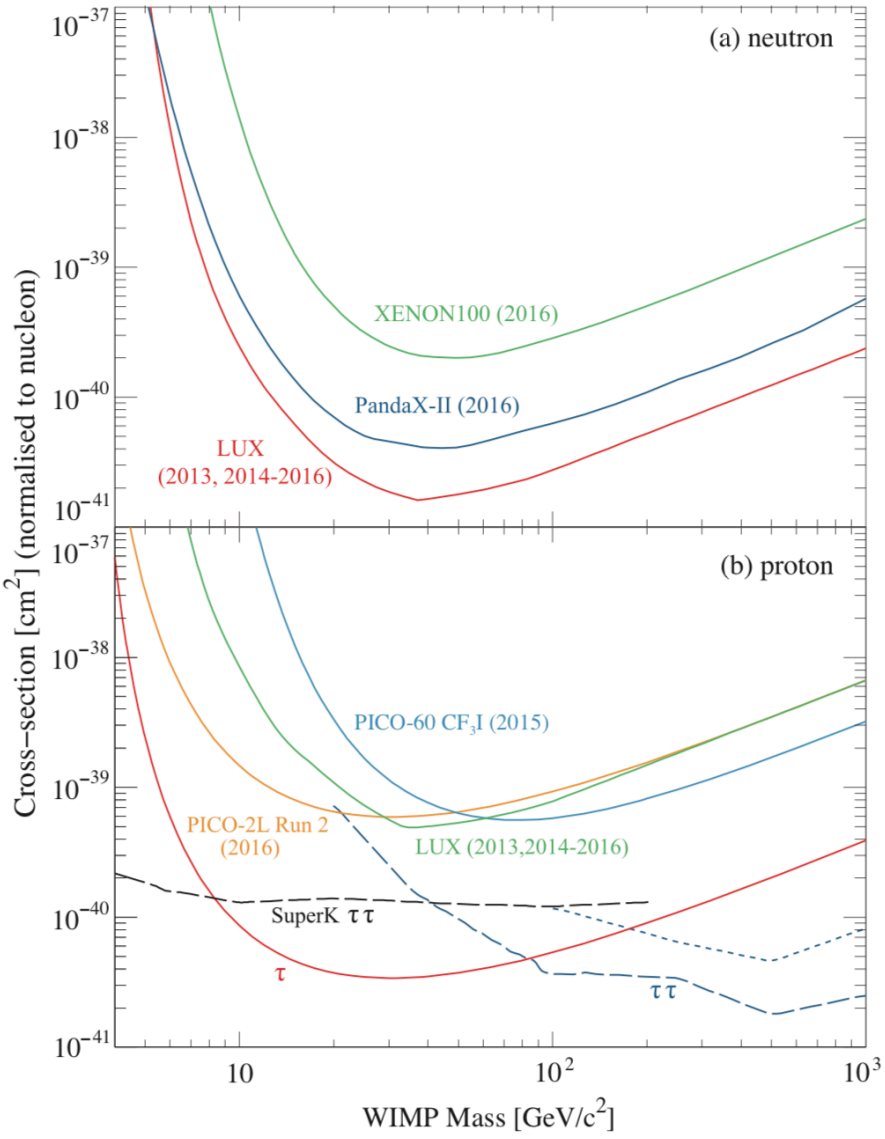

Figure 2.7: Spin dependent WIMP-nucleon scattering cross section limits (current). Taken from Ref. [105].

2.3 Directional detection

Spergel first mentioned the idea of using the highly anisotropic angular distribution of the WIMP signal in the galactic frame as a means of studying dark matter in 1988 [103]. In pursuit of this, several other advantages over traditional direct detection experiments have been realized. We will first briefly discuss the neutrino floor, then what exactly is meant by the term "directional detection", and then we will go through the advantages of directional detection systematically. We will close this section with a summary of current work being done in the field.

2.3.1 Defining and categorizing "directionality"

The orange area at the bottom of the plot in Fig. 2.6 is the result of solar, or atmospheric neutrinos, coherently scattering off of target nuclei in terrestrial detectors. This represents an irreducible background in detectors that measure only the event time and energy, and it is colloquially known as the neutrino floor. While measuring this signal would be a wonderful achievement, it is not the primary goal of dark matter experiments. And if the WIMP-nucleon cross section does lie within the neutrino floor, we will need another way to discriminate the neutrino events from potential WIMP events.

The double differential spectrum in Eq. 2.13 allows for input of angular information from a recoil distribution in addition to the energy spectrum. Fig. 2.9 depicts an experimental event, an ionization cloud, which has been reconstructed in 3D and orientated in some arbitrary coordinate system. Generally a χ^2-minimization is done, either with a line or some 3D distribution which can assign a primary axis of travel. This event was recorded with a FE-I4B pixel chip, as discussed in Sec. 3.2.3, and the color scale is proportional to the charge detected in each pixel. Each 3D box, or voxel, measures $50 \times 250 \times 250$ μm and the total event energy recorded is $\approx 1\,\text{MeV}$.

The head-tail signal

In order to fully describe and categorize directionality, we first need to introduce the concept of the "head-tail", or the "sense" measurement of an ionization distribution. Fig. 2.8 shows a 2D projection of an event, again recorded with a FE-I4B pixel chip, where the color scale represents the amount of charge recoded by each pixel. This is an image of the ionization cloud produced by some nucleus inside one of our gas detectors, discussed starting in Sec. 3.2.1, recoiling from a scattering interaction, likely with a neutron. What is clear in this image is that the recoiling particle is moving horizontally across the plane of the pixel chip. However, what is not immediately clear is if the particle is moving from right to left or from left to right.

The high resolution charge readout available with these pixel chips allows us to answer this question by splitting the track into two pieces and determining which half contains more charge, or which is half is the "head" and which half is the "tail". This is discussed more in Sec. 2.4.1 in

relation to the Bragg curve of the particle. For now we note that if a detector has this ability, we say that it can measure the "head-tail" of a track. The importance of this measurement will be discussed as we move through this section, and thesis, but the most crucial aspect is that without this ability, there is a 180° ambiguity in the resulting angular distribution.

As will be discussed in Sec. 2.4.1, the method in which nuclear recoils deposit their energy in a target medium is complicated and results in an uneven ionization distribution along the track. At MeV energies, the distribution is relatively flat and this can be seen in a particle's Bragg curve, see Fig. 2.14 for an example. However as the particle loses energy the situation becomes more complicated owing to effects like straggling, where the particle trajectory changes drastically, and that the particle will lose a smaller proportion of its remaining energy to ionization. This is somewhat of a benefit because in the areas of the track where the distribution is flat the head-tail effect is small, and as the distribution becomes less isotropic the effect becomes larger. However, there is also less overall charge to measure and this is why good energy resolution is needed. This is currently being studied but an energy resolution of $\approx 20\%$ is enough to for an efficiency of $\approx 80\%$ for recoils with energies less than 100 keV [58]. Lower energies will be investigated in the near future.

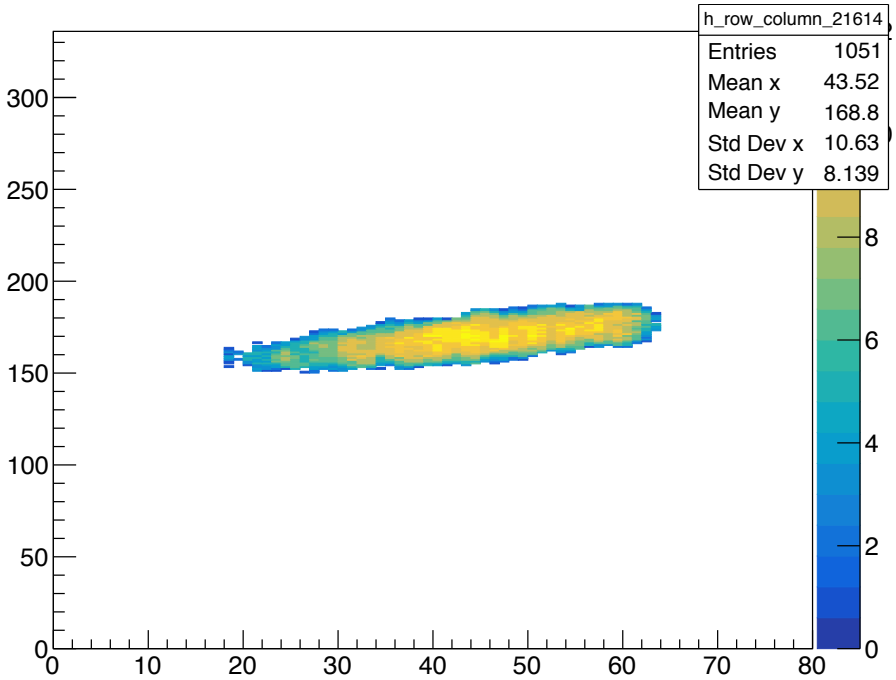

Figure 2.8: Event head-tail. A 2D projection of an ionization distribution, recorded with a FE-I4B ATLAS pixel chip, created from a recoiling nucleus induced via scattering with a neutron. We seek to know if the nucleus is traveling from left to right, or from right to left. Equivalently, we are seeking the "head-tail" information of the track. See text for discussion.

Differences in directional detection capabilities

The idea of directionality is that angular distribution of many recorded events could be used as another observable in addition to the energy and time of the event. This distribution could be transformed into galactic coordinates and used as a discriminate for neutrinos originating from the Sun, for instance. What is shown in Fig. 2.9 is the result of a directional detector with what we will call "vector 3D ionization cloud (track) reconstruction" capabilities, and represents the maximal amount of information that can be extracted on an event by event basis. However, directional capabilities exist various levels of sophistication and we list them next, roughly in the order of information per event which, for instance, has a direct correlation with the number of events needed to reject an isotropic background signal.

Levels of directional capabilities (more information than event time and energy):

- Directional dependance on event rate - No track reconstruction capabilities, but a detector with an asymmetric exposure or response would provide a different event count rate when oriented along a line towards CYGNUS vs. a line perpendicular. This is all assuming, of course, that the pitch and resolution are fine enough.
- 1D track reconstruction (with or w/o head-tail) - Minimal track reconstruction. Essentially, any segmented 1D readout, a row of wires for example, would provide a 1D projection of an ionization distribution. Alternatively, a non-segmented readout with a digitized readout would provide reconstruction via the varying arrival times of the charge.
- 2D track reconstruction (w/o head-tail) - Allowing one angle, either θ or ϕ in Fig. 2.9, to be measured with 180° ambiguity.
- 2D track reconstruction (with head-tail) - Allowing one angle to be measured with no ambiguity.
- Axial vector 3D track reconstruction (w/o head-tail) - Allowing both angles, θ and ϕ in Fig. 2.9, to be measured with 180° ambiguity.
- Vector 3D track reconstruction (with head-tail) - Allowing both angles to be measured with no ambiguity.

2.3.2 Directional detection advantages and the dipole signal

When deciding which readout to outfit a detector with an optimization considering cost really needs to be done. This is studied is detail in Ref. [24], and here we will simply describe some general advantages. One important aspect of directional detection technology is the highly segmentation of some of the readouts. Meaning that even without utilizing the angular distribution, the high resolution track reconstruction produced by some readouts allows for powerful event discrimination. Using just the event length and energy, electron discrimination looks feasible down to $\approx 7\,\mathrm{keV}$ [24].

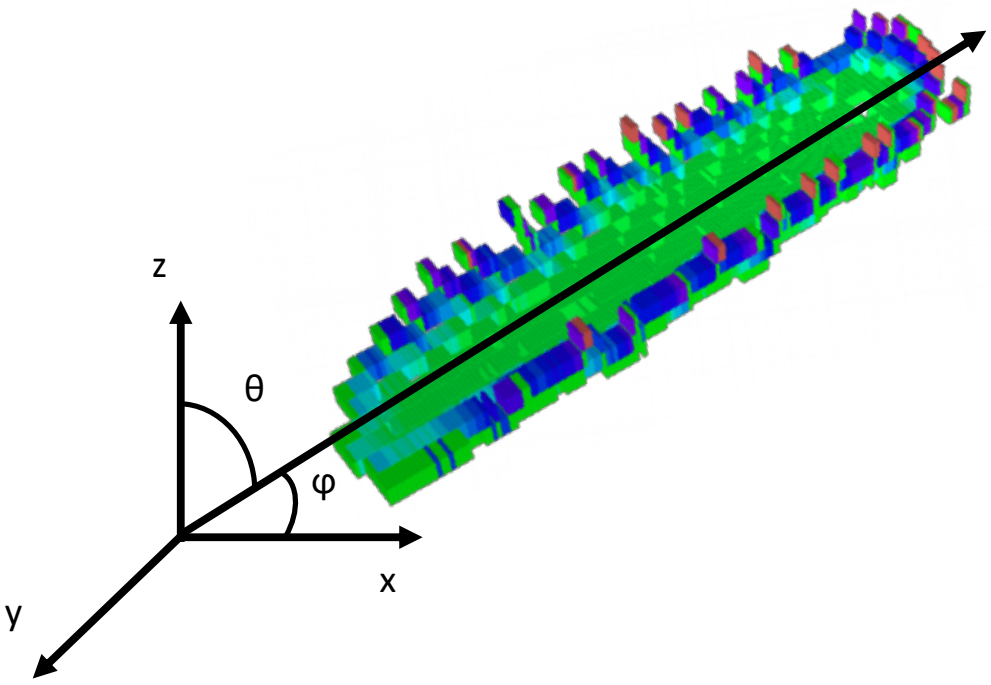

Figure 2.9: 3D ionization distribution of a recoil event recorded in one of our detectors with an FE-I4 ATLAS pixel chip. Each box measures 50 × 250 × 250 μm and the color is proportional to the charge measured in each pixel. If an ionization distribution can be assigned a primary axis then it can be deduced which direction the scattering particle was traveling.

If the event topology is used electron discrimination at even lower energies could be achieved, and this is currently under study.

Once the information from the angular distribution is put to use many other avenues of study open up. We list these roughly in the order of exposure while noting that not all levels of directionality, listed above, will allow for every topic listed below:

- Set more stringent limits than the neutrino floor would allow a traditional detector to set
- Isotropic backgrounds can start to be ruled out
- The dipole signal, described next, can be measured
- WIMP velocity distribution can be studied
- Particle interactions can be studied

When transformed into galactic coordinates, terrestrial backgrounds will appear isotropic, or nearly isotropic. This is where the power of directionality really starts to appear because in galactic coordinates the WIMP wind appears as a very distinct signal, which terrestrial could not mock.

The dipole signal

As mentioned, because of the solar motion around the galactic center, and through the WIMP halo, we perceive the particles coming at us as a "wind". If one plots the angular distribution of the WIMP flux in galactic coordinates, left plot in Fig. 2.11, a striking signal appears. Since the solar motion through the halo is in one direction, the flux of WIMPs appear to come from this direction, from the constellation CYGNUS. The plot on the right of Fig. 2.11 shows what an idealized detector with vector 3D track reconstruction capabilities would produce with Fluorine recoils induced from WIMP interactions. The extra spread, compared to the original WIMP signal on the right, is due to the scattering angle. This is known as the galactic dipole signal and is the main draw of directional detection because of its high discovery potential and eventual need for signal confirmation. As studied in Ref. [80], using the mean angle between the solar motion and recoil directions, as few as 10 detected events could reject isotropy from a detected signal.

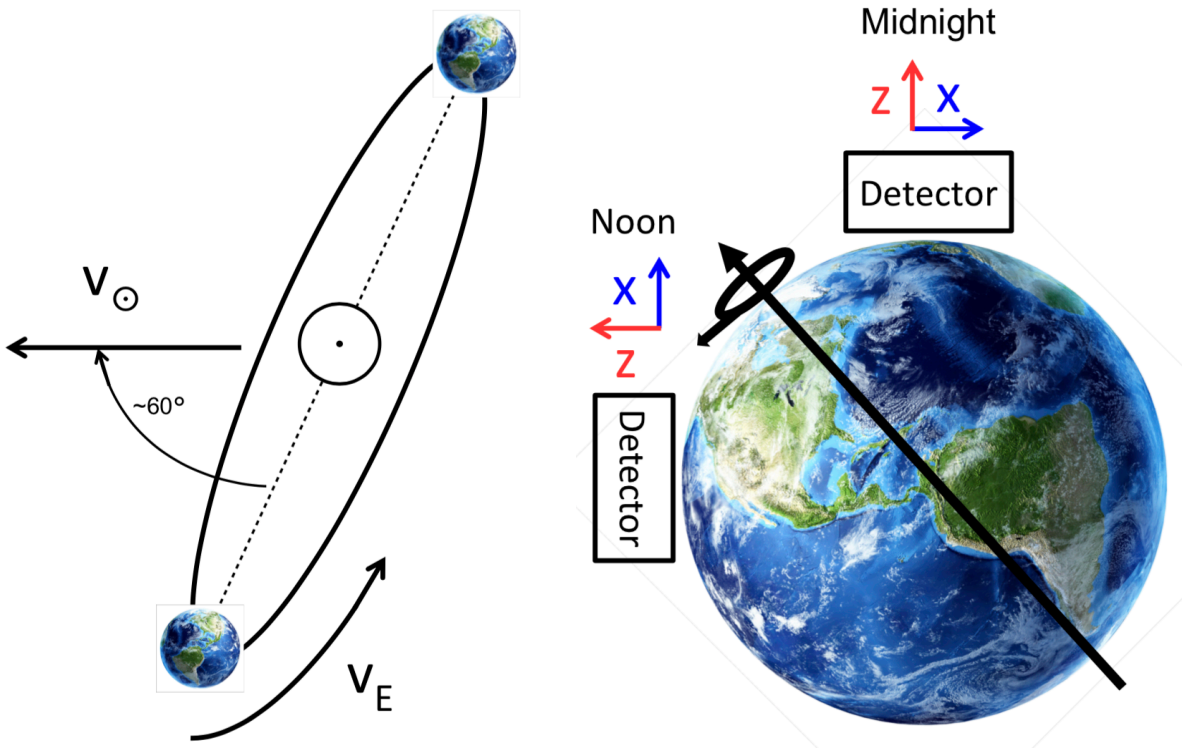

Figure 2.10: Left: Cartoon of the plane of the solar system relative to the solar motion in the galactic plane. Right: Depiction of the lab frame rotating in galactic coordinates. The detector frame rotates with the Earth but travels towards the constellation in the galactic frame, denoted by the x in the plots in Fig. 2.11. Nuclear recoil tracks induced by WIMPs will also point towards CYGNUS.

The high discovery potential for directional detection is a result of this superior background

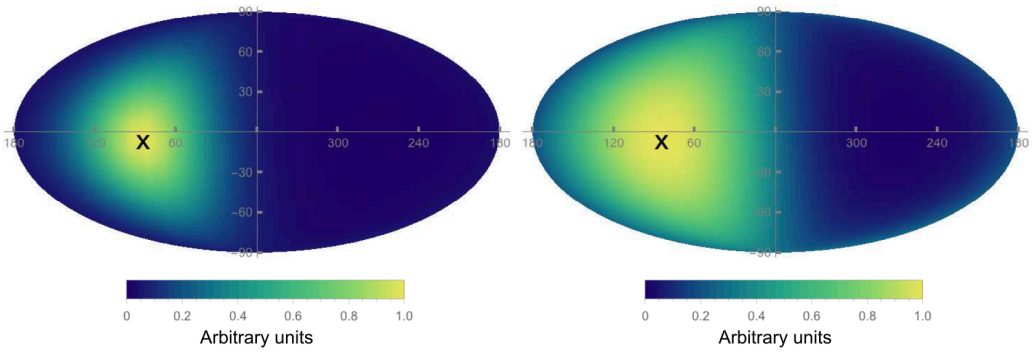

Figure 2.11: Left: 100 GeV WIMP flux above $v_{\min}$ to produce 25 keV Fluorine recoils. Right: Angular distribution of the energy differential recoil rate for Fluorine recoils from 100 GeV WIMPs. Plotted in galactic coordinates. Taken from Ref. [78].

rejection and it should be noted that traditional detectors lack the ability to resolve the dipole signal. It should further be noted that without the head-tail measurement, and with a 180° ambiguity, the plots in Fig. 2.11 would essentially be folded in half, mixing the anisotropic signal with the isotropic background. This illustrates the importance a detector's ability to measure the head-tail signal. On an event by event basis a 2D detector with head-tail capability is more powerful than a 3D detector without it.

In addition to the discovery and signal confirmation potential, information from the angular distribution of detected events could further be used to constrain the parameter space of specific dark matter-nucleon operators [38] [64]. Directional information could also be used to study the details of the WIMP velocity distribution, and test if we are inside of a dark matter hurricane [83]. Related to this, we refer back to the uncertainties in astrophysical quantities of the halo mentioned in Sec. 2.2.2. Recently, hydrodynamical simulations of the baryonic halo content in Milky Way type galaxies have shown that it can have a non-negligible effect on the halo structure itself. Large deviations from the standard Maxwellian distribution have been seen [56].

If it is the case that the velocity dispersion of the dark matter content of the halo is different than we assume, then this would have (significant) implications for directional detection. Consider if the dispersion were much lower, then the dipole signal would peak much more sharply and this would mean that our detectors would have head-tail sensitivity with worse energy resolution. This would result in money and resources being pooled into increasing the detector exposure rather than striving for better energy resolution, which would not be used. On the other hand if the dispersion were higher, then achieving the best possible energy resolution might be necessary to resolve the dipole signal at all. As the directional detection effort continues, and grows, this optimization study will need to be preformed to inform where the resources will be utilized most effectively. Next we will discuss some current directional detection experimental efforts around the world.

2.3.3 Status of the field

Several directional detection experimental endeavors are underway and, while most involve gas Time Projection Chambers (TPCs), there are other approaches. Emulsions are used by some groups, [66] [42], allowing for resolution of $\approx 100\mu$m recoil tracks, and the higher density allows these detectors to be much smaller than gas TPCs. Other materials such as crystals, carbon nanotubes and even DNA have be explored, [89] [37] [46]. Regardless of the material, the goal with all of the methods is to image the recoil tracks. Gas TPCs can operate can various pressures, thereby allowing for various recoil track lengths. And since WIMPs deposit such small amounts of energy, it is usually necessary to operate these TPCs with low pressure.

DRIFT operates with a Negative Ion (NI) gas mixture at low pressure [101] and, is to the author's knowledge, the only underground experiments which has successfully demonstrated this. The ionization is readout via a plane of Multi Wire Proportional Counters (MWPCs) and, as a result is not able to be reconstructed in 3D and has lower position resolution than pixelized readouts. They were, however, the first to demonstrate a method allowing for the absolute measurement of the drift coordinate, z, as the result of what is normally undesirable. A leak allowed a small of a "containment" gas to seep into the vessel and it was realized that this "containment" was actually drifting signal ionization to the readout in addition to the primary gas. These two different gases drift the ionization at different speeds and will arrive at the readout at slightly different times and this information can be exploited for an absolute z coordinate. This allowed for a background-free dark matter run and resulted in an upper SD limit of 1.1 pb at a 100 GeV/c^2 [25].

MIMAC is an electron drift TPC [79] [90] which uses a CF_4 gas mixture aimed at a SD interaction and reducing drift velocity while giving sufficient gain [77]. A Micromegas is used for readout as full 3D track reconstruction is a primary goal, and larger detectors are planned.

NEWAGE uses electron drift in pure CF_4 at low pressures, and has many R&D efforts. The readout is an in-house designed micro-pixel-chamber, μ-PIC, which also uses GEM amplification, discussed in Sec. 3.2.2. Performance studies show $\approx$ 40% detector efficiency and an angular

resolution of 40° at 50keV [106]. They were also the first to produce a direction-sensitive dark matter limit [81] with an underground run at Kamioka, and have since been able to produce plots like the one the right of Fig. 2.11 with experimental data.

DMTPC was a low pressure CF_4 TPC using electron drift with CCDs and low noise integrating amplifies to measure both scintillation and ionization. They were the first group to measure to full vector direction of recoil tracks using the head-tail measurement [47]. A 10 L prototype was operated the WIPP underground facility and produced a SD scattering limit [9] but this effort has since been abandoned.

NITEC [22], among other prototypes, is another effort using optical readouts for track reconstruction. The CYGNO project, recently funded by INFN, will feature sCMOS cameras and PMTs in a 1 kg gaseous TPC and will be housed at Laboratori Nazionali del Gran Sasso (LNGS).

The directional detection community is international and there is a board effort in combining knowledge and resources into a large detector project, known as CYGUNS. With this in mind, we will briefly discuss the attributes of an idealized dark matter detector.

2.3.4 The ideal detector

We can describe two different eras of dark matter detection simply as before and after it is discovered in a lab. After discovery, it will be necessary to build detectors capable of extracting details about the interactions themselves, which directional detectors are well suited for. However for discovery, it might be thought best to keep on the current track on building larger liquid noble gas detectors but this may be short sighted. Directional detectors can also aid in discovery by needed fewer events because more information is contained per event. They will also be needed for confirmation of cosmological origin should a discovery be made elsewhere. We summarize the detectors attributes the ideal detector would possess for success both for and after discovery:

- Vector 3D ionization distribution (track) reconstruction
- High positional resolution
- Low energy threshold
- Good energy resolution
- Inexpensive
- High signal/noise ratio
- Easily scaleable

An effort is underway [24] to determine the most cost-effective way to build such a detector. The most compact would employ some sort of pixel ASIC readout, wether it be a $x - y$ strip readout or some specialized pixel chip remains to be seen. What is clear is that without a readout capable of the vector 3D reconstruction, the detector would have to be very large to achieve the

same discovery power. In the end, it is the author's view, that a customized pixel readout will be needed. Our group currently uses ATLAS pixel chips, Sec. 3.2.3, which have 50×250 μm pixels and a digitization rate of 40 Mhz. The benefit of a pixel readout is the low noise and threshold which result in a high signal/noise ratio, but it is expensive. One important consideration is that large areas, ≈ 1 m^2 or ≈ 10 m^2, need to be instrumented for this to be a competitive method, and this likely means lower resolution pixels will need to be developed.

It is also not clear what the exact detector target should be. Negative Ion (NI) gases, Sec. 2.4.2, essentially increase the ability to retain directional information through longer drift distances by diffusing the primary ionization cloud less than electron gases. However, it is not obvious that the required gain or gain stability can be achieved. If NI gases are employed the readout will have to compensate for the very different drift velocities, a factor of 10^3 lower than electron gases. All of this leads to the conclusion that the ideal detector would have a pixelized readout with $\approx$ mm^2 pixels with an adjustable digitization rate to allow for NI drift, and a gain stage which takes advantage of charge avalanching, Sec. 2.4.3, to allow for a high signal to noise ratio.

We will now go through an overview of relevant detector physics and phenomena before moving to experimental work and analysis.

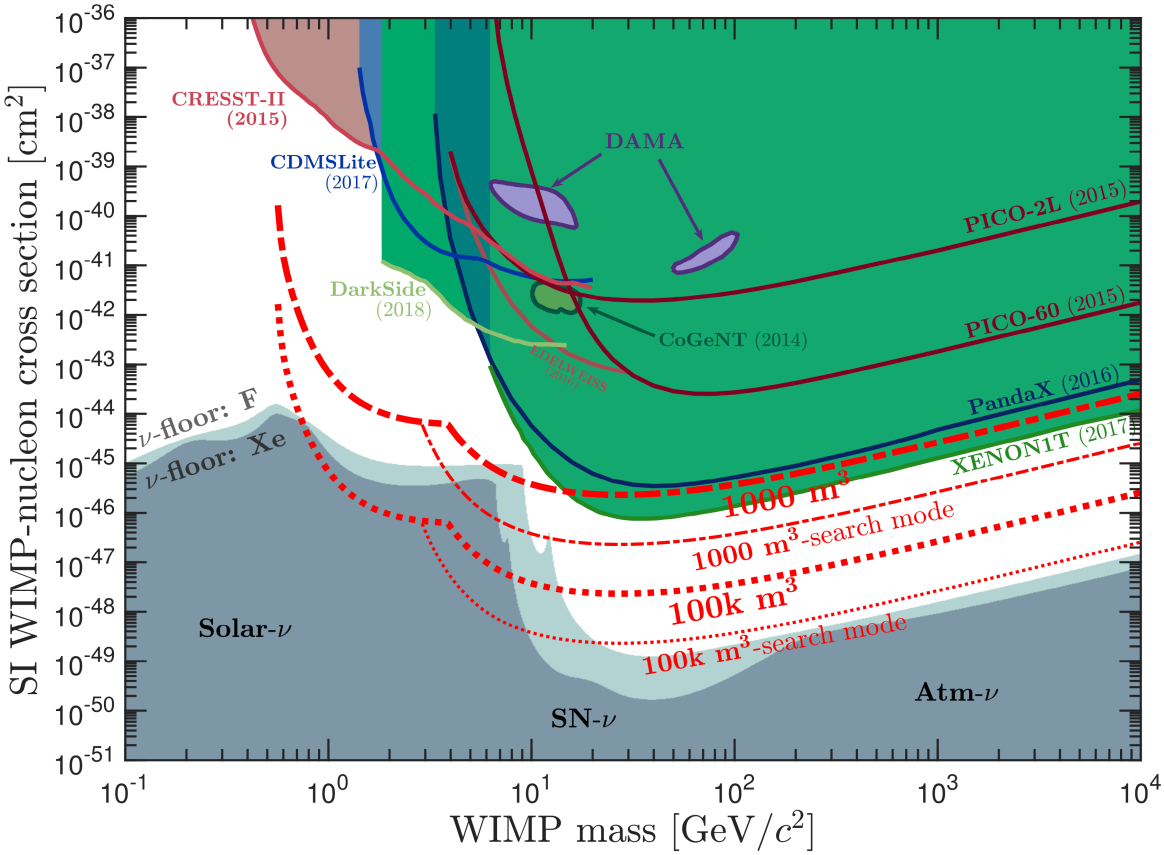

Figure 2.12: Comparison of new directional detector concept with existing limits. The red lines represent a proposed directional detector discussed in Ref. [24]. The concept detector target material is a mix of SF_6, which allows for negative ion drift, and Helium, which allows for low mass reach. The different modes, "search mode" and "directional mode", correspond to different proportions of Helium. In the search mode less Helium is used to increase exposure, while in directional mode more Helium is used to extend the low mass reach further. The live time here is three years. Used with permission.

2.4 Detector physics

2.4.1 Interactions of radiation with matter

Different radiation types generate specific detector responses, largely energy dependent, that allow them to be identified. This Sec. will briefly summarize relevant radiation types along with their corresponding detector signatures.

X-rays and γ-rays

Fig. 2.13 shows the total photon cross section as a function of photon energy in Carbon (top) and Lead (bottom). We will discuss the three main regions of interaction in terms of increasing photon energy.

Photoelectric absorption

Starting below $\approx 100\,\mathrm{keV}$, as the photon energy approaches atomic binding energies, the photoelectric cross section becomes dominant. A photoelectric absorption is an interaction between a photon of sufficient energy and an atom which absorbs the photon by emitting a bound electron, usually from the most tightly bound K-shell electrons, called a photoelectron. If a photon has excess energy, above that binding the electron, the remainder will be carried off as kinetic energy with the photoelectron which will then move through the detector creating ionization.

After emitting a photoelectron the atom is let in an excited state and will de-excite via a rearrangement of the remaining electrons and, as a result, a series of characteristic X-rays can be emitted. These X-rays will have energies specific to the difference in binding energies of the atom. Generally, they continue to move through the detector until they are absorbed, releasing more photoelectrons which ionize, until the original photon energy has been completely transformed into ionization. This ionization can then be collected and a measurement of the original photon energy can be preformed. It should be noted that some of these characteristic X-rays, with UltraViolet wavelengths, are called fluorescent and detectors exist that explicitly measure these.

The different binding energies can be seen on the left side of the plots in Fig. 2.13 as sharp peaks, referred to as a K-edge, or whatever shell has been vacated, and we can understand these by following from higher to lower energy (right to left). As the photon energy decreases and gets closer to the binding energy of the shell, the probability that it will interact steadily increases until the photon energy becomes lower that the binding energy, at which point the electron can no longer be ejected and the probability sharply decreases.

Interactions involving bound electrons can be complicated and often involve more than one specific process. For instance there is a certain probability that one of the X-rays, produced in the above situation, can leave the sensitive volume of the detector before it is absorbed resulting in a measured energy lower than that of the original photon being measured. This lower energy

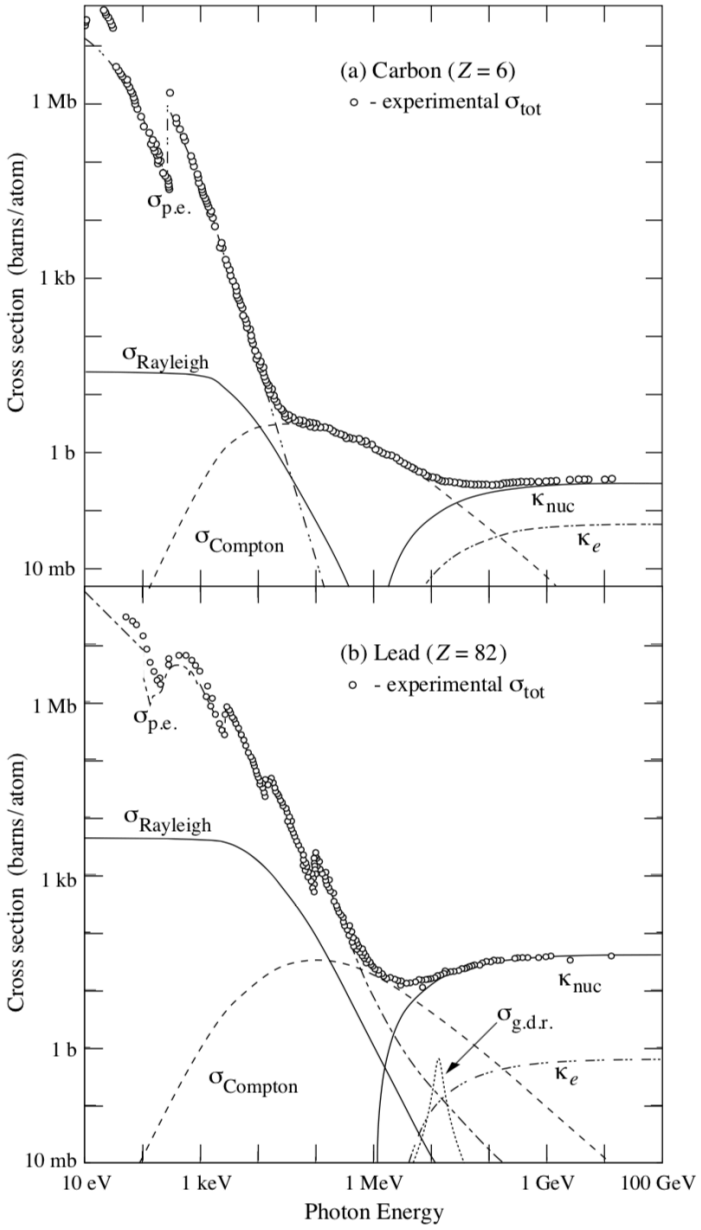

Figure 2.13: Total photon cross section as a function of photon energy. Figures taken from [105].

will be equal to the original energy of the photon minus the binding energy of whichever electron was ejected and is called the escape energy, or escape peak, referring to the X-ray that escaped the detector.

In addition to an X-ray escaping the detector, there is a certain probability that one will not be produced at all. An excited atom, with a vacant K-shell for instance, will de-excite via a higher energy shell, more loosely bound, electron "falling" into to vacant position and this usually results in a X-ray being produced. However, it is possible for the "falling" electron to give a kinetic kick to an even higher energy shell electron ejecting it from the atom. These Auger electrons will continue to ionize in the detector and are a subject of study in spectroscopy in their own right.

Compton scattering

As the photon energy increases so does the probability of Compton scattering, and this interaction is prevalent among γ-ray energies from typical radioactive sources. An electron, generally regarded to be at rest, can scatter a photon through an angle θ and recoil, in the process, extracting energy from the photon. Since all angles are accessible, a large portion of the photon energy can be transferred to the electron and the change in trajectory can be drastic. The following formula describes the interaction [50]:

$$h\nu' = \frac{h\nu}{1 + \frac{h\nu}{m_0 c^2}(1 - cos\theta)} \tag{2.22}$$

where hν and hν' are the original and scattered photon energies, respectively, θ is the angle between the original and scattered photon path, and m_0c^2 is the rest mass of the electron. In general, the probability of Compton scattering increases linearly with the number of electrons the atom contains, Z, and falls off with increasing photon energy.

Pair production

As the photon energy increases beyond twice the rest energy of the electron, 1.022 MeV, the production of an electron and a positron becomes kinematically possible. However, the probability remains fairly small until the photon energy reaches several MeV. Once the electron and positron are produced they travel, on average, a few mm in the target material before losing their energy to ionization creating an energy peak of the photon energy minus twice the rest energy of the electron and, for this reason, pair production is an important mechanism for γ-ray detectors.

For instance, in a Positron Emission Tomography (PET) scan a patient is placed into the center of a series of γ-ray detectors which are arranged into a circle. Prior to the scan the patient has been injected with a substance that releases γ-rays with an energy such that the probability of pair production is high. In areas of high metabolic activity, such as certain cancers, this substance will accumulate emitting a higher rate of γ-rays than surrounding areas with a lower metabolic rate. These γ-rays are then detected by multiple detectors which help to localize the "hot spot". This is usually done in conjunction with a Computed Tomography (CT) scan to show where the high radioactive areas are in relation to anatomical structures.

Charged particles and nuclear recoils

There are many ways to categorize how charged particles interact with matter. A common way is to talk about heavy charged particles, i.e. α-particles, separately from recoiling nuclei that are induced from collisions with uncharged particles, and this certainly makes sense, however we will take a different perspective. Consider a detector filled with Helium as a target material that is exposed to a neutron source, many ionized recoiling Helium nuclei will result. Since ionized Helium (^{4}He) nuclei are α-particles, we will talk about heavy charged particle interactions under the guise of nuclear recoils. This is not done arbitrarily. Since WIMPs have no electric charge, the result of their interaction with a detector target will appear as any un-charged particle interaction. We can then define two categories of a neutral particle interacting with a detector target medium: 1) Coherent scattering with detector target nucleus (neutral particle-nucleus scattering), and 2) Neutral particle-electron scattering. We will discuss both of these interactions.

Nuclear recoils

Charged particles that are highly relativistic, $\beta = v/c \approx 1$, will lose most of their energy to radiative effects, Bremsstrahlung and Cherenkov radiation. Given that the galactic rotation speed is $\approx 10^{-3}c$, and WIMPs move non-relativistically there should not be any recoils in this energy regime that are of interest for dark matter detectors and these effects will not be discussed further.

As radiative effects become sub-dominant, nuclear recoils are well described by the Bethe equation [50]:

$$\frac{dE}{dx} = \frac{4\pi e^4 z^2}{m_0 v^2} NB \tag{2.23}$$

where

$$B = Z(ln\frac{2m_0v^2}{I} - ln(1 - \frac{v^2}{c^2}) - \frac{v^2}{c^2}) \tag{2.24}$$

Here v and ze are the ionizing particle velocity and charge. N and Z are the target medium number density and atomic number, and m_0 and e are the electron rest mass and charge, respectively. This is generally valid while the velocity of the ionizing particle is much larger than the speed of the orbiting electrons in the material being traversed. One further assumption is that all of the energy loss of the ionizing particle is due to interactions with electrons, electronic stopping, as opposed to interactions with other target nuclei, nuclear stopping, and this is generally the case until lower energies are obtained.

Via many Coulomb interactions a charged particle will leave a trail of ionization which encodes its nature. This trail is referred to as an ionization cloud or a recoil track. The term $-dE/dx$ is called the specific energy loss and we note some major features. For a given velocity, the z^2 in Eq. 2.23 results in heavier nuclei experiencing much greater charge loss. The v^2 will generally

result a much lower energy loss for faster particles but, as a result of the logarithmic term, there is minimum specific energy loss that high velocity particles will approach. These are appropriately called minimum ionizing particles and will leave clusters of ionization with "empty" spaces in-between as they skip through a detector media. The author thinks of these as the skipping stones of particles. To understand further details a specific example will be considered, the α-particle.

Doubly ionized and possessing an energy in the MeV range, α-particles can deposit a large amounts of energy in short distances. Interactions occur with many target atoms simultaneously and the net result is a decrease in the velocity of the α-particle. The interactions include raising electrons to higher energy levels, atomic excitation, or complete removal of electrons from the atom, ionization. In addition to being ionized, some of the electrons will also receive large amounts of kinetic energy and will continue to produce additional ionization. These electrons are called delta rays and can travel in directions away from the track, but since they originate from the track, this can result in clusters of ionization forming along it.

The Bragg curve of a particle is a plot of the specific energy loss vs. the distance traveled. Fig. 2.14 shows an average Bragg curve for $\approx 5.3\,\mathrm{MeV}$ α-particles in atmospheric pressure $ArCO_2$ (70:30), and it is essentially a demonstration of Eq. 2.23. If one were to superimpose the Bragg curve for a single α-particle on top of Fig. 2.14 differences would be seen in the actual distance of travel and total energy deposited. These differences are referred to as straggling both in distance and energy, respectively [50]. It is a result of the fact that individual particles will undergo slightly different microscopic interactions, and is statistical in nature, so even a beam of mono-energetic particles will result in a distribution of energies deposited and distances traveled.

As an α-particle travel through the media, the amount of energy loss increases, but that loss distribution also spreads out because of straggling. Then, near the end of the track, the amount of energy loss sharply decreases, associated with a narrowing of the loss distribution, because of the now very low energy of the particle. The peak in Fig. 2.14 is associated with the particle accumulating charges as it slows which results in the sharp decrease in energy loss. Generally, particles with higher Z will start to accumulate charge at lower energies as a result of the specific energy loss being higher.

As mentioned, as the energy becomes lower the Bethe model begins to fail and corrections need to be considered. For $\approx 0.01 < \beta < 0.05$, no satisfactory model exists and the simulation tool Stopping and Range of Ions in Matter (SRIM) [61] is standardly used. Once $\beta < 0.01$ and the velocity of the charged particle becomes similar to that off the orbital electrons in the target material the Lindhard, Scharff, and Schiott (LSS) formulation based on a Thomas-Fermi atomic model becomes valid for estimating the total stopping power [95].

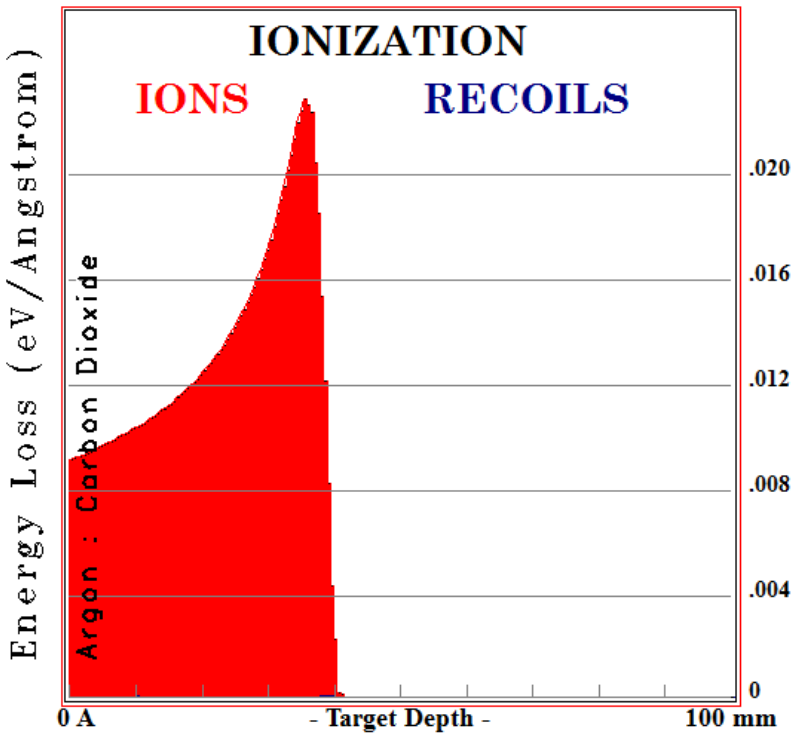

Figure 2.14: Bragg curve for α-particles, $\approx 5.3\,\text{MeV}$, in $ArCO_2$ (70:30) at atmospheric pressure generated with SRIM [61].

Electron recoils

Due to the mass matching between a primary ionizing electron and the orbital electrons in the target material it is interacting with, a much larger fraction of its energy can be lost in a single collision compared to heavy particles. The paths that result from this involve drastic changes in trajectories and rarely follow a straight line, and a similar formula to Eq. 2.23 can be derived [50]. Radiative processes can occur for fast electrons and scale with the electron energy and Z^2, where Z is the target material atomic number.

In general, electrons will lose energy at a much lower rate than heavy particles and travel greater distances. Although the range for heavy particles is fairly well defined, it is not for electrons due large differences in the track trajectories. An absorption coefficient can be defined as it relates to the count rate of electrons with and without an absorber material present, and range can be inferred from this.

2.4.2 Diffusion, drift, and the advantage of Negative Ion (NI) gases

In this section we will talk about movement of the primary ionization cloud once it has been produced via the initial interaction. Most particle detectors which rely on ionization must generate an E-field to move the charge to the readout. During this process the ionization will diffuse away from its initial shape, slowly losing information, and this is a limiting factor for directional detection with gaseous TPCs.

Drift velocity and diffusion

As mentioned, diffusion of the primary ionization cloud is one of the fundamental limitations of directional detection and every effort to suppress this effect should be considered. Essentially, if the diffusion grows beyond the length of the original recoil track, if any direction, then the primary axis can not be properly assigned to the ionization cloud. At this point we say that the directional information has been lost. From elementary kinetic theory we know that, due to their small mass, electrons at a given temperature will have a much higher, $\approx \times 1000$, diffusion coefficient than the corresponding ions. This substantial decrease in diffusion would allow the drifting distances in directional detectors to be increased, while still retaining vital track information, by a substantial amount. For instance, if the drift distance were able to increase by a factor of 10 while using the same readout then 10 more detectors could be built for the same price.

The drift velocity, v_d, is used to describe the average motion of a charge undergoing many collisions in an E-field and can be written as [33]:

$$v_d = \frac{eE}{m}\tau = \mu E \tag{2.25}$$

where τ is the average time between collisions, E is the field strength, and e and m are the drifting particles charge and mass, respectively. The second equality relates the mobility, μ for completeness. Essentially, the drift velocity is a macroscopic result of averaging out the random motion resulting from the many collisions occurring along the drift path resulting in a net motion along the E-field direction.

At thermal energies, or in the zero-limit of E-field strength, the diffusion coefficient, D, obtains the form in the Nernst-Townsend-Einstein relation:

$$\frac{D}{\mu} = \frac{kT}{e} \tag{2.26}$$

where T is temperature and k is the Boltzmann constant. As the field strength is increased deviations from this limit occur and, due to the low electron mass, they can be substantial for electron drift gases. Because the drift field increases the energy of the particles, the longitudinal diffusion along the drift direction, z, will always be greater than the transverse diffusion across the $x-y$ plane, it is the primary concern.

Using the diffusion coefficient, D, we can describe the variance of the distribution, which follows a Gaussian, by:

$$\sigma^2 = 2Dt = \frac{4\epsilon L}{3eE} \tag{2.27}$$

where $t = L/v_d$ and L is the drift distance and ϵ is the energy of the drifting particle. We can note that for an ideal gas at a given temperature, a less massive particle will have a higher velocity and spend less time in a given position. From Eq. 2.27 we can see that the diffusion coefficient is higher for particles spending less time in a given position, hence particles with lower mass diffuse more. For deviations from thermal diffusion it is typical to replace ϵ with $\epsilon_k = 2\epsilon/3$ which is the characteristic energy of the drifting media [100]. We note the thermal limit for σ^2 occurs when $\epsilon = 3kT/2$ resulting in:

$$\sigma^2 = \frac{2kTL}{eE} = 0.0257V \times \frac{L}{E} \tag{2.28}$$

where the second equality is at STP for reference.

Negative Ion (NI) gases

Because of the low velocity of the WIMPs, we expect relatively low amounts of energy, $\approx$ keV, deposited in our detectors. From a directional detection point of view, this means that many of the recoil tracks will be short, $\approx$ mm long. The shorter the recoil track the harder it is to assign a primary axis of travel. We want to make these short, low-energy recoil tracks as long as possible, in order to extract the most directional information per keV as possible. The way this is done in a gas detector is to lower the pressure, and this is where the idea of low pressure gas TPCs for directional dark matter arises. However, the lower the pressure is, the more the primary ionization cloud diffuses. This diffusion also makes it harder to assign a primary axis of travel.

The fundamental idea behind a NI gas is that the primary ionization attaches itself to highly electronegative atoms, or molecules. These negatives ions then transport the charge along the direction drifting E-field. Owing to the substantial increase in mass of the charge carriers, the diffusion is reduced. The negative ion then reaches the amplification stage where the electron is stripped off and avalanche multiplied, which is described in Sec. 2.4.3, into a macroscopic charge

signal and passed along to the readout. The details of the avalanche multiplication in NI gases are not well understood, and are currently being researched by multiple groups as discussed in Sec. 4.5.

There has been some work showing that the longitudinal diffusion in 40 torr of Sulfur Hexafluoride (SF_6) remains at the thermal limit for drift fields up to $\approx$ 800V/cm [87]. This is encouraging because it implies that directional information could be retained for sub-mm tracks drifting 10s of cm. However, achieving high avalanche gain with stable conditions remains an issue with these gases, as is discussed in Sec. 4.5.

2.4.3 Ionization avalanching

This section is a general discussion of the electron avalanching phenomenon in gases which we will refer back to in Chap. **??**.

Gas gain, or electron avalanching or avalanche multiplication, is an important phenomenon in particle physics as many different types of detectors are based on it. Generally, the incident particle energy, and hence the number of ion-pairs in the primary ionization, is low enough that some amplification is necessary before the signal can be passed to the readout electronics. In gaseous detectors the process of charge avalanching, which is also referred to Townsend avalanching, can be taken advantage of. In a strong enough E-field, drifting electrons can gain enough energy to overcome the ionization potential of the gas. Once this energy is surpassed inelastic collisions with neutral target atoms will produce secondary ionizations. This process is exponential, Eq. 2.29, since one electron can ionize many neighboring atoms, and the resulting signal can become macroscopic and passed along to the collection area of the detector. Fig. 2.15 is a cartoon of the avalanche process in a uniform field which will be studied throughout this thesis.

As shown in Fig. 2.16, this process has different operating regimes based on the strength of the E-field, ranging from no secondary ionization to uncontrolled avalanching, i.e. sparking. Sparking, in addition to damaging equipment and creating unwanted noise, breaks down the E-field and causes detector dead-time and if the rate of sparking is high enough the detector becomes inoperable, so this must be controlled.

In order to measure the energy of the incident particle detectors need to operate in what's known as "proportional mode" where the number of electrons after avalanching is proportional number created during the primary ionization. This is the depicted in Fig. 2.16 and is the region of study here. At lower field values secondary will not occur and lower still, the primary ionization starts getting absorbed so part of the original signal is lost. At higher fields, the number of secondary ions created in the avalanche can become large enough to inhibit the avalanche itself and this introduces nonlinear effects and the resulting pulse will not be proportional to the primary ionization in all cases. If the field is increased further still then the number of positive ions produced becomes large enough to change the field value below the threshold for avalanching to occur. This process is

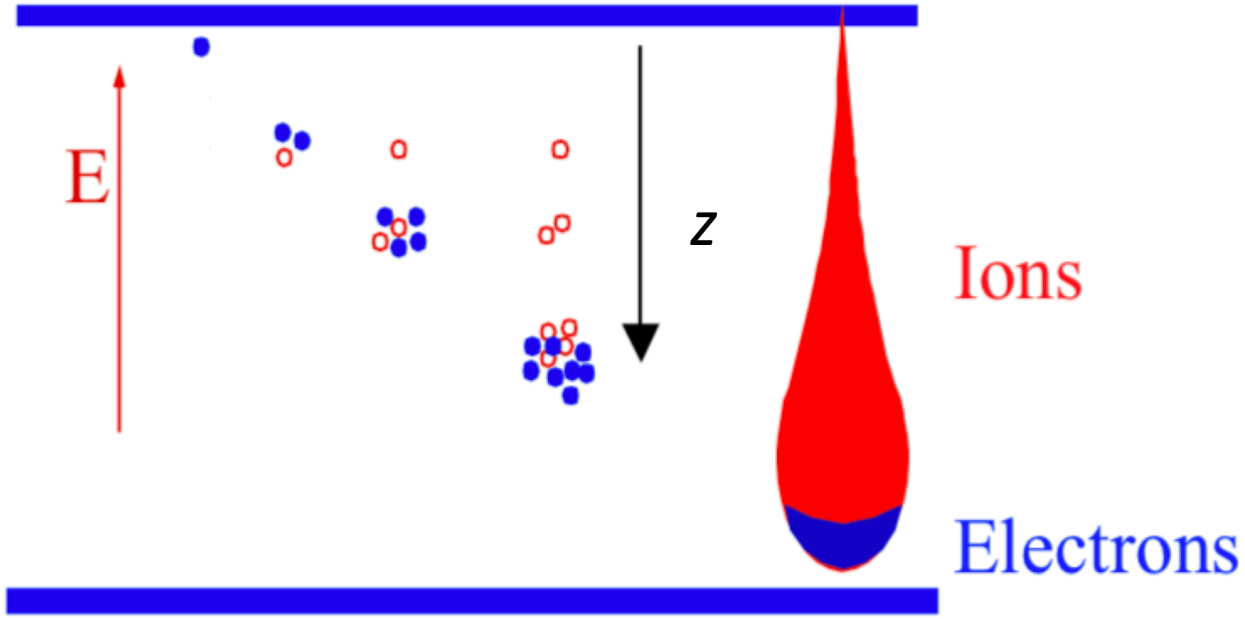

Figure 2.15: Illustration of the avalanche process. Taken from Ref. [92].

self-limiting and results in an equal magnitude pulse regardless of the amount of primary ionization and it is known as the Gieger-Mueller mode of operation [50].

In addition to creating secondary ionization, electrons colliding with neutral target atoms can also put them into simple excited states. These atoms will then return to their ground state by releasing X-rays or UV photons which then further ionize the outer shells of other atoms, and thus do not contribute directly to the avalanche. This "extra" ionization is undesirable in a proportional counter because it can lead to unpredictable pulses and a loss of proportionality. The way to control this effect is to minimize the amount of X-rays and UV photons the gas can produce and this can be accomplished by adding a molecular gas, CO_2 for example, with many degrees if freedom, i.e. vibrational and rotational modes, to the target gas. This molecular gas is known as a quenching gas [50].

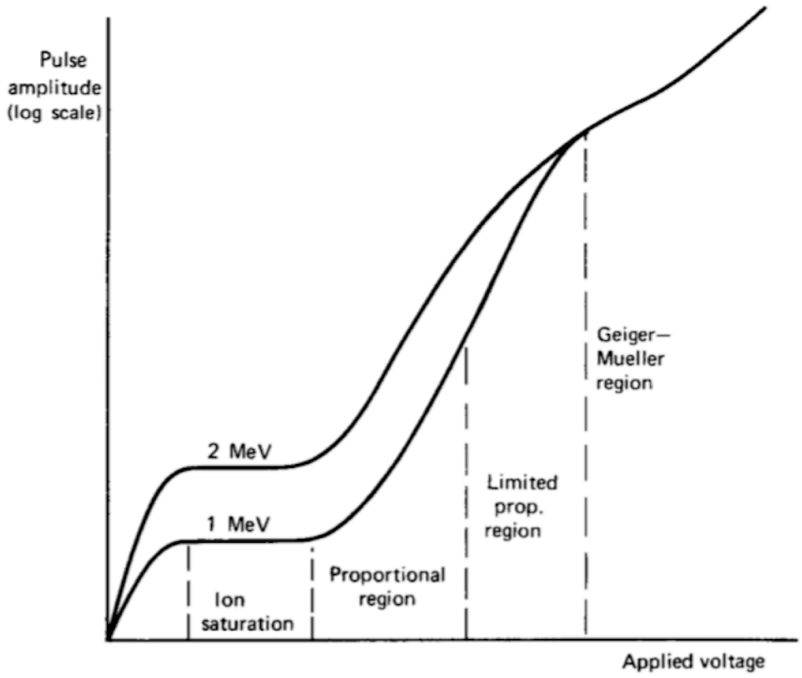

Figure 2.16: The different regions of the avalanching process. Taken from Ref. [50].

Quantitative description

The equation:

$$\frac{dn}{n} = \alpha dr \tag{2.29}$$

where n is the number of ion-pairs and r is the path length of the avalanche, is known as the Townsend equation [50]. The parameter α is known as the first Townsend coefficient and describes the fractional increase in the number of electrons per unit path length. In general, α is a function of the reduced field, $\frac{E}{p}$, where p is the gas pressure and has a value of zero if the field is below the value to create secondary ionizations. Note that some authors, [18], write this as $\frac{E}{N}$, where N is the gas density, for generality. The Townsend equation predicts that the number of electrons produced in the avalanche will increase exponentially with the distance. The gas gain is defined to be the ratio of secondary to primary ionizations, $G = \frac{n}{n(0)}$, and regardless of the exact form of α and assuming negligible contributions from recombination and space charge effects, we can write [43] [18]:

$$ln(G) = \int_{r_1}^{r_2} (\alpha) dr \tag{2.30}$$

where r_1 and r_2 are where the avalanche begins and ends, respectively. Our goal, then, is to

understand α and a summary of the classical argument in Ref. [18] follows.

Let λ_r be the component of the electron mean free path length along the electric field direction. Additionally, let λ_i be the mean free path length along the field direction the electron must travel in order to produce an ionization, or ionization path length. So, if $\lambda_r > \lambda_i$ a secondary ionization can occur. In a gas with no E-field, the distance between any two consecutive collisions of electrons and target atoms has an exponential distribution, [43] [48], which is a result of the velocity distribution being a Maxwell-Boltzmann. An alternative way to define the first Townsend coefficient, α, is the number of mean free paths per unit length along the E-field direction weighted by the probability that $\lambda_r > \lambda_i$:

$$\alpha = \frac{1}{\lambda_r} exp(\frac{-\lambda_i}{\lambda_r}) \tag{2.31}$$

The energy gained by the electron is equal to the charge of the electron, e, multiplied by the E-field integrated along the ionization path λ_i. If we neglect the energy differences from elastic scattering along the path, which should be small compared to the ionization potential, V_i, of the gas, and we assume that the E-field is constant we can write:

$$eE\lambda_i = eV_i \tag{2.32}$$

This turns out to be valid over a wide range of detector operating parameters. And it remains a valid approximation in proportional counters, where $E \sim \frac{1}{r}$, the field only varies $\approx 10\%$ from when the avalanche starts until the charge is collected on the wire [18]. Now if N and Q are the gas number density and the total cross section, respectively, we can write:

$$\frac{1}{\lambda_r} = NQ \tag{2.33}$$

If we finally assume that:

$$Q = C(E/N)^m \tag{2.34}$$

where C and m are dependent on the gas and $0 \leq m \leq 1$ then we can substitute Eq. 5.1 into Eq. 2.33, and then Eq. 2.33 and Eq. 2.32 into Eq. 2.31 giving:

$$\frac{\alpha}{N} = K\left(\frac{E}{N}\right)^m \exp\left(-L\left(\frac{N}{E}\right)^{1-m}\right) \tag{2.35}$$

where $K = hC$ and $L = hCV_i$ are experimentally fitted parameters, and h is ratio of λ_r to the full mean free path of the electron who's value is ~ 1 in an avalanching strength E-field. It turns out that many of the historical, empirically determined formulas are simple manifestations of Eq. 2.35, specifically, where they take on different values of m.

Diethorn's assumption was that $\alpha \sim E$, or that $m = 1$, [50] [45], and Williams and Sara used a more general form where $m = 0$ [110] which gives:

$$\frac{\alpha}{N} = A \exp\left(- B\left(\frac{N}{E}\right)\right) \tag{2.36}$$

where A and B are K and L, respectively, and note that $\frac{B}{A}$ gives back an "effective" ionization potential of the gas. There are other parameterizations of $\frac{\alpha}{N}$ with varying values of m, see Table 1 in Ref. [18].

What Eq. 2.35 tells us is that as m is scaled from 1 to 0 the reduced Townsend coefficient goes from a simple linear dependence on the reduced field to an exponential dependence, and all values of m seem to work well within limited ranges of the reduced field with a constant field. Indeed, in the operating range of any single detector, taking $m = 1$ is a valid assumption and allows for a very intuitive interpretation of the data, see Eq. 4.1, however, as we'll see in Sec. 4.3.2, once the parameter space is broadened the more general approach of Eq. 2.36 will be needed.

CHAPTER 3
DETECTOR PROTOTYPES IN HAWAII

3.1 Motivation for the Directional Dark matter Detector (D^3) prototypes

Directional detection is still in its infancy as a field, and many of the ideas are either in, or just advancing out of, the proof-of-concept stage. Small prototype detectors allow us to evaluate these ideas and determine which are viable, and which need rethinking. This chapter will discuss the various small prototypes used for gain measurements at the University of Hawaii. This chapter, including the design and construction of prototypes, and the next chapter, including all gain measurements and analysis, represent the core of the author's work.

Because of the low relative velocity between our detector target and incoming WIMPs, the resulting low-energy recoil ionization tracks will be short, on the order of a few mm. We operate Time Projection Chambers (TPCs), to be described in Sec. 3.2.1, with low pressure gases in an effort to make the low-energy tracks as long as possible. Our TPCs use Gas Electron Multipliers (GEMs), described in Sec. 3.2.2, and pixelized charge readout, discussed in Sec. 3.2.3. This results high resolution vector 3D ionization cloud (track) reconstruction with no noise, see Figs. 2.9, 3.4, 2.8, and appendix D for examples.

3.2 Principle of detector operation

3.2.1 Time Projection Chambers (TPCs)

A Time Projection Chamber [76] (TPC), in the most basic sense, is an ionization chamber. A incoming particle enters the target medium and interacts, and this interaction produces some primary ionization. This ionization is then drifted, in an electric field, to some sort of readout device and, depending on the readout, various measurements of the interaction can be made. Fig. 3.1 shows a schematic of one of our prototypes, where the readout is a pixel chip. The GEMs, discussed in the next section, are for amplifying the charge signal to a macroscopic level. The cathode, along with the field cage rings produce the E-field which is responsible for drifting the charge down to the GEMs.

Specifically, a TPC is a sophisticated extension of the Multi-Wire Proportional Chamber (MWPC). In a MWPC a layer of fine pitch wires is placed in a plane perpendicular to the drift field which allows for position measurement in the wire plane. In addition to this a TPC records and digitizes the ionization signal and its arrival time as it encounters the wires. Using the drift velocity of the medium, the timing information can be reconstructed into a relative z coordinate. So a

TPC "projects" the z coordinate onto the wires. This allows for 3D reconstruction of events inside the detector and, depending on the resolution of the readout, can provide exquisite detail of the ionization distribution from single events.

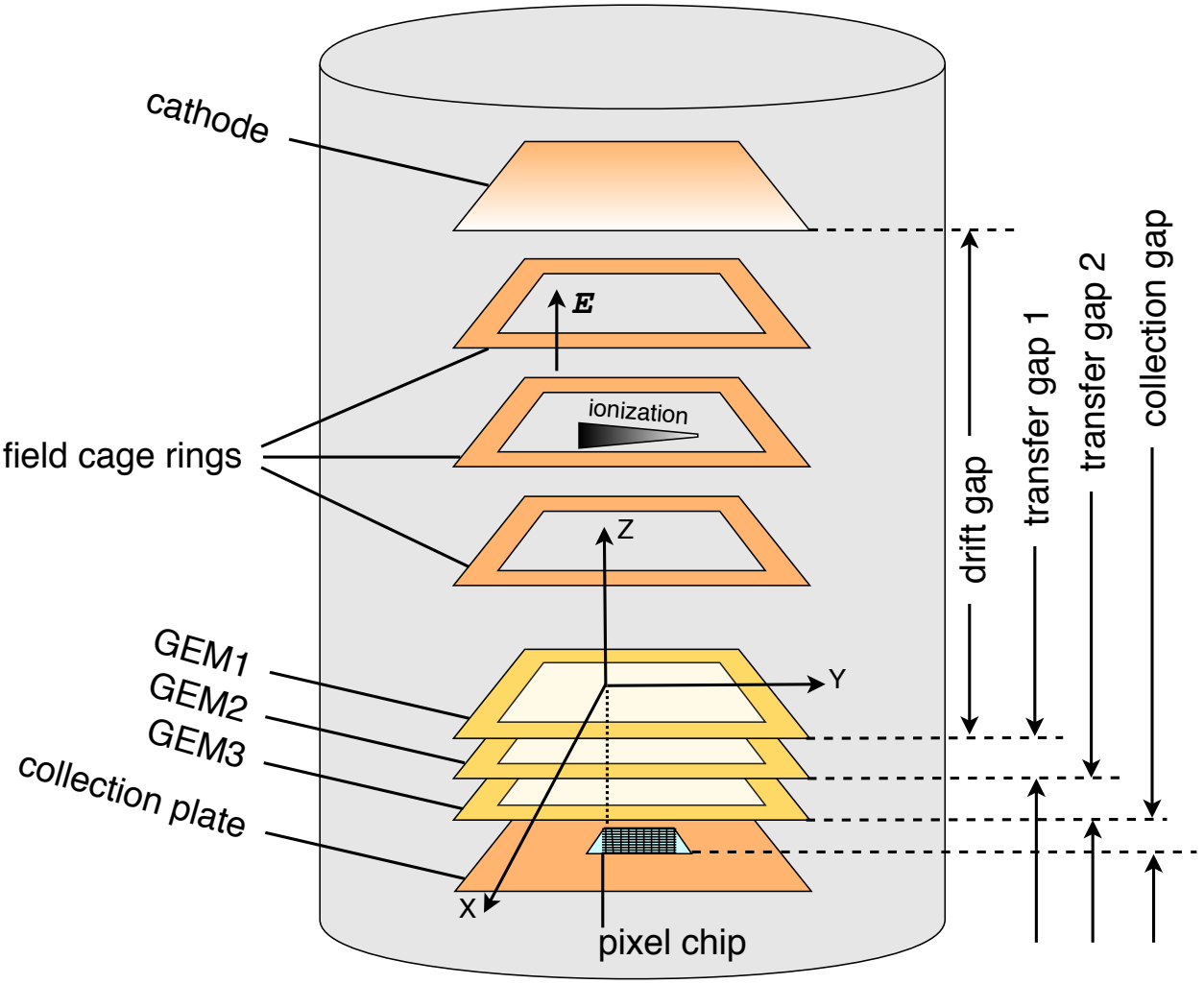

Figure 3.1: A schematic for our prototypes and definition of the coordinate system used for pixel chips measurements. During gain measurements the pixel chip was replaced with an aluminum or copper plate. The dimensions are not to scale for clarity.

3.2.2 Gas Electron Multipliers (GEMs)

GEMs [91] take advantage of the ionization avalanching process discussed in Sec. 2.4.3 and consist of a composite grid of two metal layers separated by a thin insulator. Generally, the composite layer is framed inside a rigid insulator and electrodes are attached to the two metal layers, see Fig. 3.2, allowing for an E-field of avalanching strength to be established.

Depending on the thickness of the GEM, they are manufactured differently. Thin GEMs, usually 50 μm thick, are coated with photoresist, exposed to light through a mask, and then the metal is acid etched from both sides until through holes are created. As the thickness increases the holes can be drilled through with tiny drill bits.

Based on the authors experience, thicker GEMs are easier to work with and much more robust as the thin GEM foil can easily be distorted. Attaching leads to the electrodes is also more difficult with thinner GEMs and it is usually beneficial to create an additional rigid frame to mount the voltage leads to. However, thinner GEMs are able to maintain a much higher field and, generally, achieve better resolution than thicker GEMs. Two types of GEMs were used in the D^3 prototypes and their details are in Table 3.1.

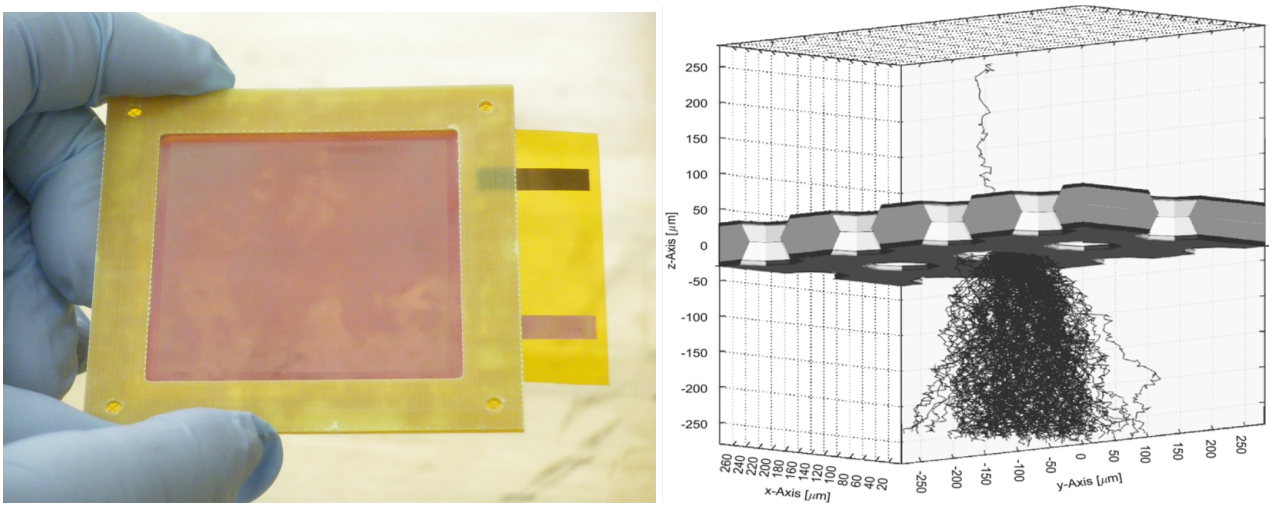

Figure 3.2: Left: A thin GEM used in our prototypes. Note the two electrodes off of the right side for powering each side of the GEM. Right: Garfield simulation of electron avalanching in a thin GEM.

Table 3.1: GEMs used in D^3 prototypes.

GEM type	Thickness (cm)	Active area (cm)	Hole diameter (cm)	Pitch (cm)
Thin GEM	0.005	5×5	0.007	0.0014
THGEM	0.04	5×5	0.03	0.05

3.2.3 Charge readout via ATLAS pixel chips

Pixel chip operational details

After the GEMs produce a macroscopic charge signal, it can be detected with an ATLAS pixel ASIC ("chip"). Both the ATLAS FE-I3 and FE-I4B pixel chips were used in different prototypes

and exhaustive details about them can be found in Refs. [2] and [40]. The active area of the chip is divided into small pixels, see Table 3.2, each consisting of an integrating amplifier, a discriminator, a shaper, and associated digital controls. The chips sample at a frequency of 40 MHz and operate in what's known as self-trigger mode, which is defined next. The definition of charge being detected is that at least one pixel goes above threshold, which is adjustable, and this self-trigger generates a serial stream that encodes the $x - y$ position, arrival time, and amount of charge collected for each pixel that is over threshold for the next number of cycles of 25 ns each. The number of clock cycles to be read out can be adjusted, for FE-I3 it was up to 16 while the FE-I4B can operate with 16 or 256. The time over threshold, ToT, is used to measure to amount of charge that is collected to 4-bit precision, in both chips.

The chips have several tuning scans that can be preformed along with a small injection capacitor. To relate the ToT to the actual charge detected a ToT calibration is preformed. This scan records the mean ToT value for 200 injections of charge, in internal chip units, into each pixel. This is done for 13 different values of charge (chip units). Then the mean ToT for all of the pixels is computed for each of the 13 values. The internal chip unit of charge is converted into an electron charge using a conversion unique to each chip. Finally, the computed ToT is plotted against the converted electron charge to give a relationship between the two quantities.

There is a similar scan to set the threshold of the chip where the user selects a desired threshold. Charge is injected to each pixel multiple times and is averaged for each pixel, and then for the entire chip. The threshold is generally chosen to be as low as possible without allowing any pixels to self-trigger on undesired noise.

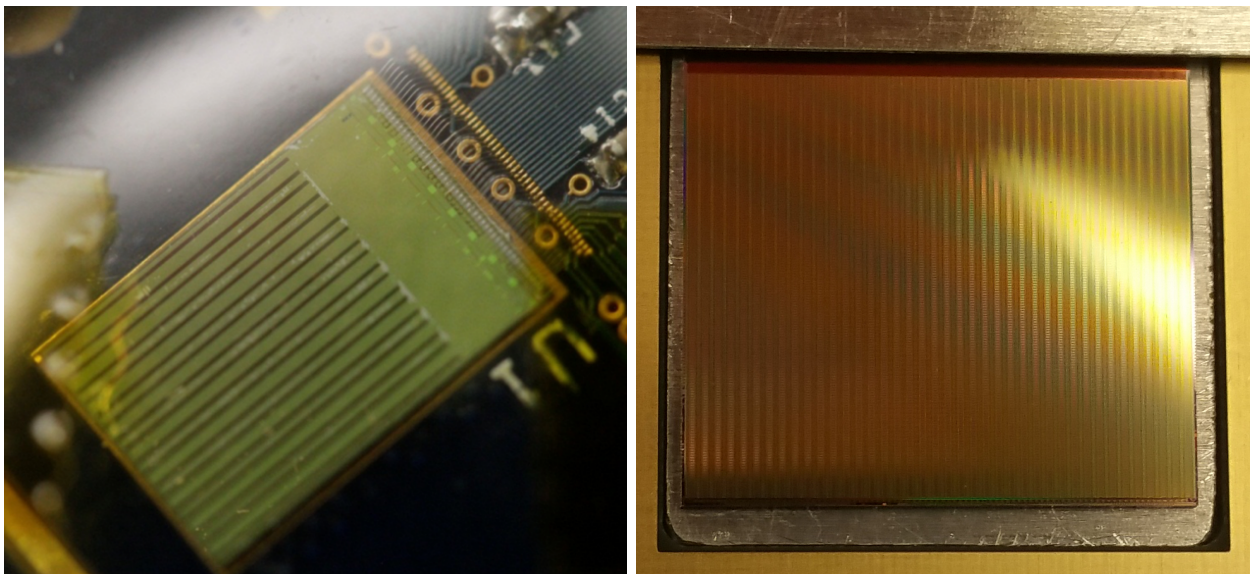

Figure 3.3: ATLAS pixel chips. Left: FE-I3. Right: FE-I4B. See text for descriptions.

Table 3.2: ATLAS pixel ASIC "chips" dimensions.

Chip	Active area (cm)	Number of pixels	Pixel size (μm)	Column $\times$ row
FE-I3	0.72 $\times$ 0.80	2880	400 $\times$ 50	18 $\times$ 160
FE-I4B	1.68 $\times$ 2.0	26880	250 $\times$ 50	80 $\times$ 336

Event reconstruction

Event reconstruction is as follows: The primary ionization cloud drifts in an E-field created by the field cage. The primary charge is avalanche multiplied by a GEM layer, which could consist of a single or multiple GEMs, and detected by an ATLAS pixel chip which starts the digitization procedure described in Sec. 3.2.3. The $x-y$ coordinates of the events are defined by the row and column number of the incident pixel and multiplied by their corresponding dimension. The z coordinate is quantized into 250 μm segments defined by 25 ns time-bins and the drift velocity of the target medium. The events are then readout out using the the appropriate DAQ system and controlling software, [107].

Performance

Since the drift velocity in the gas is known then the timing information can be converted into a relative position in the drift direction, z. Relative is mentioned because the because the digitization starts only when the event is self-triggered, so the time, hence position, is only known relative to the start of the event. There are methods to get the absolute z position including using the different drift velocities of different gas species [25], and, in our case, using the high granularity of the pixel chip itself [72]. This is a crucial development allowing for full 3D fiducialization, which allows for complete background rejection, which is necessary in the search for dark matter, and will be exploited in Sec. 5.4.2.

Fig. 3.4 shows the FE-I4B readout plane with three separate events, from experimental data, superimposed. The event discrimination here is evident not only by the amount of ionization detected, the color scale, but also by the track length and topology. The long track going across the entire plane of the chip is from a ^{210}Po α-particle which deposits MeV amounts of energy in the detector. These mono-energetic particles are useful for monitoring detector stability and are easily rejected based on their tracks crossing the edge of the fiducial volume.

The other longer track, that is fully contained to the plane of the chip, is a Helium nuclei recoiling from an interaction with a neutron. Nuclear recoils are distinguished from the through-going α particles by requiring them to be fully contained to the plane of the chip. Also, due partly the limited momentum transfer in the collision, nuclear recoil energies are typically less (much) than MeV scales and, as a result, these recoils lie closer to the Bragg peak. The recoil shown in

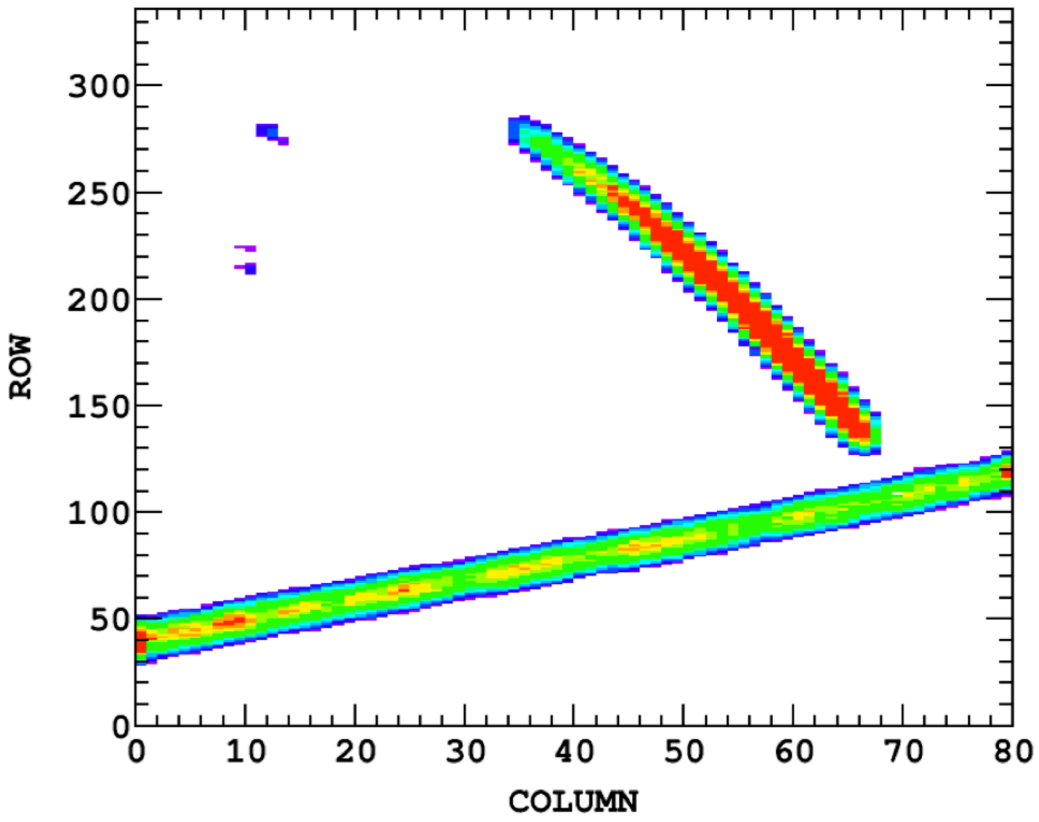

Figure 3.4: FE-I4B readout plane featuring three superimposed events. Top left: An electron recoil $\approx 70\,\text{keV}$. Top right: Nuclear recoil $\approx 500\,\text{keV}$. Bottom: An α-particle $\approx$ MeV. Color is the TOT (charge) scale, red is more, blue is less.

Fig. 3.4 deposited an energy in the detector of $\approx 500\,\text{keV}$, and there is a clear difference in the amount of charge deposited on one end of the track vs. the other displaying the head-tail signal discussed in Sec 2.3.1.

The third event is an electron recoil and their discrimination against nuclear recoils is what limits the low mass WIMP reach of these detectors. The one displayed is $\approx 50\,\text{keV}$ but at lower energies these begin to look identical to nuclear recoils. A future study will likely use the full 3D event topology as the electrons tend to lack a continuous ionization distribution due to the erratic nature of their tracks.

3.2.4 Pulse-height measurement device

For the gain measurements, discussed in Chapter 4, the pixel chip was replaced with a metal plate as a charge collection device. This was then connected via an amplifier chain to a multi channel analyzer operating in pulse-height mode. This is detailed in Sec. 4.2. This is done to study the gain process itself without any additional noise accompanying the pixel chip and readout. This gain measurement, and the corresponding gain resolution measurement, serve as benchmarks for detectors operating with GEM amplification should strive for.

3.3 General prototype design and features

3.3.1 D^3 - overview and naming scheme

D^3 was envisioned to be a 1 m^3 directional dark matter detector. With that in mind, we have adopted the following naming scheme for our prototypes: The dimensions of the FE-I3 chip are $\approx$ 1 cm^2, and with a 1 cm drift gap results in a $\approx$ 1 cm^3 fiducial volume. This is $1{\times}10^{-6}$ of 1 m^3, the volume of D^3, so this prototype is called D^3 - Micro. The next prototype employed the, $\approx$ 4cm^2, FE-I4B chip with a larger drift gap and is called D^3 - Milli. Each prototype also underwent iterations, i.e. there was a major structural change or repurposing, these are denoted as stage 1, stage 2, and so on.

Although the material, orientation, and dimensions vary between the detectors under discussion, they all have a drift region, GEM amplification region, and a collection region, see Fig. 3.1 for a cartoon of a setup and Table A.2 for specific dimensions. Prototypes with multiple GEMs have a transfer gap between the GEMs. The numbering scheme for all quantities is as follows: The item with the highest absolute potential is numbered 1, the next highest is numbered 2, and so forth. For instance, in the triple GEM setup, GEM1 has a higher potential than GEM2 which has a higher potential than GEM3. The gap between GEM1 and GEM2 is transfer gap 1 and the gap between GEM2 and GEM3 is transfer gap 2. Transfer gap 1 is at a higher absolute potential even though it may have the same field as transfer gap 2, and if there is only a single transfer gap the number is omitted.

3.3.2 Mechanical support structure

All prototypes consisted a of Delrin, acetal, support structure, the white or off-white pieces in Figs. 3.7, 3.8, 3.9, and 3.10. For all prototypes, an aluminum baseplate was used as a foundation to mount the Delrin support structure to. Holes were tapped into the baseplate allowing either 0.25" or 0.125" threaded Delrin rods to be inserted. Flat, $\approx$ 2 mm thick, Delrin pieces were machined as mounts for the various GEMs and mesh, if needed. The GEMs, and the GEM HV leads, were then attached with small nuts and bolts to the thin Delrin pieces. These assembled pieces were

then mounted to the threaded Delrin rods fixed to the baseplate. All distances along the threaded rods were fixed by the use of small Delrin spacers which were machined to our specifications. All field cage rings, the anode, and the cathode were held apart via these spacers as well. Once all the parts were "slid" onto the threaded Delrin rods, the entire structure was "squeezed" together by tightening the appropriate size Delrin nuts down the rods onto the structure. All prototypes were assembled in a clean room and then transported into vacuum vessel where all feedthrough connections were assembled.

A note on material choices

With gas detectors, in general, low outgassing materials are sought after. In our case, the gain is sensitive to impurities at the ppm, or ppb, level so we try to adhere to the NASA low outgassing materials guide [67] when choosing materials for detector components. As mentioned above, white Delrin is used for all structural support aside from an aluminum baseplate. Low outgassing Teflon or Kapton coated wire was used all HV connections. Teflon seems to perform better over time as the Kapton becomes very brittle and tends to crack. Kapton tape is used liberally around the GEM and other HV leads, but outgassing is seen to increase when large amounts of Kapton are introduced so its use should be limited to the tape. A general, maybe obvious, statement on material usage is that, unless using more material serves a necessary operational or scientific purpose, less material should be used.

3.3.3 Vacuum vessel

All of the prototypes were housed in a stainless steel vacuum vessel, see Fig. 3.5, that was custom manufactured by Huntington Mechanical Laboratories. The internal dimensions are $\approx 45 \times 15\,\mathrm{cm}^2$, height $\times$ radius, or $\approx 30\,\mathrm{Liters}$ in volume. The collar features six KF-40 ports symmetrically arranged around the vessel, and there is another KF-40 port located on the lid all which use Viton o-rings. All of these allow for a variety of different feedthroughs and devices to be connected.

3.3.4 Gas system

0.25" stainless steel tubing with Swagelok fittings and valves were for all gas inlet and mixing points. Stainless steel corrugated tubes with KF-40 connections were used for evacuation routes via a combination roughing and turbo pump (Drivac BH2-60HD). During certain measurements, gas flow was needed to counter high detector component outgassing. This was achieved either via a 0.25" silicon tube connected directly to the building exhaust, or via a 0.25" copper tube connected to another combination vacuum pump for gas flow at atmospheric, or low pressure, respectively.

A gas mixing manifold was used to connect up to four different gases to the vacuum vessel inlet. N_2 was generally used to flush out any target gas before opening the vessel to the laboratory

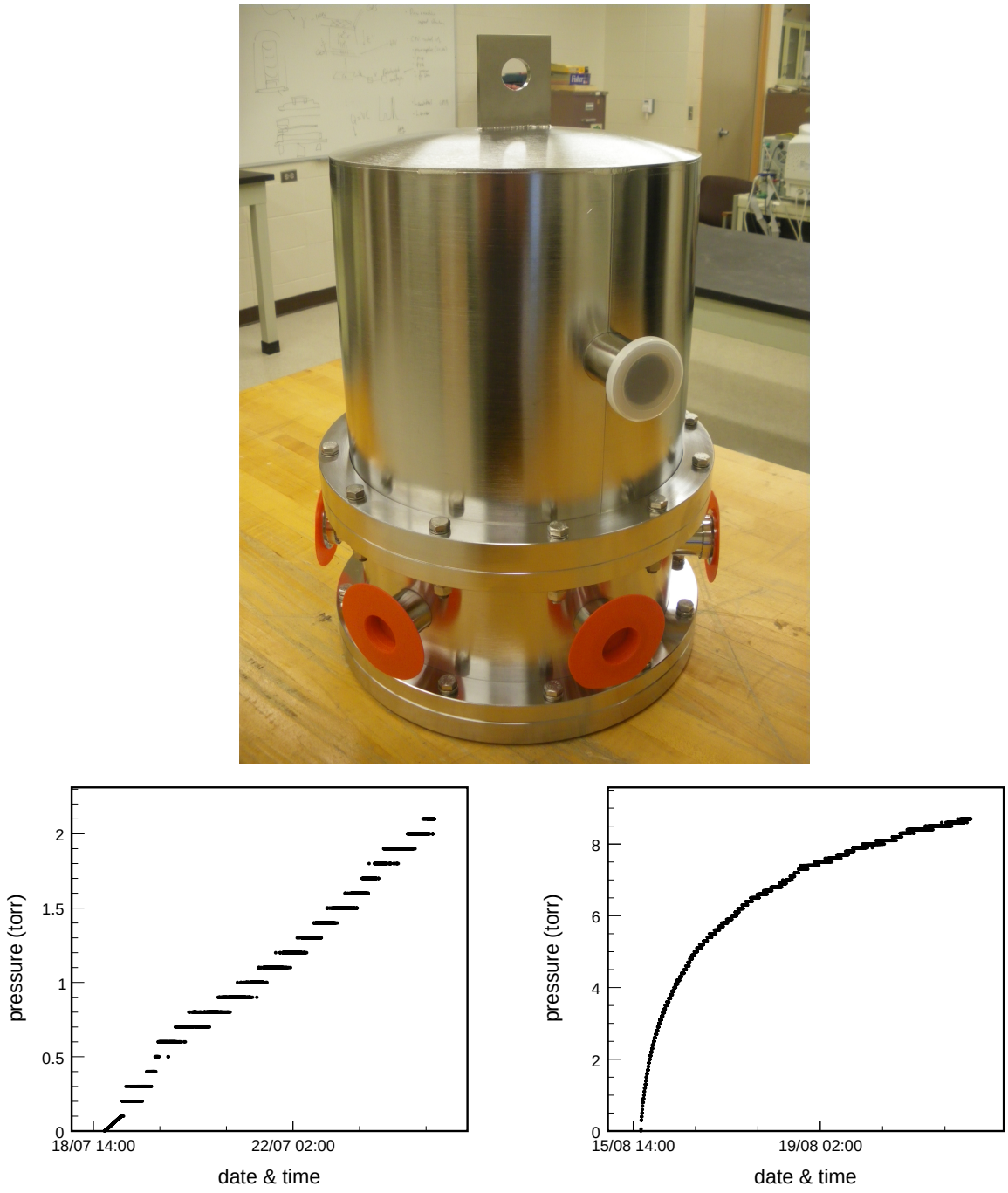

Figure 3.5: Top: $\sim$ 30 Liter stainless steel vacuum vessel used to house the D^3 prototypes. Bottom: Outgassing curves for the stainless steel vessel. Left: Empty vessel. Right: With the D^3 - Milli stage 2, Sec. 3.4.3, setup installed.

environment. Also connected were any gases being used for measurements so we could easily switch from one to another.

3.3.5 HV supplies and power scheme

Multiple different power supplies were used for the various prototypes, and they included: Keithley model 248 (5kV), SRS model PS370 (20kV), and a Caen NDT1470 (8kV). This is mentioned simply to note that the Caen supply, while less robust against discharges, produced less noise on the pulse-height spectra than the others.

A resistive divider was always used to supply voltage to the GEMs and as a result, the transfer and collection gap(s) voltages, $V_{transfer1,2}$ and $V_{collection}$, vary with GEM voltage, V_{GEM}. In some of the setups the drift field was created by extending the GEM resistive divider with an additional HV supply as illustrated in Fig. 3.6, and in the others the drift field was created by simply supplying the cathode, and each ring, with its own separate HV channel. Either way, the drift field was always independent of V_{GEM}. See Table A.5 for the prototype specific voltages and table A.1 for the power schemes and field cage setups.

3.4 A chronological timeline of work in Hawaii

This section will detail the individual prototypes as they were assembled. Issues including electronic noise, high material outgassing, and poor gain performance will be discussed as they relate to the specific prototypes. The hope is to paint a picture of the thought process moving from one prototype to the next.

3.4.1 D^3 - Micro - our first prototype (2011 - 2013)

The D^3 - Micro prototype, Fig. 3.7, was the first detector assembled by our group at the University of Hawaii and the design closely follows that of an earlier prototype constructed at LBNL [65]. Visible in the left plot in Fig. 3.7 is the copper collection plate which surrounds the pixel chip. This was used for the some of gain measurements in Sec. 4.3 and all of the $ArCO_2$ in Sec. 4.4. This prototype was also used for the reconstruction of the position of a ^{252}CF neutron source via directionally reconstructing the helium atom recoil tracks from collisions with neutrons using the FE-13 ATLAS pixel chip, Sec. 3.2.3, see Ref. [108] for details.

D^3 - Micro operated successfully from 2011 - 2013 and ran stably for weeks at a time during which the gain was stable enough, to the few % level, to correlate any changes with the temperature in the lab. During this time the ATLAS FE-I4B pixel chip, Sec. 3.2.3, also became available. Because the circuit boards that the chips were connected to had different dimensions, and a longer drift length was desired, a new prototype was designed and constructed, D^3 - Milli stage 1.

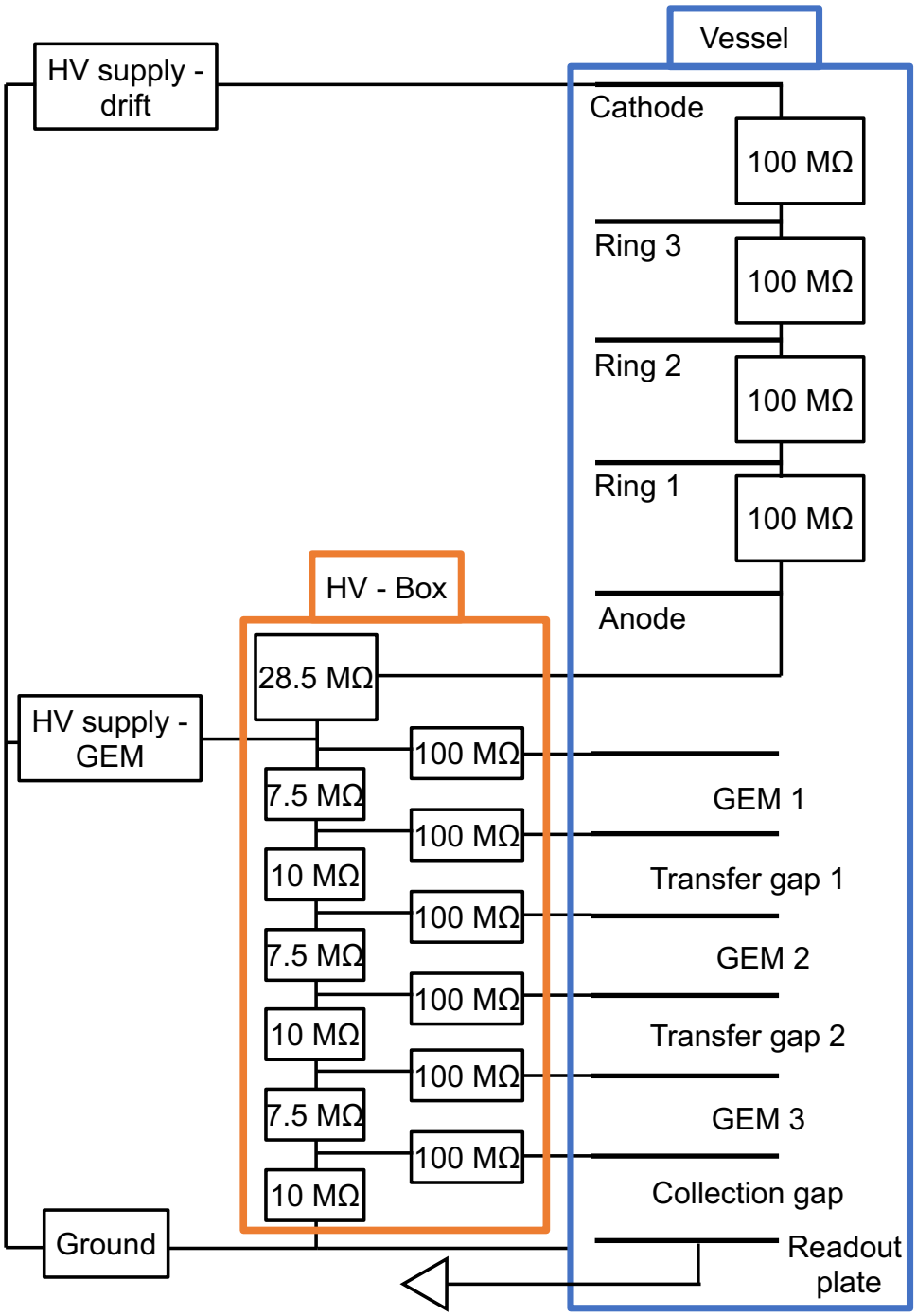

Figure 3.6: The high voltage scheme used for the D^3 - Milli1, Sec. 3.4.2, triple prototype. A similar resistive divider was used in all prototype unless otherwise noted. The 100 MΩ resistors on the GEM leads are to protect the GEMs against discharging.

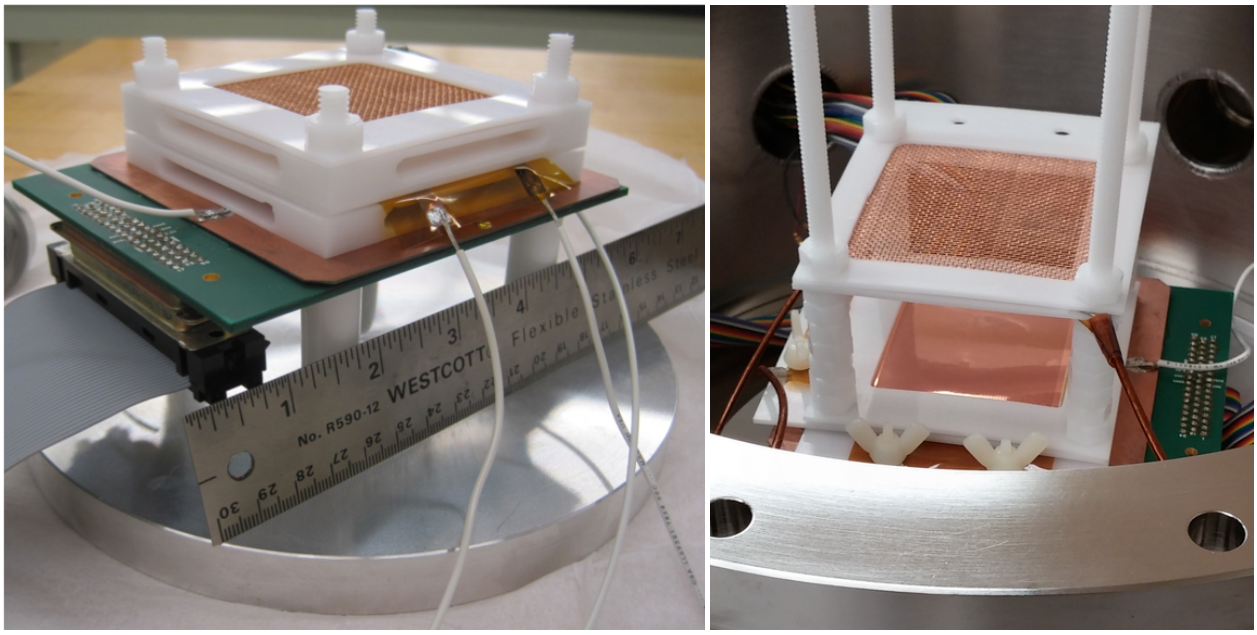

Figure 3.7: D^3 - Micro prototypes. Left: Shown with a drift gap of 9.2mm; used for all the gain studies. Right: Shown inside the vacuum vessel with an increased drift gap of 45mm; used for directional neutron measurements, [108]. Also shown is the circuit board, (green), to which the ATLAS FE-13 pixel chip is wire bonded.

3.4.2 D^3 - Milli stage 1 (2014 - 2017)

Although designed around the FE-I4B chip, this prototype was mainly used for gain studies as the BEAST II TPC prototype [62] was being built in parallel which would make its primary use the FE-I4B chip. This prototype operated successfully with both a triple thin GEM and a single THGEM setup installed, see Fig. 3.8. A large portion of the measurements discussed in Sec. 4.3 and our first SF_6, a Negative Ion (NI) gas, gain measurements were taken with this setup, see Sec. 4.5 for details.

A note on electronic noise

Up to and including the early operation of this prototype, electronic noise was a major issue that manifested itself as a "wall" on the low end of the pulse-height spectra. While using the high gain double and triple thin GEM setups of D^3 - Micro and D^3 - Milli stage 1, respectively, the gain was simply increased to where the signal-to-noise ratio allowed for successful measurements. However, it was necessary to resolve this before successful operation with THGEMs could occur.

Multiple components comprised this noise, and not all are fully understood, but a decrease of an order of magnitude was achieved to allow for successful low gain measurements in 2017. The grounding connection between the preamp housing and steel vessel turned out to be a major

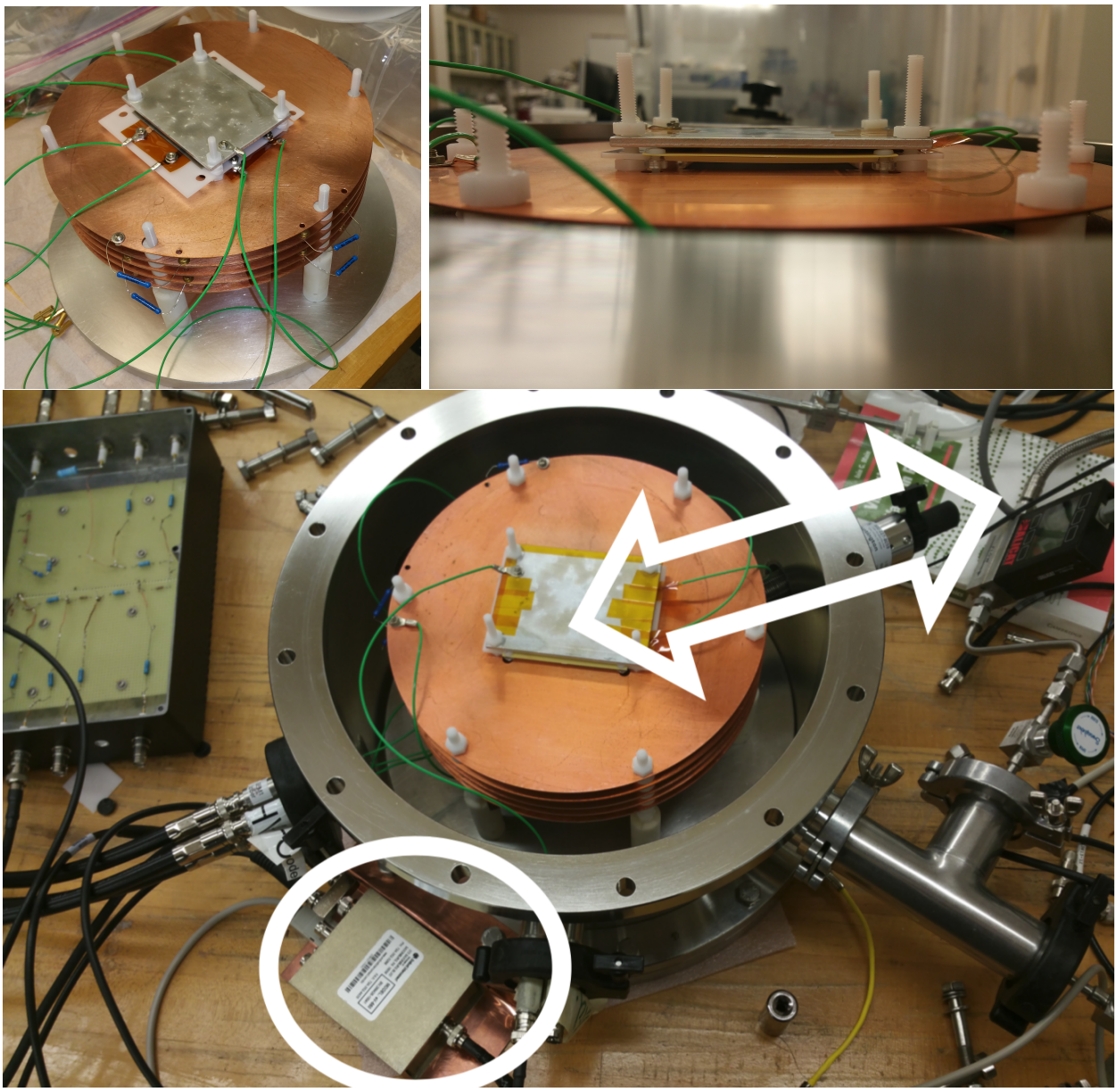

Figure 3.8: D^3 - Milli stage 1. Upper left: Triple thin GEM setup. Upper right: Single THGEM setup. Bottom: Improvements made to allow for single THGEM operation. Inside the white oval is the improved grounding connection for the preamp housing, and the white arrow inscribes the spring loaded feedthrough allowing for source on/off measurements, see text for discussion.

component. The shielding of the BNC cable was inadequate and the preamp housing was mounted to a copper plate which was then bolted to the vessel itself. The improvements can be seen by comparing the spectra in Fig. 4.2 and Fig. 4.6, which use the same source, gas, and pressure, by noting the channel number on the horizontal axis. In the thin GEM spectra, with high gain, the

noise floor extends up into the 100s while in the THGEM spectra, with low gain, this is the signal region.

Another major noise component, which took a long time to sort out, were mechanical vibrations. While some of this could be controlled simply by using different pulse shaping times, it was discovered having the vacuum pump turned off helped greatly with noise reduction. Yet another crucial improvement for low gain operation was the installation of a spring loaded feedthrough that could move laterally from near the vessel wall to the center. The ^{55}Fe source was attached to this inside the vessel and could now be turned "on" and "off" by moving it to certain positions, see Fig. 3.8. So, starting with the single THGEM setup background measurements were a possibility.

D^3 - Milli stage 1 operated well for years, 2014 - 2017, but suffered from high outgassing due to the larger amount of material used compared to D^3 - Micro which can be seen in the gain stability plots in Fig. 4.3. To some extent this could be controlled with gas flow, and while it wasn't a major issue with the triple thin GEM setup it became a problem with a single THGEM because of the gain limitation. To date, the author has yet to achieve measurable gain in SF_6 with thin, 50 μm GEMs, so using THGEMs became a priority and a new, lower mass, prototype was constructed.

3.4.3 D^3 - Milli stage 2 (2017 - 2018)

By 2017, the BEAST II prototypes had operated successfully operated in the commissioning of the SuperKEKB upgrade, [71], and extra field cage rings were available. These rings were much smaller and throughly tested so they were used in stage 2. While this setup did produce much lower outgassing, the electronic noise again became an issue. Although the exact mechanism is not well understood, there is some mechanical coupling between the HV components and the metal readout plate which can render the detector inoperable. This is possible because the readout plate is mounted to same support structure as the GEMs and field cage. While testing with no collection gap the GEM was mounted directly to the readout plate, and when powered on the noise swamped the entire signal region. It is suspected that mounting the readout completely independently of the HV components would be best for future operations. Note that the pixel chip does not seem to be vulnerable to this effect.

D^3 - Milli stage 2 was used to take the remainder of the measurements in Sec. 4.3 and the lower picture of Fig. 3.9 shows it inside the stainless vacuum vessel with the visible source holders . On the right is the ^{55}Fe that can be moved below the mesh as the source "on" position or near the vessel wall as source "off". On the left is the ^{210}Po source fixed to a feedthrough which can rotate 360°, placing it in the "on" position, as shown, allows α-particles to enter the drift region while rotating it 180° places the α-particles well below the mesh.

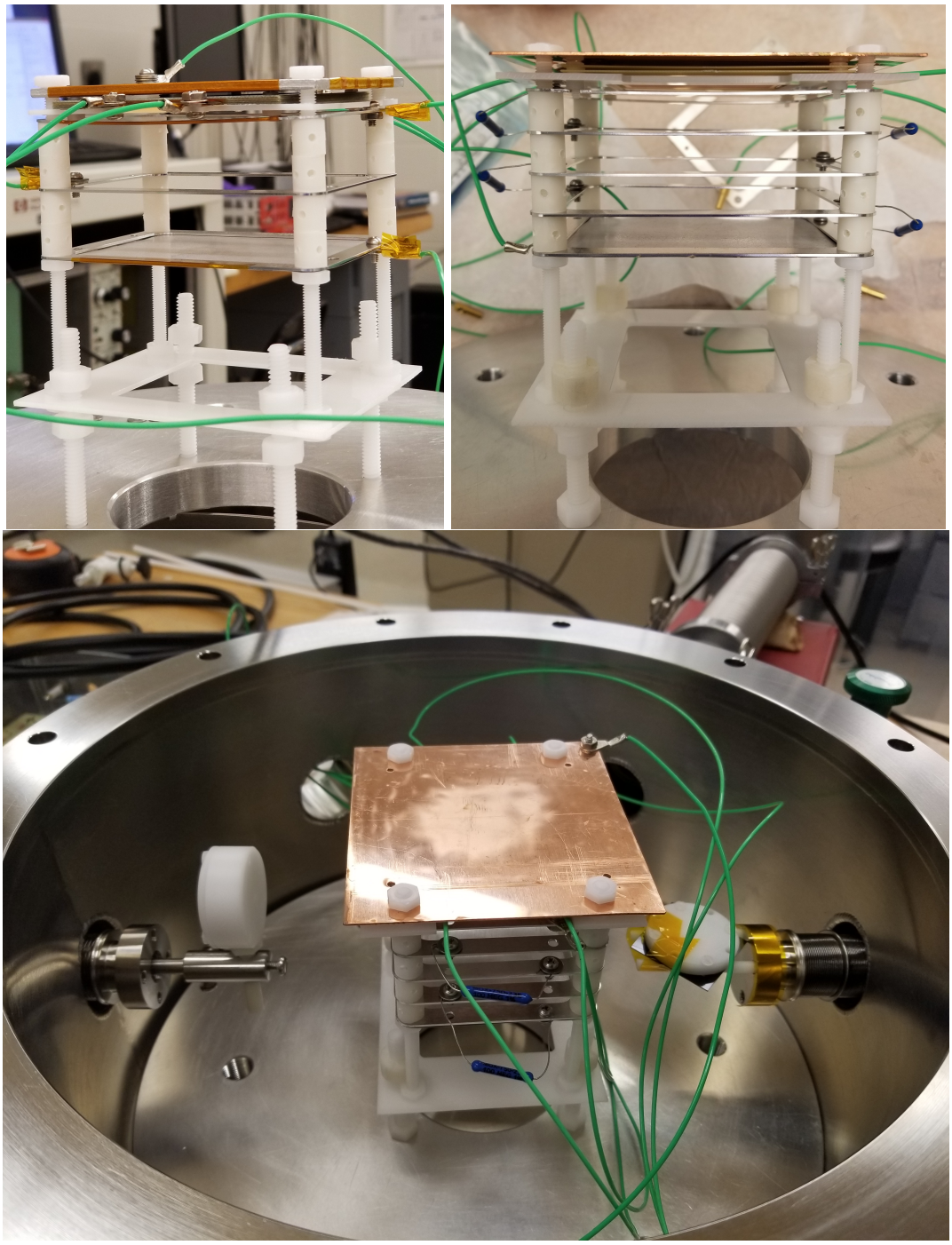

Figure 3.9: D^3 - Milli stage 2. Upper left: double thin GEM setup. Upper right: double THGEM setup. Lower: Inside the stainless vacuum vessel with the source holders.

3.4.4 D^3 - Milli stage 3 (In progress)

During the measurements with the previous prototypes our group started learning about the advantages of Negative Ion (NI) gases as they relate to directional dark matter detection, see Sec. 2.4.2. With this consideration, it was decided to move to a new vacuum vessel which was longer and made of a non-metallic material, and the 48" acrylic vessel in Fig. 3.10 was chosen. The diameter was chosen to accommodate four GEM/pixel chip setups arranged in a square, see Fig. 3.11. The pixel chips could be connected together (multiplexed) and this would be the proof of concept for scaling up to larger detectors. A 30 kV power supply and feedthrough were procured which would accommodate drift lengths up to 60 cm, and would likely allow for obtaining the maximum drift length that is achievable in a NI gas while still retaining directional information.

The overall design concept is that the field cage, along with the GEMs and readout, would be assembled into a single structure in the clean room and then slid inside the acrylic vessel, and this is the purpose of the large "donut" spacers in the bottom picture of Fig. 3.11. These spacers protrude outside the OD of the rings and are the contact points with the interior of the acrylic vessel, and with the endplates removed two people could easily slide in a large field cage assembly.

The endplates were designed such that the HV field cage lead would be isolated from everything else and the top left picture in Fig. 3.10 shows the two endplates. Seven KF-40 nipples were welded onto a 1/2"×15"×15" steel plate and the plate was then bead blasted to remove any debris. The HV endplate is a 3"×15"×15" acrylic plate with a single KF-40 feedthrough mounted in the center. O-ring grooves were also also designed and tested with aluminum test plates before the final endplates were started. Both endplates are supported upright by wooden frames so that they can easily slide around when assembly/disassembly is required. The wooden frames were constructed such that the o-rings line up with the edge of the acrylic when slid together to form a vacuum seal, see the top right plot in Fig. 3.10 for the outgassing curve. The long steel rods shown the bottom of Fig. 3.10 have nuts on each end to provide the initial seal as they clamp both endplates to the vessel, and they have since been replaced with fiberglass rods due to sparking concerns. A polycarbonate shield was also constructed to further isolate the 30kV feedthrough. Although the parts, and some test assembly, have been completed, the author ran out of time to attempt any measurements aside from the outgassing of the empty acrylic vessel.

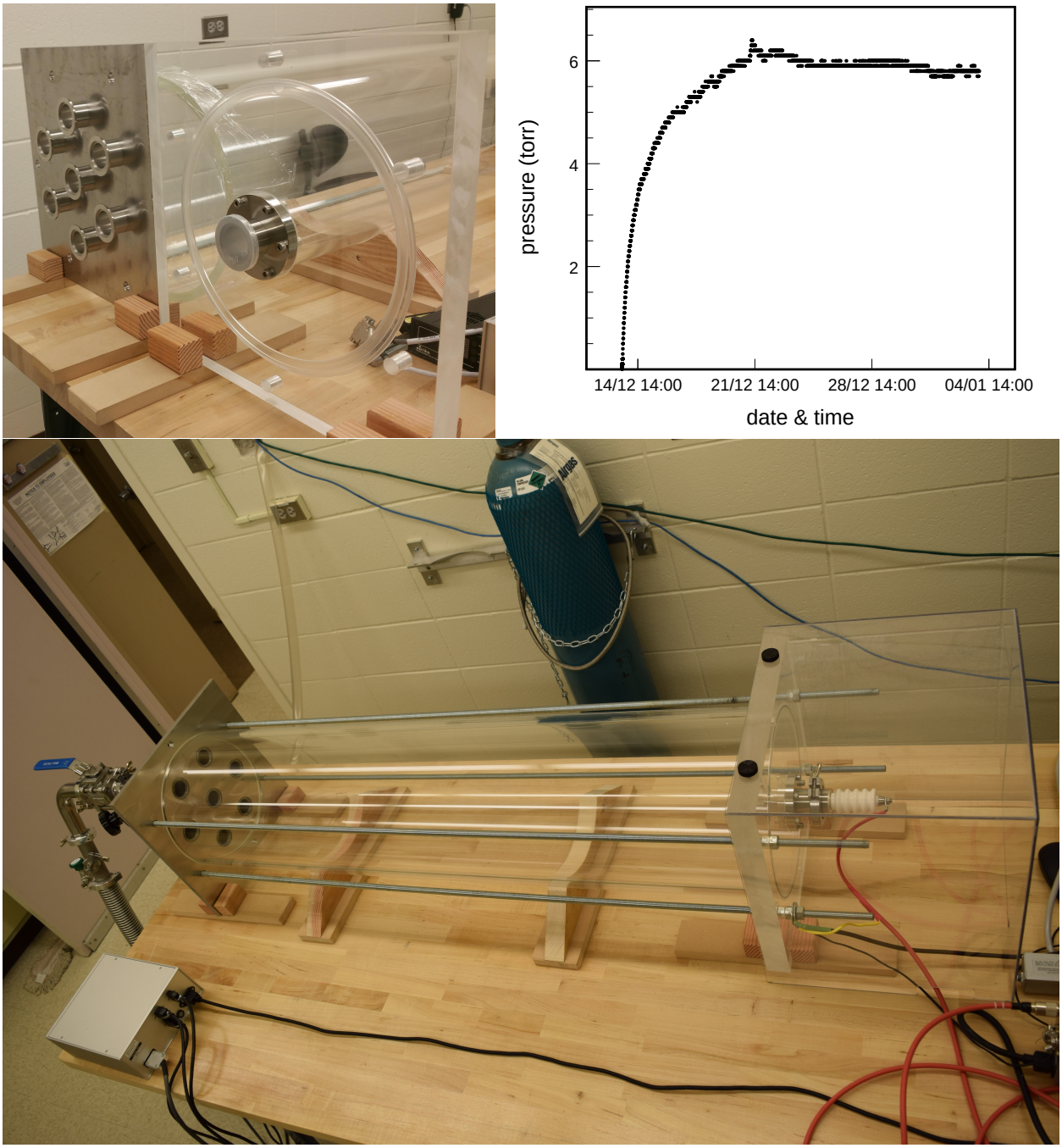

Figure 3.10: D^3 - Milli stage 3 acrylic vacuum vessel and endplates. The vessel was procured and the endplates were designed and manufactured in our machine shop. Top right: Outgassing curve for the empty acrylic vessel. It is much worse than for the steel vessel which could be problematic when operating at low pressures.

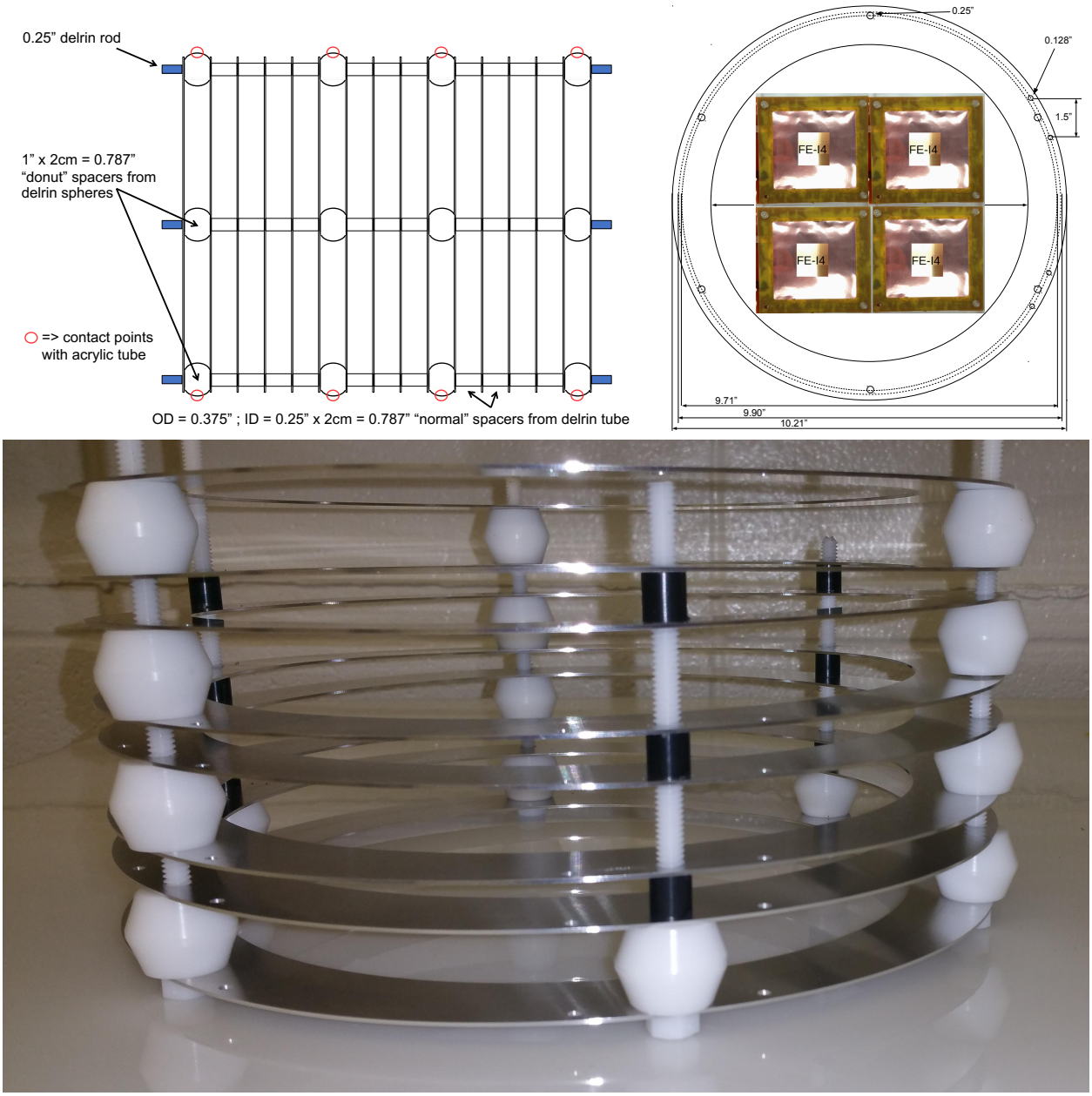

Figure 3.11: D^3 - Milli stage 3 field cage concept. Bottom: Test assembly showing the "donut" spacers protruding beyond the ring diameter. Top left: The red circles indicate the contact points with the acrylic vessel. Top right: Concept for a modular design. Four GEM/pixel chip assemblies arranged in a square inside the ID of a field cage ring, so the four setups would readout using the same drift field.

CHAPTER 4
AVALANCHE GAIN AND GAIN RESOLUTION MEASUREMENTS

4.1 Motivation

The energy resolution of a detector is one the fundamental parameters which describe how effective the detector will be. In any phase space involving energy, the energy resolution will determine how well a detector can discriminate between different event types, including proper identification of a desired signal. Even in phase spaces that do not explicitly contain event energy, an angular distribution for instance, the energy is usually involved via some sort of weighting. And, again, the energy resolution will inform how confident one is in the energy measurement. We seek as much information as possible about the energy resolution and, generally, strive to make as good as possible.

If detector and electronic noise can be suppressed, then the gain resolution can be thought of as the fundamental limit of the energy resolution. One way to suppress the detector and electronic noise is to measure the gain resolution at infinite gain, and this can be done by extrapolation, see Eq. 4.2. One of the main topics of this chapter is measuring this extrapolated gain resolution for different GEM-based gain stages, and gases, and trying to form a cohesive picture.

The other main topic is the gain itself. The gain for different gain stages and gases is measured and put into context with a heuristic model describing a fairly large parameter space in which avalanche multiplication is possible. This model draws on the discussion from Sec. 2.4.3 and the idea of the reduced field, E/p, where E is the electric field and p is the gas pressure. When all of this is put together a single equation, Eq. 4.5, is the result and it contains all the parameters necessary to describe any GEM-based detector operating at any pressure.

4.2 Experimental method and system calibration

4.2.1 Experimental setup

The copper, or aluminum, readout plate was connected, with a short BNC cable, to an Endicott eV-5093, or a Cremat CR-110, charge sensitive preamplifier with a quoted, and measured, gain of 3.6 V/pC, or 1.4 V/pC, respectively. This preamp is housed inside an eV-550 module which greatly reduces Rf-noise and includes a mounting board for the preamp which also provides AC-coupling for the detector. After the preamp, the signal is shaped by a Canberra AFT 2025 spectroscopy amplifier and finally an Ortec EASY-MCA operates as a Pulse Height Analyzer (PHA), see Fig. 4.1.

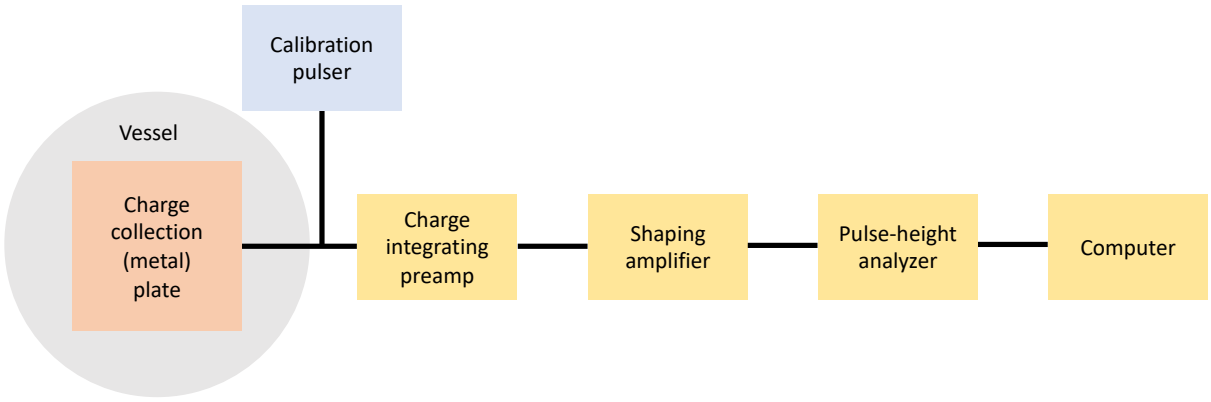

Figure 4.1: Signal detection and electronics cartoon depicting the gain measurement setup. The calibration pulser sends voltage pulses into a 1 pF capacitor located on the circuit board containing the preamplifier. The resulting voltage pulses are then measured either at the shaping amplifier output with an oscilloscope, or directly with the pulse-height analyzer. See text for more discussion.

4.2.2 Calibration and systematics

The detector is calibrated by injecting voltages pulses into a 1 pF test capacitor located on the eV-5093 and measuring either the output of the shaping amplifier, or the resulting signal on the PHA itself. The ratio of these two pulses is taken as the system response.

Initially, an additional high-pass filter was installed immediately after the detector output. After some time, during the D^3 - Milli stage 1 measurements, it was discovered that this was not needed and it was removed. This is mentioned because it changes the detector calibration, or system response measurement, because of the additional capacitance of the filter. Without the additional filter the response value is 2.86 PHA bins/fC and this was measured directly with the PHA to reduce any effect by the oscilloscope or the PHA itself.

The system response with the additional filter is 0.91 ± 0.13 V/pC, and was measured at the shaping amp output where the large error is due to the mis-measurement of the small capacitance in the filter. This results in a 14% error in the gain values for all of the D^3 - Micro and the D^3 - Milli stage 1 triple GEM measurements.

The operating range of the PHA is stated to be 0 - 10 V with 8192 channels and the linearity was checked. There is also a 2% error of all the voltage values due to multimeter accuracy. Every

voltage divider was measured with a HV probe and multimeter at each GEM lead and the values were corrected for due to the high resistance values of the circuits.

For pressure measurements at, or near, 1 atmosphere there is a systematic error of 0.5%, and for the low pressure measurements with SF_6 this was increased to 5% due to gas flow being required. As the noise varied drastically between the setups, the shaping time was varied between 1 and 12 μs based on which setting was most efficient at noise suppression. All settings, however, result in the same pulse height.

4.2.3 The gain and gain resolution measurements

A note on the gain measurement process

Generally, the vessel was evacuated overnight, or for several days where to pressure would reach $\approx 10^{-5}$ torr, before measurements were taken. However, sometimes a "pump and purge" method was used where the vessel is briefly brought to vacuum, $\approx 10^{-3}$ torr, filled with the target gas, and repeated a couple of times. Both methods perform adequately, and the most important factor in gain stability seems to be the amount of time the detector sits sealed to the atmosphere after being exposed to it. This is likely due to component outgassing and after a couple of weeks this is essentially a non-effect, whether being held at vacuum or not. In larger detectors, with much higher component masses, there will likely need to be a month long period of gain stabilization, and outgassing, before any dark matter data runs can be performed.

When possible a source "off" background spectrum was taken and subtracted from every source "on" spectrum, but generally this was only necessary in the low gain studies with THGEMs. The gain stability was also monitored and accounted for, when necessary, by taking before and after measurements and averaging the results, and these details will be provided. The spectra were generally recorded for five minutes a piece but longer if the count rate dictated, for instance the ^{210}Po spectra are 30 minutes each.

Definition of the gain and gain resolution

The gain and gain resolution are always measured the same way; a χ^2-minimization is preformed for every pulse-height spectrum, background subtracted or not, and the mean of the fit is taken to be the gain. We take the standard deviation divided by the mean (of the fit) as the fractional gain resolution.

Gain and gain resolution curves

The avalanching process is generally exponential, see Sec. 2.4.3, and is empirically well described by:

$$G = 10^{(V_{GEM} - V_1)/V_2} \tag{4.1}$$

where V_1 and V_2 are parameters extracted from a χ^2-minimization and V_{GEM} is the total voltage applied across all GEMs. G here is the gain, and is an effective gain value which contains any reabsorption, or any other inefficiencies in the avalanching process. Since the gain itself is used in multiple places throughout this chapter, we note here that G is sometimes referred to as the initial gain value. V_1 and V_2 will be displayed in tables for the various data sets so we describe them here for clarity. V_1 is the voltage at which a given setup would obtain a gain of unity. V_2 is the voltage required, by a given setup, to obtain a gain increase a factor of 10.

The fractional gain resolution is empirically well described by:

$$\sigma_G/G = \sqrt{(a/G)^2 + (b')^2} \tag{4.2}$$

where a and $b' = b/100\%$ are, again, extracted from a χ^2-minimization to the data. Throughout this chapter, we display σ_G/G and the parameter b as a percentage, and these are usually referred to as the gain resolution and the asymptotic gain resolution, respectively. We, again, describe a and b' here for clarity. The parameter b' is the asymptotic (infinite gain) fractional gain resolution value. This is the gain resolution value we can expect a given GEM-based detector to achieve if all electronic/detector noise is suppressed. This is discussed throughout this chapter and explicitly starting in Sec. 4.3.4. The parameter a is the gain at which the gain resolution obtains its asymptotic value.

As a bit of foreshadowing, the $HeCO_2$ discussion will close with a measurement of the Fano factor, which is the variance in the number of primary ion-pairs formed in a given interaction. This will be done using the fit parameters just mentioned from six different GEM-based prototype data sets. We will also utilize these equations throughout this chapter, and refer to the resulting fits as the gain and gain resolution curves, respectively.

4.3 $HeCO_2$ gas: Gain stage comparison

$HeCO_2$, with a ratio of 70:30, was the most studied gas by our group and was used with many different setups. This section will discuss the gain and gain resolution measurements using the ^{55}Fe source with different GEM setups and different pressures.

4.3.1 Thin GEMs

Helium has a W-factor of $\approx 41\,\text{eV}$ [98] which results in 172 electrons per 5.9 keV photon in $HeCO_2$. As opposed to Argon, discussed in section Sec. 4.4, Helium only has one orbital shell filled with electrons. As a result, spectra taken in $HeCO_2$ with thin GEMs commonly look like those in Fig.

4.2. A crystal-ball function [84] was used to model the spectra while no additional model for the background was used.

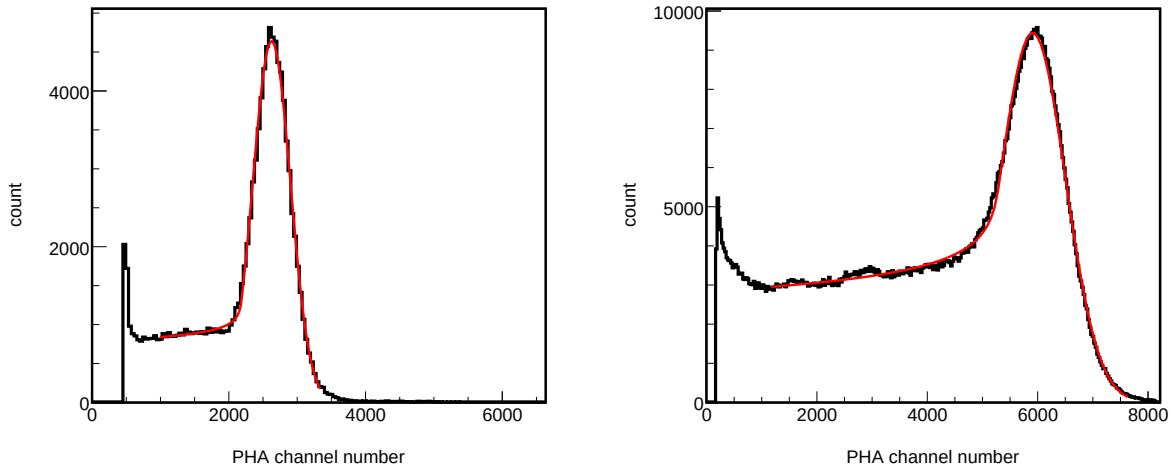

Figure 4.2: Typical high gain pulse-height spectra of ^{55}Fe in $HeCO_2$. Left: Double thin GEMs; Right: Triple thin GEMs. The ratio of the gas is 70:30 and measurements were done at atmospheric pressure.

Gain stability

D^3 - Milli stage 1 suffered from a higher outgassing rate than the other setups due to the amount of material involved which lead to a gain decay over time, see the top plots Fig. 4.3. The triple thin GEMs data set was taken after being held at vacuum, $\approx 10^{-3}$ torr, for three days, filled to 1.0 atm., and then closed off. The gain decayed by roughly 10% per day and was corrected for by flowing gas when necessary. The cusps in the top plots in Fig. 4.3 are when the gas flow was turned on. The gap in data near the end of the run is when the triple GEM gain study was conducted, and the results from this study are the plots on the right of Figs. 4.4 and 4.5. These were chosen to illustrate the worst gain variation that occurred during any study with electron gases.

As shown in the bottom plots in Fig. 4.3, stage 2 was much more stable owing to less material being used, and this represents more typical behavior of the prototypes. The gap in data here indicates the time in which the double thin GEM gain study in the plots on the left of Figs. 4.4 and 4.5 was taken.

The stability data was used in the gain and resolution curves as follows: 1) V_{GEM} was the same value as one of the points in the gain study. 2) Spectra for roughly the same duration as the gain study were fit and the mean and sigma averaged. 3) These average values were used for the gain and resolution values for that V_{GEM}. 4) The largest difference in those mean and sigma values were then divided by the number of spectra measured to get a variation between individually

measurements. These were taken as statistical errors and added in quadrature with the fit errors for all other V_{GEM} values. This procedure was followed for all available stability data and results in the error bars in the gain and gain resolution values throughout this thesis. Some of the gain data did not have associated stability data, and this is mentioned when it is relevant.

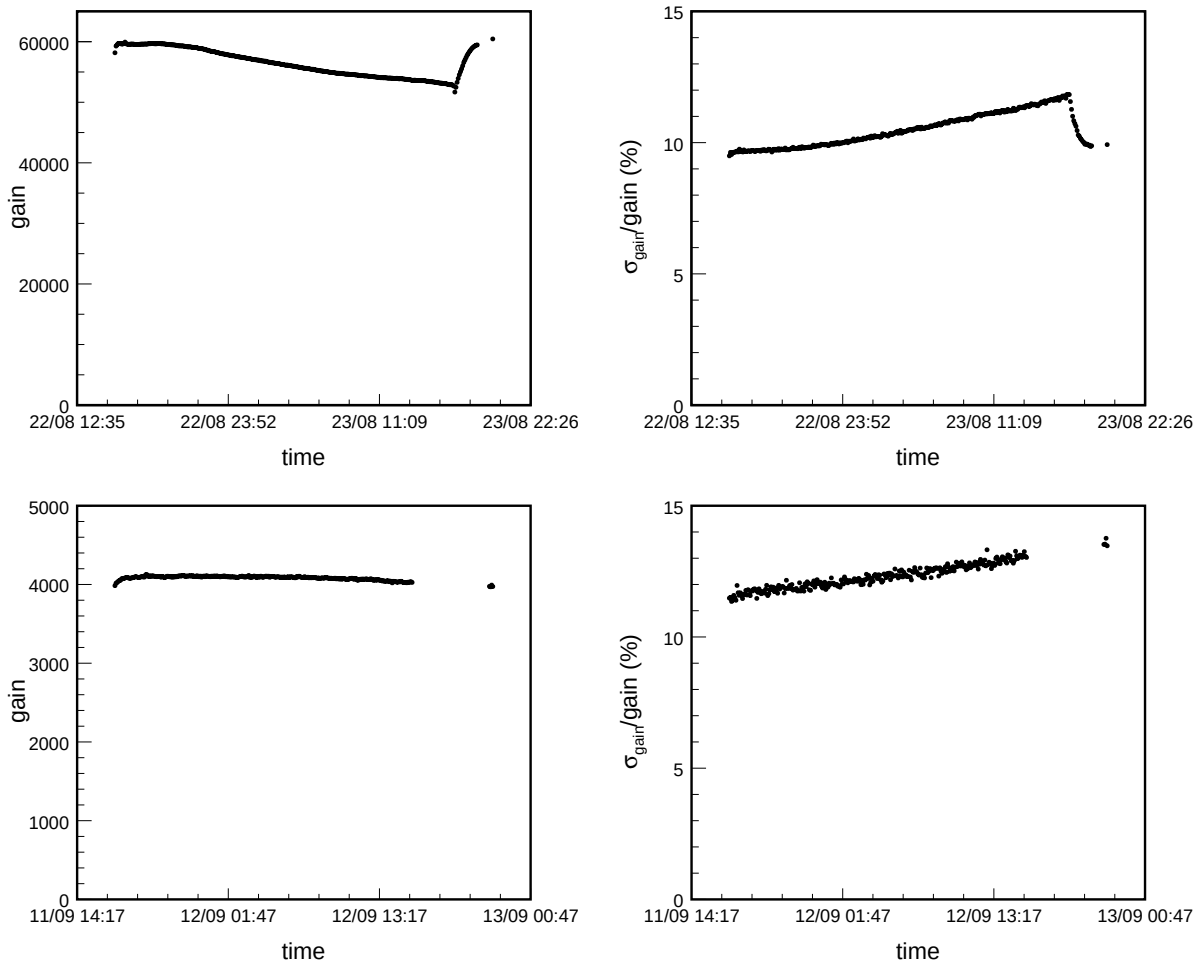

Figure 4.3: Top: Stability curves for the D^3 - Milli stage 1 triple GEM setup Bottom: D^3 - Milli stage 2 double GEM setup. Left: gain stability. Right: resolution stability, see text for discussion. Error bars have been suppressed for clarity.

Gain and gain resolution

Fig. 4.4 shows the three thin GEM setups gain plotted against V_{GEM}. The plots on the left are comparing the two double GEM setups compared and shows a substantial difference. This is likely due to the calibration and operating conditions being quite different. The gray points are from D^3 - Micro and, in addition to having an additional capacitive filter attached to the output, was

operated stably for many weeks at a time without the vacuum vessel being opened. In contrast, the black points are from D^3 - Milli2 and were measured soon after the vessel had been held at vacuum, and the amount of time being held at vacuum was less than with D^3 - Micro.

However, if this were simply a gas purity issue one would expect the data taken after less time being held at vacuum to have lower gain at a given V_{GEM}, and the opposite is seen here. Another difference is that the D^3 - Milli2 GEMs were brand new and this was the first data taken with them, whereas, D^3 - Micro used the same GEMs for months of data taking. However, GEM performance over time and in harsh radiation environments has been extensively studied [14], so we consider the gain resolution for more information.

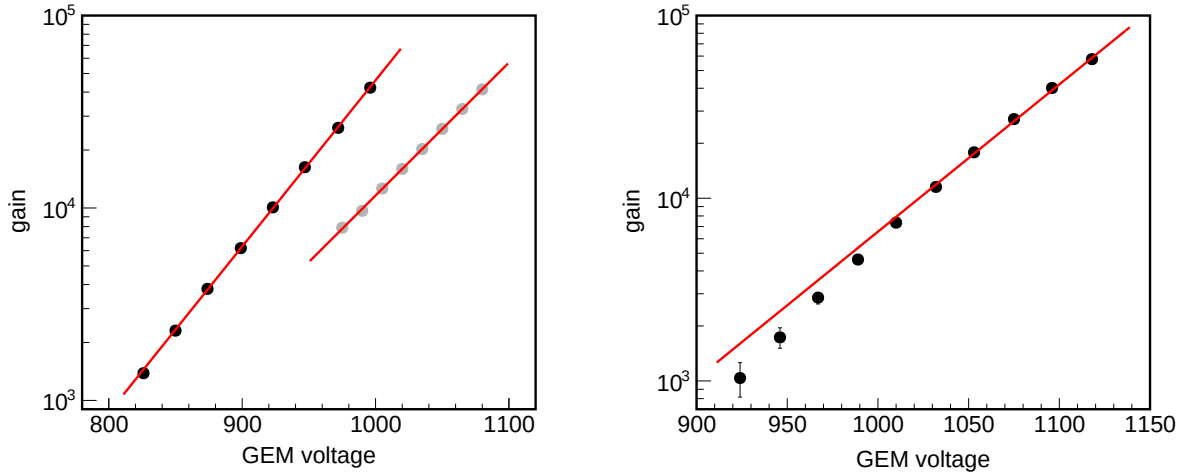

Figure 4.4: Gain vs. V_{GEM} curves. Left: Double thin GEMs. Black points: D^3 - Micro; Gray points: D^3 - Milli stage 2; Right: Triple thin GEMs: D^3 - Milli stage 1. The large error bars are due to the gain fluctuating during the measurements, see text for discussion.

The plot on the left of Fig. 4.5 shows that the setup requiring more voltage to achieve the same gain actually has a better asymptotic resolution, but needs higher gain to achieve it. The likely explanation for all of this is the following: The avalanche distribution changes as the reduced field does and, if the gain is similar, the variance decreases as the field reduced increases. Regardless of the reason more voltage is needed for a given gain, this means that D^3 - Micro was operating at a higher reduced field and a lower avalanche variance should be expected, and this would lead to a lower overall variance which is seen.

The plots on the right of Figs. 4.4 and 4.5 show the gain and resolution curves for the triple thin GEM setup. The gain was changing more during this measurement as seen in and the error bars are due to trying to account for this. For a given V_{GEM} less gain is achieved with triple GEMs than double but the dynamic range is extended when using triple GEMs, or more GEMs in general. Since V_{GEM} is being divided by three instead of two the reduced field is lower per GEM and thus less gain should be expected. A similar asymptotic gain resolution is also seen with the triple GEMs

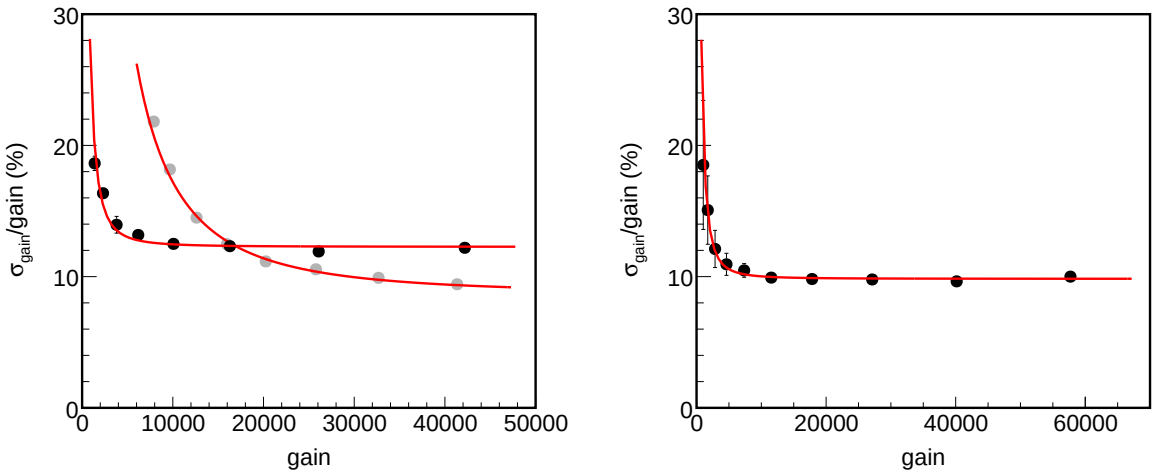

Figure 4.5: Gain resolution vs. gain curves. Left: Double GEMs. Black points: D^3 - Micro; Gray points: D^3 - Milli stage 2. Right: Triple GEMs.

and, if this were only a function of the reduced field, it would be higher.

However, the gain per GEM is much lower as well and, as discussed in Sec. 4.3.5, the avalanche variance is a function of the reduced field, gain, and the ionization potential of the gas. As a result of this complicated relationship, the avalanche variance is approaching a minimum in the range of reduced field being considered here. Since the avalanche variance, along with the fluctuation in the number of primary electron-ion pairs, is what determines the asymptotic gain resolution we can expect similar values for it if the avalanche variance is similar. This is observed in the double and triple thin GEM setups.

4.3.2 Thick GEMs (THGEMs)

In principle, a THGEM could have a similar reduced field to a thin GEM but in reality sparking prevents this, and this starts to occur at approximately one third of the maximum reduced field that a thin GEM can operate. As a result, the maximum gain achieved with a single THGEM was $\approx 10^3$. This seems to have an effect on the single THGEM spectra in Fig. 4.6, as the peak is not Gaussian, and has been fit as a Landau distribution. With higher gain in the double THGEM setup, a Gaussian distribution is recorded.

Gain vs. pressure

During this study the gain in $HeCO_2$ was measured at different pressure with the D^3 - Milli stage 1 single THGEM setup. The gain stability at 0.5 atm. was monitored and gain data was taken. The pressure was then increased to 0.75 atm. where another gain measurement was taken. The chamber was then pumped overnight, refilled the next day, and the stability monitored again at

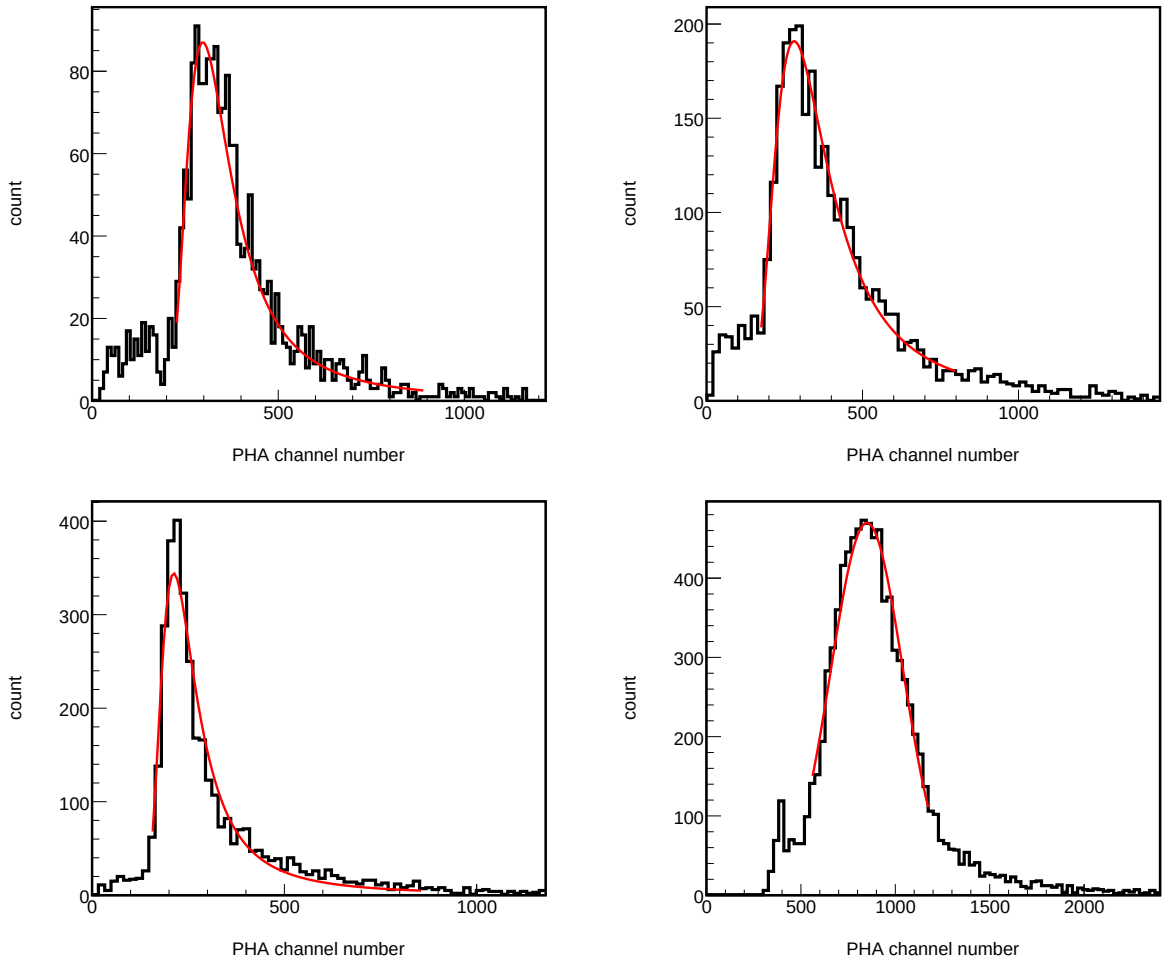

Figure 4.6: THGEM pulse-height spectra. Top left: Single THGEM at 0.5 atm. Top right: Single THGEM at 0.75 atm. Bottom left: Single THGEM at 1.0 atm. Bottom right: Double THGEM at 1.0 atm. All single THGEM $HeCO_2$ spectra were non-Gaussian and fit as a Landau distribution.

1.0 atm. until the final gain mesurement at 1.0 atm. was taken. These curves are shown in the plot on the left of Fig. 4.7. From left to right is: 0.5, 0.75, and 1.0 atm. Unfortunately, the gain at 0.75 atm. was not stable and stability data was not recorded. This can be seen in the slope and the resulting resolution data, the top right plot in Fig. 4.8, was roughly a factor 2 worse that at 0.5 atm. and 1.0 atm, which is not consistent with expected behavior. This likely had to do with the abrupt temperature change that occurs when filling from a lower pressure and not letting the detector stabilize before taking data.

Until now all of the measurements have been taken at a single pressure, but now it needs to be introduced as a variable. Replacing N with p in Eq. 2.36 where p is the gas pressure, and writing $E = \frac{V_{GEM}}{t}$, where t is the GEM thickness gives:

$$\frac{\alpha}{p} = Aexp\left(-B\frac{npt}{V_{GEM}} \right) \tag{4.3}$$

where n is the number of GEMs which V_{GEM} is distributed over. Eq. 4.3 allows us to develop an understanding the gain dependence on gas pressure. We can calculate the V_{GEM} value needed to achieve the same gain at half the pressure. Assuming the constants A and B do not change, V_{GEM} should decrease by a factor of $2\ln(2)$, or $\approx 38\%$. This is consistent with the values in the left plot in Fig. 4.7 when comparing the 0.5 atm. and 1.0 atm. curves.

As seen in the right plot of Fig. 4.7, a large amount of voltage was needed to operate two THGEMs and, as a result, high rates of sparking occurred when raising the drift field which could have had an effect on the resolution. Although higher gain was achieved with double THGEMs than with a single THGEM, further operation will require proper insulation by either coated the vessel with Parylene, or a similar insulating material, or placement in a non-metallic vessel. This setup was unable to achieve stable gain with SF_6, partly, because of this.

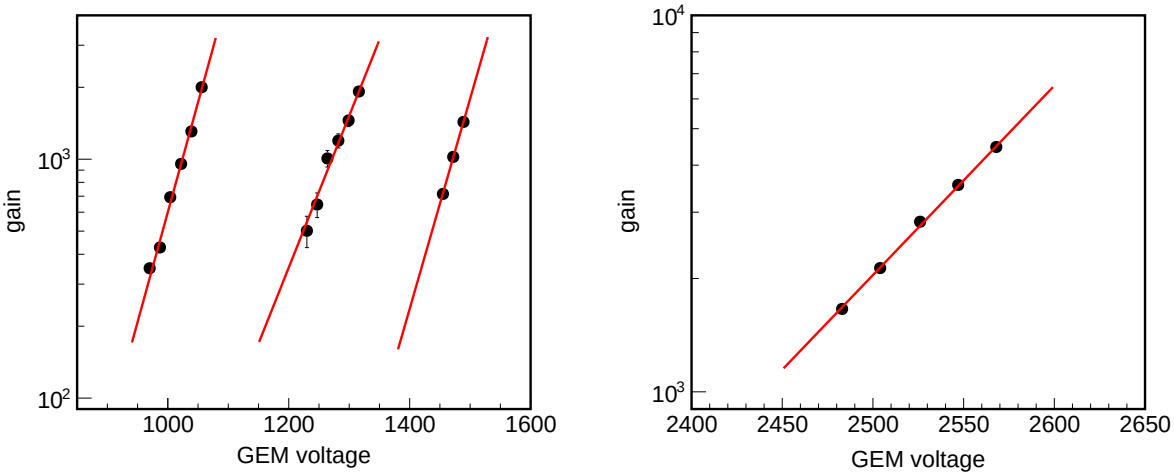

Figure 4.7: THGEM gain curves. Left: Single THGEM at, from left to right, 0.5, 0.75, and 1.0 atmosphere. Right: Double THGEM AT 1.0 atmosphere. The 0.75 atmosphere measurement, middle curve in the left plot, suffered from large gain instability, and lower overall gain than is consistent with expectations.

Gain resolution

In general, the THGEM resolution is worse than that of the thin GEMs as a partial result of the lower reduced field. As mentioned, the avalanche variance has a dependance on the reduced field and the gain itself. In the reduced field regime of THGEM operation this dependance is much stronger than with thin GEMs, more exponential vs. near its minimum. As a result, with the lower reduced field in the double THGEMs a much larger asymptotic resolution is seen then between the

triple and double thin GEMs, and a triple THGEM setup would see an even larger increase. The details of this are discussed in the Sec. 4.3.5 and, specifically, see Fig. 4.12.

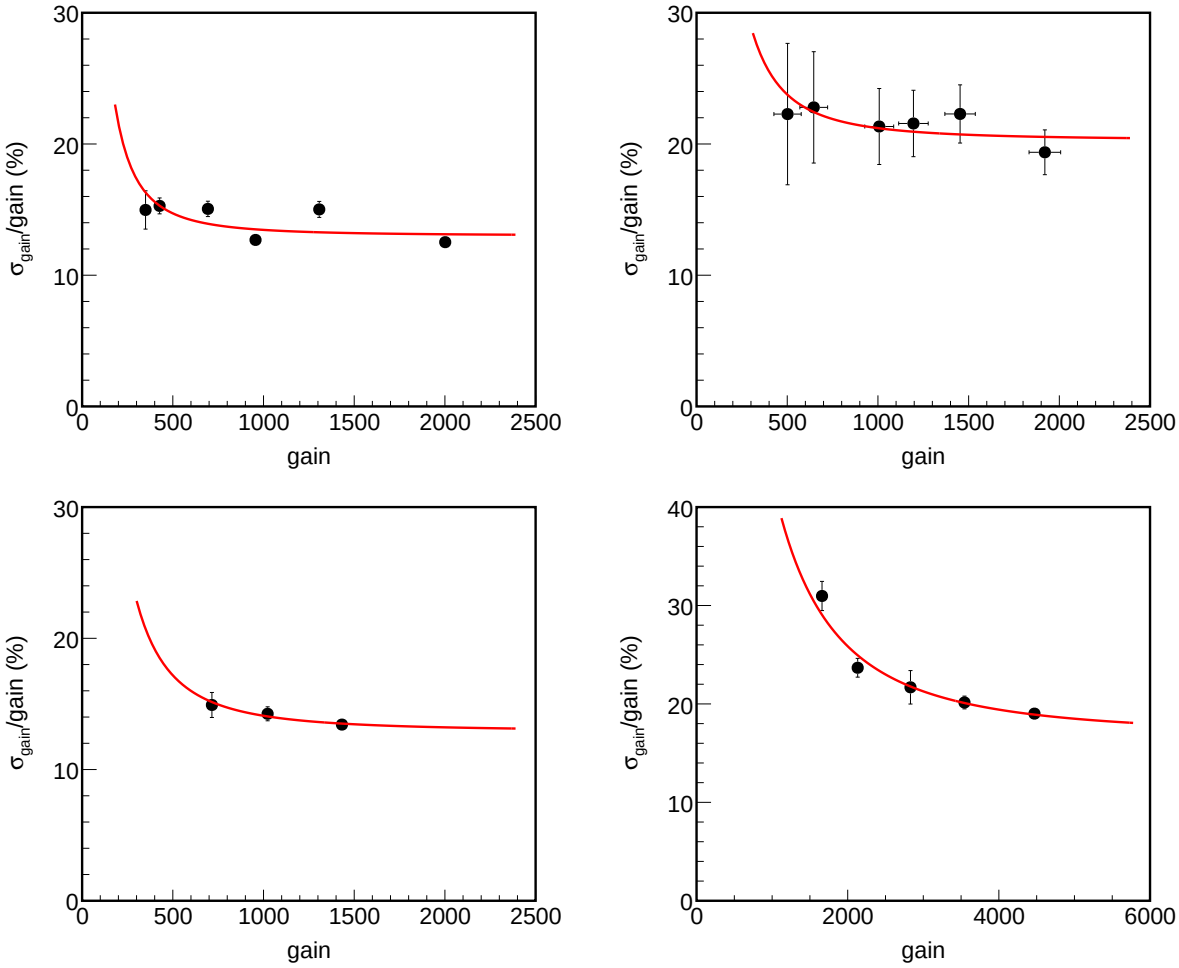

Figure 4.8: THGEM gain resolution curves. Top left: Single THGEM at 0.5 atmosphere. Top right: Single THGEM at 0.75 atmosphere. Bottom left: Single THGEM at 1.0 atmosphere. Bottom right: Double THGEM at 1 atmosphere.

4.3.3 First Townsend coefficient

As discussed in Sec. 2.4.3, the avalanching process is possible over a broad range of reduced field values. Until this point we have discussed each prototype uniquely but they all operate via the same process, and Eq. 4.3 allows a generalized interpretation of the gain data. If we apply Eq. 2.30 to any GEM with thickness, t, and where E is constant, we can write:

$$\ln(G) = n\alpha t \tag{4.4}$$

Table 4.1: Fit parameters characterizing the effective gain and resolution for 5.9 keV photons from ^{55}Fe in $HeCO_2$ (70:30), defined by Eqs. 4.1 and 4.2.

Data set	V_1	V_2	a	b (%)
Double thin GEMs (D^3 - Micro)	412 ± 9	145 ± 3	$(1.49 \pm 0.01) \times 10^5$	8.64 ± 0.04
Double thin GEMs (D^3 - Milli2)	460 ± 10	116 ± 2	$(2.17 \pm 0.08) \times 10^4$	12.27 ± 0.09
Triple thin GEMs	526 ± 27	124 ± 4	$(1.9 \pm 0.4) \times 10^4$	9.83 ± 0.05
THGEM - 1.0 atm	1130 ± 27	114 ± 5	$(6 \pm 2) \times 10^3$	12.9 ± 0.7
THGEM - 0.75 atm	799 ± 41	157 ± 12	$(6 \pm 5) \times 10^3$	20 ± 2
THGEM - 0.5 atm	698 ± 14	109 ± 2	$(3.4 \pm 0.5) \times 10^3$	13.0 ± 0.3
Double THGEMs	1842 ± 48	199 ± 2	$(3.9 \pm 0.2) \times 10^4$	16.7 ± 0.7

We can now combine Eq. 4.3 and Eq. 4.4 to obtain:

$$\frac{\ln(G)}{npt} = A\exp\left(-B\frac{npt}{V_{GEM}}\right) \tag{4.5}$$

Eq. 4.5 now has all of the necessary parameters to compare any GEM based detector, at any pressure, as long as Eq. 4.3 remains valid. It should be noted that Eq. 4.5 will only be valid when a multiple GEM detector has V_{GEM} divided evenly amongst the GEMs. The D^3 - Micro prototype had a voltage difference between the two GEMs of slightly greater than 1% , while all the others had difference of less than 1%, see Tables. A.4 and A.5 for all values. From here then, the gain and reduced field will be replaced with gain* and reduced field* to indicate that they are per GEM.

The plots in Fig. 4.9 shows all seven data sets, previously discussed and listed in Table **??**, taken with $HeCO_2$. The left side of Eq. 4.3 is on the y-axis and the reduced field* is on the x-axis. Each grouping of points is from one data set and from left to right, in order of increasing field strength, we have: 1) double THGEMs, 2) THGEM at 1.0 atm, 3) THGEM at 0.75 atm, 4) THGEM at 0.5 atm, 5) triple thin GEMs, 6) double thin GEMs, (D^3 - Milli stage 2), 7) double thin GEMs (D^3 - Micro). All pressures are 1.0 atm. unless indicated otherwise.

The red lines are χ^2-minimizations with Eq. 4.5 and, as can be seen in the plot on the left, describes the general trend of the data but preforms poorly for each individual set. The plot on the right shows each data set with an individual fit which preforms better. It should be noted that Eq. 4.1 would be a straight line on this plot so over a broad reduced field range it becomes invalid. Systematic differences can also be seen between the data sets, for instance, the rapidly changing gain with the triple thin GEM setup is evident as the lower reduced field points have larger errors and fall below the fit line. But regardless of these differences, different values for A and B would be obtained for the different data sets. However, as mentioned in Sec. 2.4.3, the quantity B/A is a measurement of the effective ionization potential of the gas and should be constant for a given gas. So there are some discrepancies between the model used and what is seen in the data. We mention

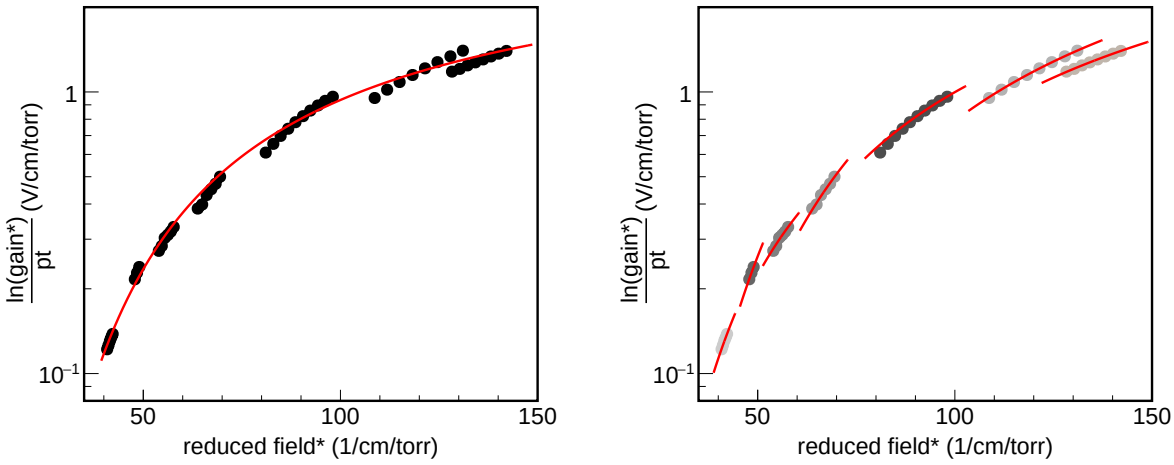

Figure 4.9: All seven $HeCO_2$ data sets discussed, listed in Table A.3, plotted together. Each grouping of points is a single gain data set. From left to right: 1) double THGEMs, 2) THGEM at 1.0 atm, 3) THGEM at 0.75 atm, 4) THGEM at 0.5 atm, 5) triple thin GEMs, 6) double thin GEMs, (D^3 - Milli stage 2), 7) double thin GEMs (D^3 - Micro). The red lines are fits of Eq. 4.3, see text for discussion.

the obvious ones briefly.

Recall that α is the number of electrons produced in the avalanche per unit length and there are implicit assumptions in Eq. 4.5 about that number that are not necessarily true. First, not all of the electrons start with small energies and then are accelerated above the ionization potential. Many already have large energies and this makes α appear to be smaller. Secondly, simply because an electron has an energy greater than the ionization potential doesn't mean the probability that it will ionize a target atom is equal to unity, and this makes α appear larger. There are also many inelastic collisions that occur that do not produce secondary ionizations [48] and because of all these effects a closed form solution covering the entire proportional regime does not exist and Monte Carlo techniques become necessary [1].

However, reasonable results are obtained via the plot on the right of Fig. 4.9, and all B/A values are listed in Table 4.2. A can be regarded as a saturation value that α reaches as E/p increases, and B is proportional to the effective ionization potential. A W-factor of 34.4 eV was used to get the initial gain values for comparison.

4.3.4 Ultimate gain resolution

If detector effects, i.e. detector and electronic noise, can be suppressed then the ultimate gain resolution of a detector will depend on two terms: 1) The primary ionization variance and 2) The secondary ionization, avalanche, variance. This can be expressed as [50] [13]:

Table 4.2: Effective ionization potential measurements with $HeCO_2$. A and B are extracted from a χ^2 - minimization of Eq. 4.3.

Data set	B/A
Double thin GEMs (D^3 - Micro)	32.9 ± 0.7
Double thin GEMs (D^3 - Milli2)	27.2 ± 0.5
Triple thin GEMs	29.3 ± 0.6
THGEM - 1.0 atm	12.5 ± 0.3
THGEM - 0.75 atm	34.7 ± 0.7
THGEM - 0.5 atm	20.2 ± 0.4
Double THGEMs	29.6 ± 0.6
Combined	37.0 ± 0.7

$$(\frac{\sigma_G}{G})^2 = (\frac{\sigma_{n_0}}{n_o})^2 + (\frac{\sigma_M}{M})^2 \tag{4.6}$$

where n_0 is the number of primary electrons. M is the mean multiplication factor for all the avalanches in a given pulse. If we assume that each avalanche is statistically independent, which is the true for most of the proportional region, we can express M in terms of a single-electron avalanche factor A we can write this as:

$$(\frac{\sigma_G}{G})^2 = (\frac{\sigma_{n_0}}{n_o})^2 + \frac{1}{n_0}(\frac{\sigma_A}{\overline{A}})^2 \tag{4.7}$$

where $\overline{A}$ is the average multiplication of a single electron. Two factors can then be introduced that represent the variance of both the primary and avalanche fluctuations. This is usually done as:

$$(\frac{\sigma_G}{G})^2 = \frac{F+f}{n_0} \tag{4.8}$$

where F is called the Fano factor and we can denote f as the avalanche variance. Since the primary number of electrons will depend on the incident particle energy we can introduce the W-factor:

$$(\frac{\sigma_G}{G})^2 = W\frac{(F+f)}{E} \tag{4.9}$$

where $W = \frac{E}{n_0}$ and is the average amount of energy required to create an electron-ion pair and is energy dependent, but constant above a few keV [35]. It is the average amount energy required to produce an electron-ion pair, but the name W-factor is generally used, and typical values are $\approx$ 30 eV for gases.

F and f are the fundamental parameters governing the ultimate resolution achievable in ion-

ization avalanching detectors. Both are gas dependent and range from 0 to 1 but F is typically much closer to 0. The Fano factor describes how much of the incident particles energy went into ionization and has a slight dependance on the type of incident particle [35]. The avalanche variance, f, describes the distribution of electrons produced in many avalanches and, as we will see in Sec. 4.3.5, has a complicated dependance on the avalanching field.

Taking this one step further, using the $HeCO_2$ data sets discussed previously we can extrapolate Eq. 4.9 to an infinite gain form. The asymptotic resolutions values, the b parameters from Eq. 4.2 in Table 4.1, can be regard as the resolution values at infinite gain which we will denote as $\frac{\sigma_G}{G}_\infty$. We can also assume that f has some dependance on the gain, so we will denote f_0 as the avalanche variance at infinite gain. Now:

$$(\frac{\sigma_G}{G}_\infty)^2 = W\frac{(F+f_0)}{E} \tag{4.10}$$

In Fig. 4.10 the asymptotic resolution values are plotted against the reduced field. There is no theoretical justification for the Fano factor to have a gain dependance so we are left to conclude that f_0 decreases as the reduced field increases. Note that this does not mean in, for instance, a proportional counter where $E \sim 1/r$ that the same dependence would be seen. In fact, in a continuously varying field where the avalanche starts at very low field values, the variance is observed to increase and then plateau as the avalanche continues into the stronger field [13]. In this case, as the avalanche is "turning on" there are many more elastic collisions that don't result in secondary ionizations. This proportion continues to increase, with the field, until the probability that a given collision will result in an ionization is near unity. In a uniform avalanching field this "turn on" effect would essentially be a step function and so the plateau is all that would be measured. What this shows is that the plateau of the avalanche variance is lower for higher reduced fields and this is to be expected in a certain range of reduced field. We discuss some details of the avalanche distribution next.

4.3.5 Modeling the avalanche distribution

Several models have been proposed to describe the distribution of electron avalanches and the modern technique is using tools such as Garfield [1] and Magboltz [32]. Most of these models define different classes of electrons and proceed to calculate the probability distribution of the distances traveled for specific occurrences, i.e. an electron causing a secondary ionization. In the case of Bryne [36] and Legler [69], two classes are described: s-electrons are produced from a secondary ionizing collision but lack the energy to create more secondaries and f-electrons are in equilibrium with the E-field and may, or may not, create secondary ionizations.

Using these two classes of electrons Alkhazov [13] defines the probability distributions of the distances traveled by a s-electron transforming into a f-electron and visa versa. From here two specific cases are considered which will determine how the avalanche progresses: 1) A f-electron has

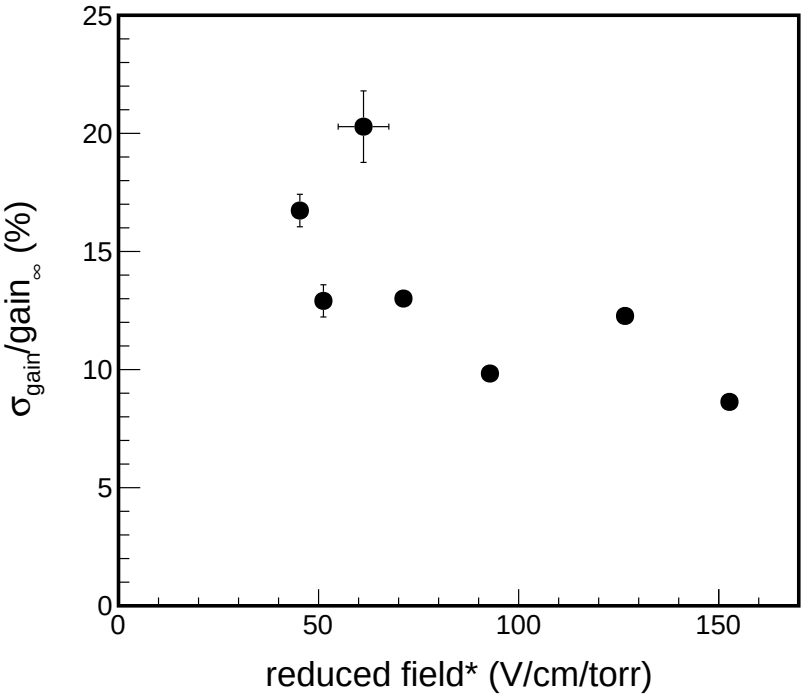

Figure 4.10: Asymptotic gain resolution values for the seven $HeCO_2$ data sets, listed in Table A.3, vs. reduced field*, see text for discussion.

an ionizing collision resulting in two s-electrons or 2) A f-electron has an ionizing collision resulting in one s-electron and one f-electron. Two probability distributions can then be defined describing the number of electrons the avalanche contains at a point x if it were developed from either a s-electron or f-electron and the variance can be calculated.

Legler assumed that the electron that starts the avalanche, the seed electron, must travel a minimum distance, $x_0 = \frac{U_0}{E}$, before it can produce a secondary ionization, where E is the electric field and U_0 is a model parameter. Thus x_0 can be described as the minimum distance the seed electron must travel in order to gain enough energy from the electric field to overcome the effective ionization potential, U_0.

Since α is number of electrons produced per unit path length along the avalanche, we can introduce another quantity χ where:

$$\chi = \alpha x_0 = \alpha \frac{U_0}{E} \tag{4.11}$$

χ encapsulates the reduced field, gain, and ionization potential and it has a unique dependence on the reduced field for different gases, see the plots on the left of Fig. 4.12.

In the case of Legler's model it can be shown [13]:

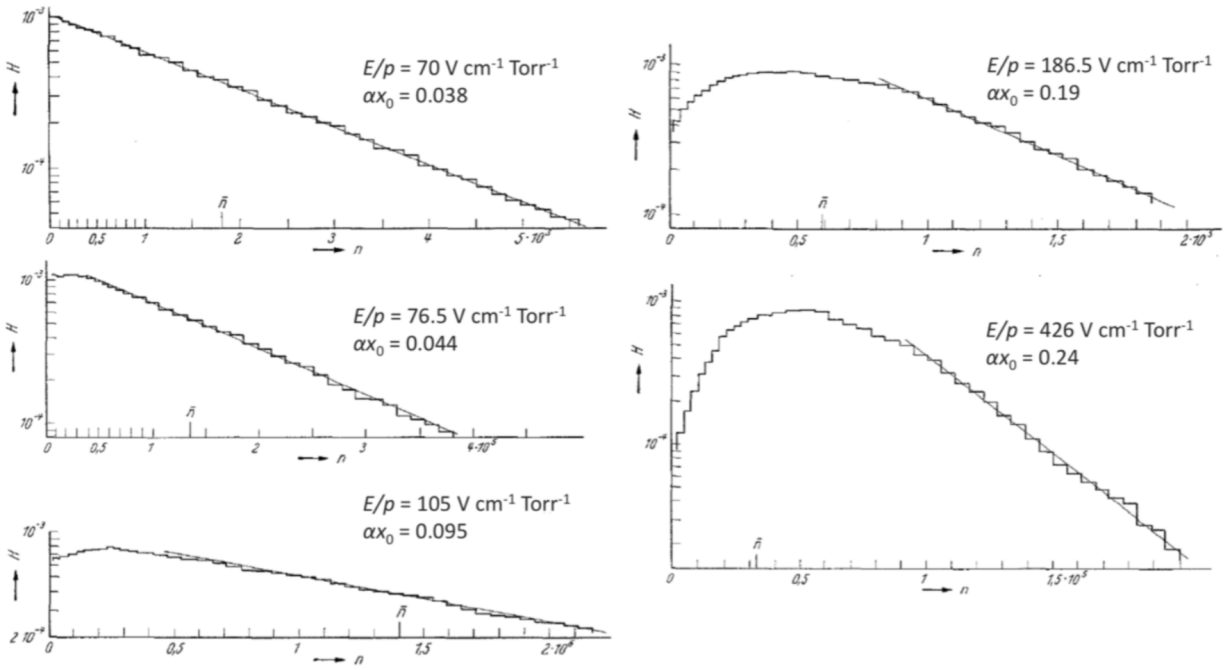

Figure 4.11: Avalanche distributions at different chi values. At lower reduced field values the distribution is basically exponential but as the field increases it starts to peak near the mean avalanche multiplication value. This explains why thin GEMs, with a higher reduced field, exhibit a lower gain resolution than THGEMs. Taken from Ref. [94].

$$f_0 = \frac{(2e^{-\chi} - 1)^2}{4e^{-\chi} - 2(e^{-\chi})^2 - 1} \tag{4.12}$$

where f_0 is the avalanche variance at infinite gain. This shows the complicated relationship between the variance, the reduced field, and the gain, and the plots on the right of Fig. 4.12 shows how χ relates to f_0. It can further be shown, by assuming each avalanche is independent and follows the same distribution, that for uniform fields:

$$f(G) = f_0(1 - \frac{1}{G}) \tag{4.13}$$

where f is the variance of the avalanche distribution at a gain of G.

Fig. 4.11 shows how the avalanche distribution changes as the reduced field is increased, and it is seen that the variance decreases. χ obtains a maximum value as a function of the reduced field and Legler showed that this maximum χ value corresponds to a minimum f_0 value, see the plots on the right of Fig. 4.12. The bottom plots in Fig. 4.12 were made by using Eq. 4.4 for α and setting $U_0 = U_i$ where U_i is the first ionization potential, $\approx 21.3\,\text{eV}$ for $HeCO_2$, [97].

We can now start to make sense of the the asymptotic resolution behavior for the thin GEMs

compared to the THGEMs. The difference in the χ values for between the double and single THGEM is much greater than between the triple and double thin GEMs, as the thin GEMs are near the maximum value of χ. This smaller χ values correspond larger f_0 values, and the larger difference in χ values for the THGEMs also corresponds to a larger difference in f_0. From Eq. 4.10 we recall that $f_0 \sim \frac{\sigma_G}{G}_\infty$, so we see that this behavior is expected. We exploit this relationship further in the next section.

4.3.6 Asymptotic detector resolution and the Fano factor

Using the b values from Table 4.1, or equivalently the $\frac{\sigma_G}{G}_\infty$ values from Fig. 4.10, we can calculate f_0 values for each data set. The asymptotic resolution values can then be squared, plotted against the corresponding f_0 values, and a χ^2 - minimization can be preformed representing Eq. 4.9. The vertical axis of this fit line will then be proportional to the Fano factor, F. The f_0 values were obtained as follows:

Using the a values from Table 4.1, as the gain at which the resolution reaches its asymptotic limit, and inserting these into Eq. 4.1 gives a corresponding E-field value. This value is the E-field at which each prototype reaches its asymptotic gain. Along with the A and B values from Table 4.2 as $\frac{B}{A} = U_0$, these values can be used in Eq. 4.11 to calculate a χ value. Eq. 4.12 can then be used to calculate a f_0 value for each data set at infinite gain. Then the corresponding asymptotic gain resolution values, $\frac{\sigma_G}{G}_\infty$, are squared and plotted against the obtained f_0 values. The resulting plot is Fig. 4.14.

The top plots in Fig. 4.13 shows χ vs. reduced field and f_0 vs. χ from all seven $HeCO_2$ data sets, listed in Table A.3, and the same general trend is observed as for the individual values in Fig. 4.12. To measure the Fano factor only six of the seven data sets were used, the bottom plots in Fig. 4.13. The D^3 - Micro data set was removed because the stability was not monitored during this time and, as a result, there are no errors associated with any of the gain values. Because there are no errors on these values the fit parameters of Eqs. 4.1 and 4.2 have artificially small errors which skew the values going into Fig. 4.14. Using the six data sets we get a central value for the Fano factor in $HeCO_2$ (70:30) of $F = 0.530$, and a lower and upper value of $F = 0.528$ and $F = 0.533$, respectively.

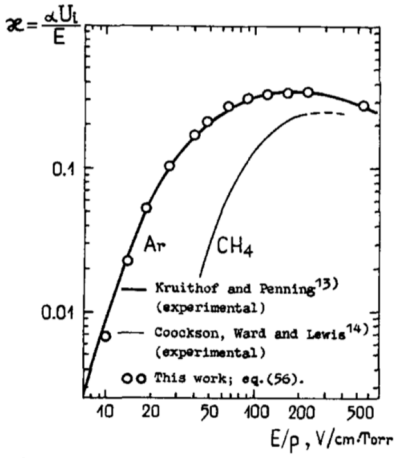

Fig. 3. The behavior of $\varkappa$ as a function of E/p for argon and methane.

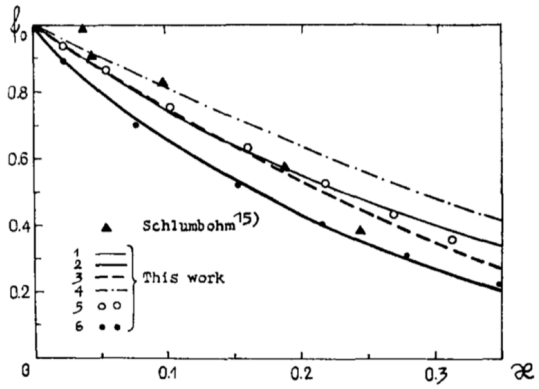

Fig. 4. Dependence of the relative gas amplification variance f_0 on $\varkappa$. 1. eq. (19), $U_0 = 0.72\ U_1$; 2. eq. (19), $U_0 = U_1$; 3. eq. (27b), $p_1 = 1/2$, $\varkappa_0 = 2$, $U_0 = U_1$; 4. eq. (23), $U_0 = U_1$; 5. and 6. eq. (56); two sets of q_{el}, q_{ex} and q_1.

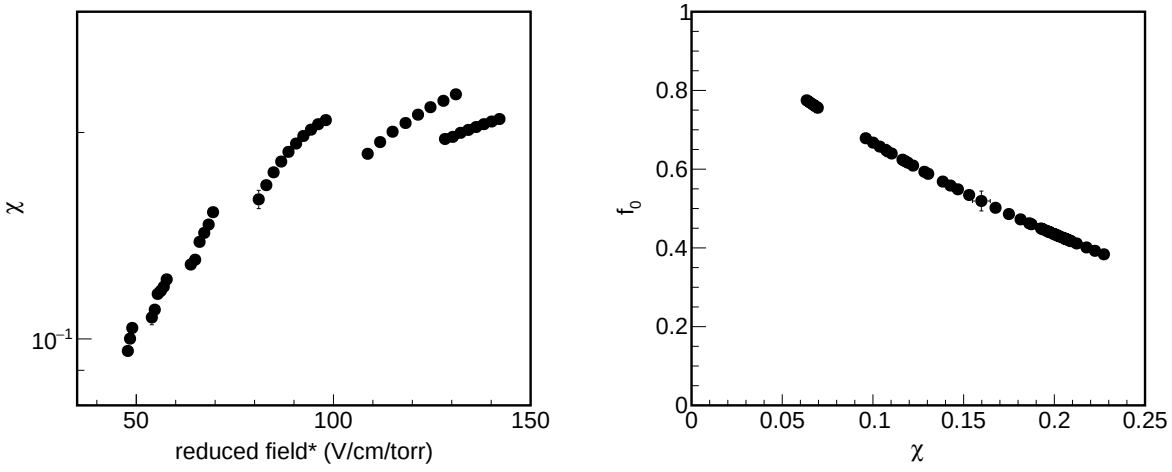

Figure 4.12: Left: χ vs reduced field. Right: f_0 vs. chi. Legler showed that the maximum value of χ corresponds to a minimum value of f_0. Top: Taken from Ref. [13]. Bottom: All seven $HeCO_2$ gain data sets listed in Table A.3.

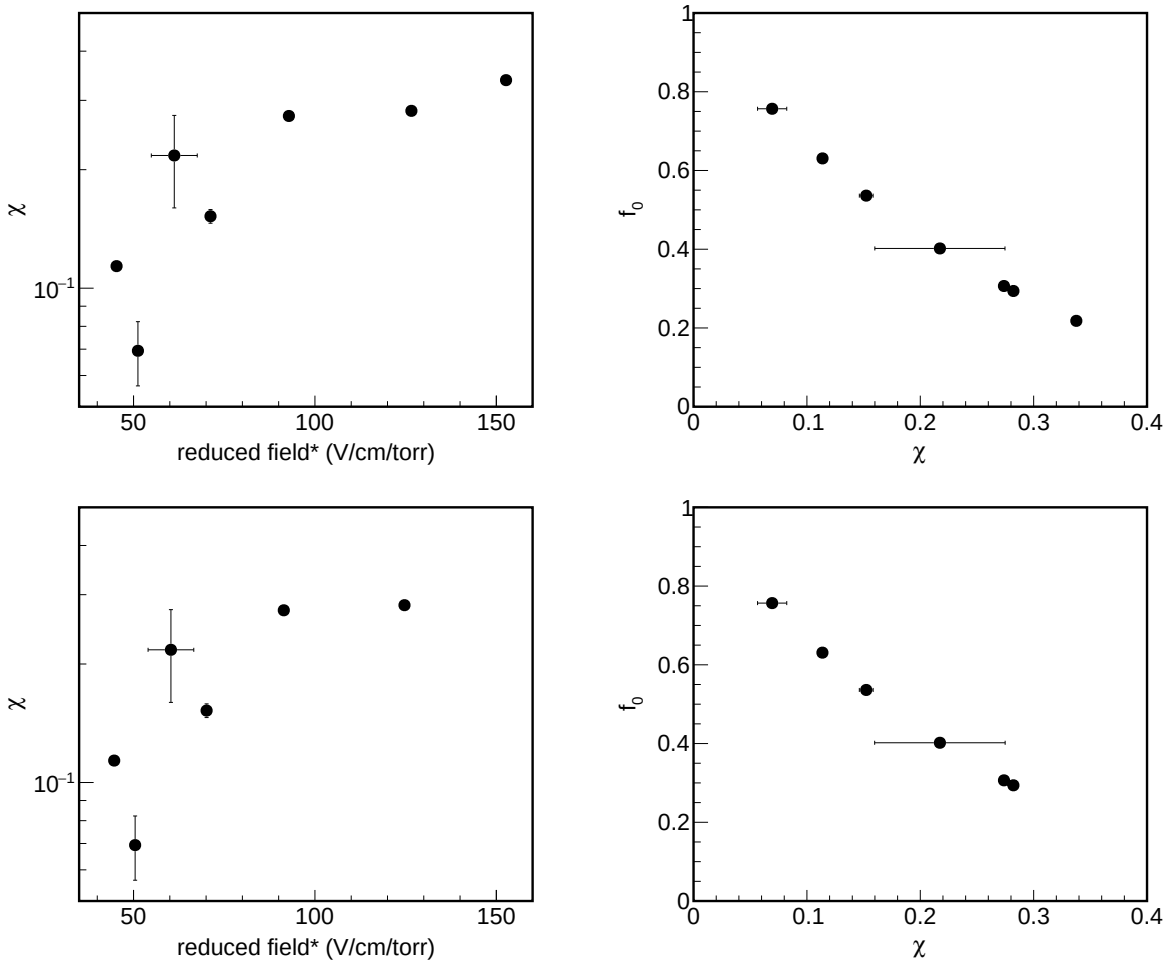

Figure 4.13: Left: χ vs. reduced field. Right: f_0 vs. chi. Top: All seven $HeCO_2$ data sets listed in Table A.3. Bottom: The six data sets, the seven listed in Table A.3 minus D^3 - Micro, used for measuring the Fano factor. See text for discussion.

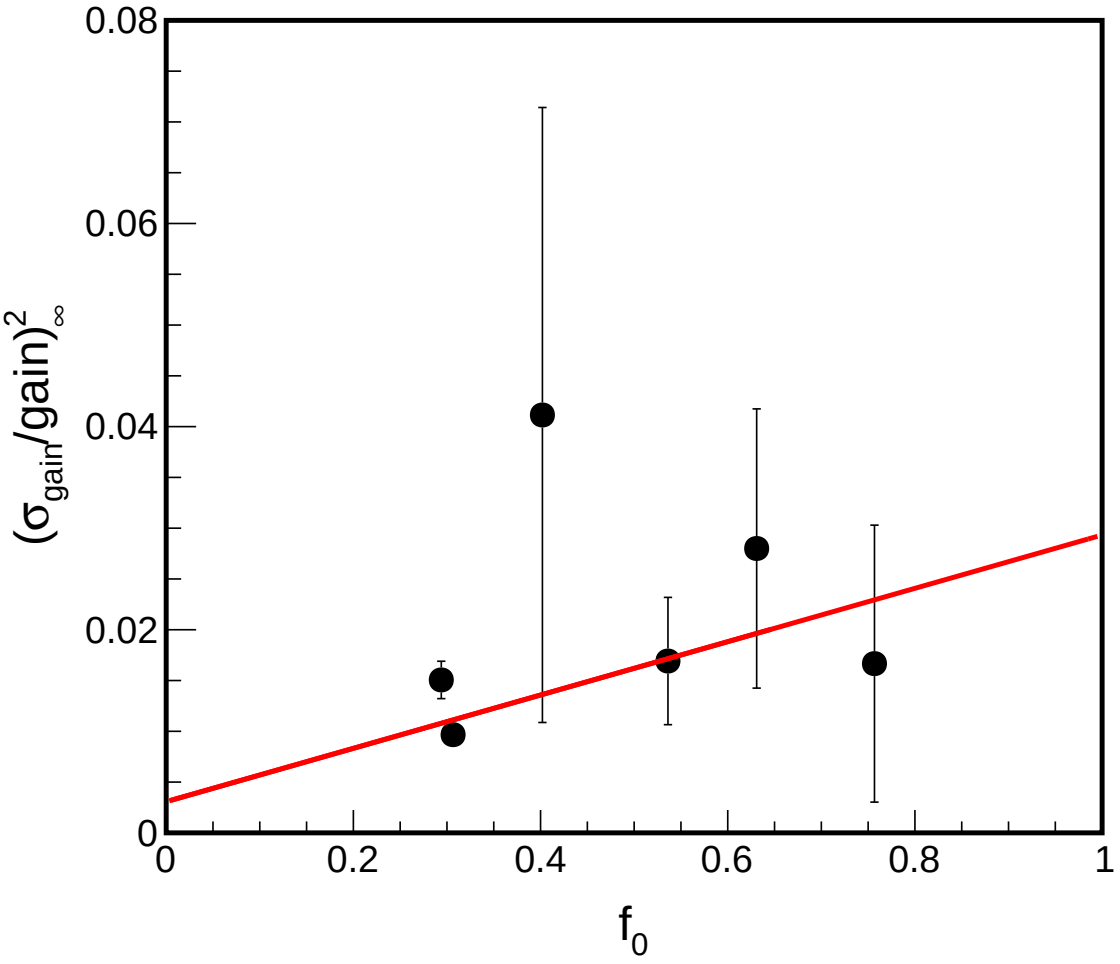

Figure 4.14: Asymptotic gain resolution values vs. their corresponding avalanche variance values at infinite gain. The red line is a linear fit representing Eq. 4.9. The vertical axis of the fit line is proportional to the Fano factor, F.

4.4 $ArCO_2$ gas: Energy dependence

4.4.1 Overview

In this study, using the D^3 - Micro prototype, the gas gain was measured with two different sources in $ArCO_2$, with a ratio of 70:30, at atmospheric pressure. 1) An uncollimated ^{55}Fe disk source was placed on the mesh above the double GEM stack so the photons would enter the drift gap and interact with the target gas. 2) An uncollimated ^{210}Po disk source was taped to the side of the Delrin support structure so the α-particles would enter the drift gap perpendicular to the drift field leaving an ionization track. After drifting to the double GEM layer the avalanche charge was collected by a copper collection plate and sent through the amplifier chain to the PHA.

^{55}Fe in Argon

X-rays emitted from ^{55}Fe have an energy of $\approx 5.9\,\text{keV}$ and their dominate interaction with Argon results in the ejection of a K-shell photoelectron, which has a binding energy of $\approx 3.2\,\text{keV}$, via the photoelectric effect. As the Argon atom de-excites a X-ray with roughly the K-shell binding energy is emitted. Depending on detector geometry, it is possible for this X-ray to "escape" the sensitive volume of the detector, for instance, if the interaction is near the edge of the drift gap. When this happens the energy of that photoelectron is not measured and the detector records an energy of the incident X-ray minus the one that escaped, $\approx 5.9\,\text{keV}$ - $3.2\,\text{keV} = 2.7\,\text{keV}$. This creates a peak called the escape peak in addition to the main peak with the aforementioned energy, allowing two energy measurements per spectrum to be performed.

There was a large background present during the ^{55}Fe study which proved very difficult to model. It is likely that, in addition to the electronic noise floor, there was an additional component from the source being uncollimated. In an effort to account for this each spectrum was modeled two separate ways: 1) A steep power-law plus a linear model for the background were combined with the two Gaussian signal peaks. 2) The individual Gaussian peaks with no background consideration. This is shown in the top plots of Fig. 4.15 and a χ^2-minimization was preformed for each spectrum with both models, and multiple spectra were recorded at each V_{GEM} value. These values were then averaged to get a gain value and the largest difference between any one background and source fit were added in quadrature with the fit error for every V_{GEM} value. The same was done for σ to get the resolution values and this is where the large error bars in Fig. 4.17 originate.

^{210}Po

A Crystal ball function [84] was used to fit the α-particle peak from ^{210}Po in $ArCO_2$. The low energy tail here is a geometric effect: since the source was uncollimated the α-particles would take paths at various angles across the drift gap. The main peak results from the particles traveling in a line perpendicular to the disk source plane and depositing a larger percentage of their energy within

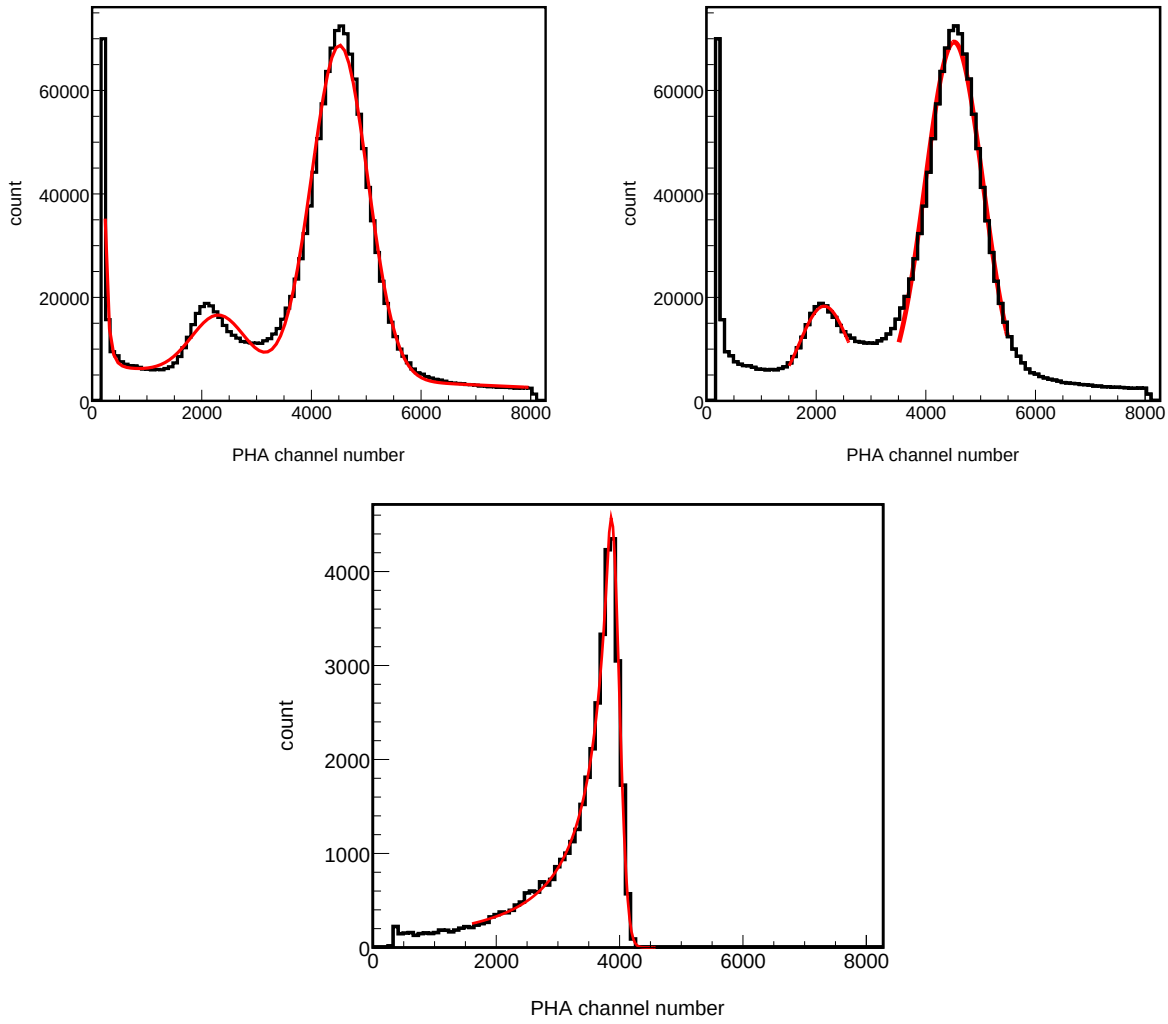

Figure 4.15: Fitted $ArCO_2$ pulse-height spectrum at atmospheric pressure. Top left: ^{55}Fe source plus background model; Top right: ^{55}Fe source fit and no background model; Bottom: ^{210}Po fit with a crystalball function.

the drift gap. Whereas the low tail results from any particles that deviate from a perpendicular path and leave the drift gap sooner depositing a lower amount of energy over the collection plate. The gain resolution here is taken from the upper end of the fit as this is the desired value of the charge collected.

4.4.2 Gain and gain resolution - $ArCO_2$

$ArCO_2$ has a W-value of 28.1 eV so a 5.9 keV photon from ^{55}Fe will produce $\approx$ 210 ion-pairs [97]. For the escape peak it was also assumed 210 electrons were produced and this can be seen in the right plot of Fig. 4.16 as the upper curve is the main peak and the lower is the escape peak. By

doing this, we can get a measurement of the escape peak energy by taking the average of the ratio of the gain values at each V_{GEM} because it must be true that each peak actually has the same gain. This gives a ratio of the main to escape peak of (2.06 ± 0.04) which results in the escape peak having an energy of (2.87 ± 0.04) keV, and this discrepancy is due to the attempt to model the background. The large error bars in the plot on the right of Fig. 4.17 are also a result of the difference between the background and source peak models, and the asymptotic limit is likely over-estimated, see Table 4.3 for all fit parameters extracted from Eqs. 4.1 and 4.2.

A 5.3 MeV α-particle Bragg curve obtained from SRIM, see Fig. 2.14, was used to estimate the amount of ionization collected. This resulted in (3.0 ± 1.5) MeV, where the large error is due to the exact source position being unknown. This was then scaled from the 210 electrons per 5.9 keV photon to obtain gain values for the ^{210}Po source. Note that this is not entirely accurate because the W-values do differ slightly between photons and α-particles [35] but, when considering the estimate of the energy actually being measured, this is a minor correction. It can be seen in the left plot of Fig. 4.17 that the resolution is much better for the α-particles than for photons from ^{55}Fe, and this is due to the energy dependance in Eq. 4.9. This can be exploited further for an energy dependance.

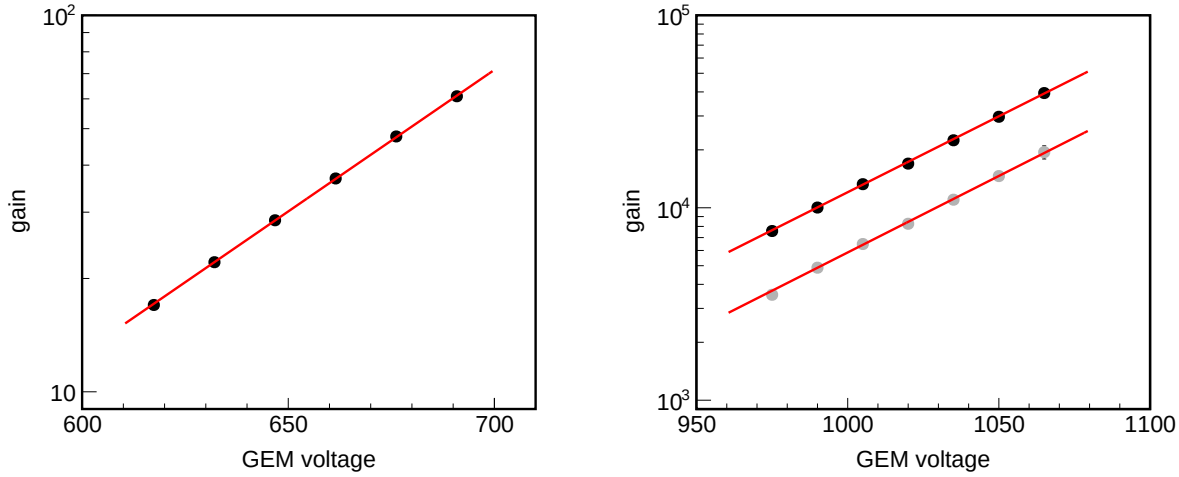

Figure 4.16: Gain vs total GEM voltage, V_{GEM}. Left: ^{210}Po; Right: ^{55}Fe; The gray and black points are for the escape and main peak in Argon, respectively. By assuming the two different energies are equal and, instead, experience different gains, the ratio of the gains can be used to measure the energy difference of the main and escape peak, see text for further discussion.

4.4.3 Gain resolution vs. energy

Using Eq. 4.10 as a guide, we can plot $\frac{\sigma_G}{G}_\infty$ for the three separate energies measured in $ArCO_2$, and this is done in Fig. 4.18. The three points are well described by:

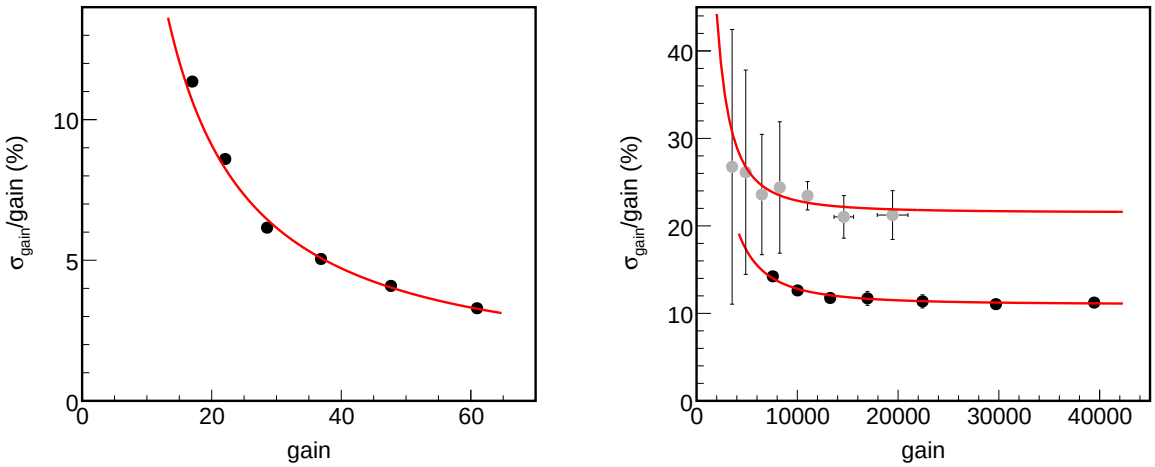

Figure 4.17: Gain resolution vs gain. Left: ^{210}Po - ≈ 4 MeV. Right: ^{55}Fe main peak - 5.9 keV (black points), ^{55}Fe - escape peak (light gray points). The Argon escape peak has roughly half the energy as the main peak and the large error bars are due to the background modeling, see text for discussion.

Table 4.3: Fit parameters characterizing the effective gain and resolution $ArCO_2$, as defined by Eqs. 4.1 and 4.2. *Large error due to large uncertainty in the amount of energy being measured with the α-particles.

Data set	V_1	V_2	a	b (%)
^{55}Fe escape peak	526 ± 17	126 ± 4	$(8 \pm 6) \times 10^4$	22 ± 2
^{55}Fe main peak	482 ± 9	127 ± 3	$(7 \pm 2) \times 10^4$	11.0 ± 0.4
^{210}Po	463 ± 9	136 ± 3	$180 \pm 120*$	1.43 ± 0.08

$$\sigma_G/G = \sqrt{d^2 + c^2/E} \tag{4.14}$$

where we have allowed for a more realistic error on the escape peak resolution. We obtain $d = 0.014 \pm 0.001$ and $c = 0.27 \pm 0.03$ $\sqrt{\text{keV}}$. Using Eq. 4.9, we can see that $c^2 = W(F + f)$ and, since $W = 28.1$ eV/pair in this gas, we conclude that $F + f \approx 2.7$. It is unclear what exactly this implies because neither F or f should have a value grater than 1. Considering f, even if the avalanche distribution is purely exponential, which is not the case at these high gains, $f = 1$. The Fano factor could have a value great than 1 in some cases involving NI gases where recombination is a large effect, but it should not this large for electron gases. It is likely that the large, poorly modeled background is the issue and is inflating the asymptotic resolution values. For instance, for the 5.9 keV peak of ^{55}Fe in $HeCO_2$ an asymptotic resolution value of 8.64% was measured, with the same detector, whereas here, in $ArCO_2$, it measured to be 11.0%. A difference this large is

unlikely and based on Fano factor values for the pure Helium and Argon, 0.2 and 0.16 respectively for electrons [35], $ArCO_2$ should reach a lower value than $HeCO_2$ if the avalanche variation is the same. Future measurements would benefit from multiple energy sources using multiple gain stages to constrain the Fano factor and the avalanche variation in multiple ways.

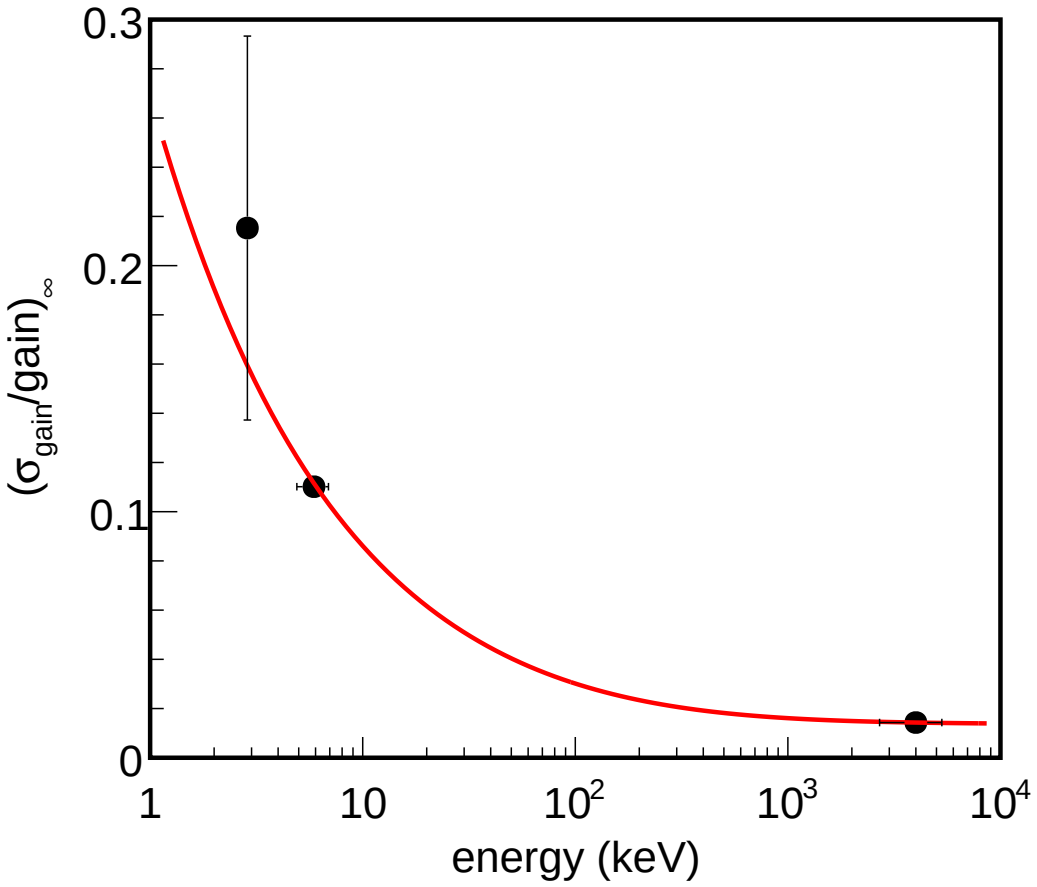

Figure 4.18: Gain resolution vs. energy in $ArCO_2$. The escape peak and main peak from ^{55}Fe are the lower energy values and alphas from ^{210}Po is the highest energy point.

Regardless, the implications of Fig. 4.18 are encouraging because when operating at high gain the electronic noise is overcome and what remains are the statistical fluctuations in the primary ionization and avalanche gain process. If the gain were high enough, and threshold/noise low enough, to allow single electrons to be measured the avalanche variance could be eliminated, [102] and this could improve for the lower energies. However, even a resolution of $\approx 20\%$ should allow for head-tail discrimination of a nuclear recoil, and $\approx$ keV of recoil energy corresponds to a WIMP mass of a $\approx$ GeV/c^2, which should allow for detailed low recoil energy measurements corresponding to low mass WIMPs.

4.4.4 First Townsend coefficient

The points on the lower left of the plots in Fig. 4.19 are from ^{210}Po and ^{55}Fe is in the upper right, where the escape peak gain has been corrected to match the gain of the main peak. As previously mentioned, Eq. 4.1 would be a straight line on these plots so a sense of the reduced field range that Eq. 4.1 is valid over can be gathered. A χ^2 - minimization of Eq. 4.5 is represented by the red lines and preforms much better for the two different sources, and the results are listed in table 4.4.

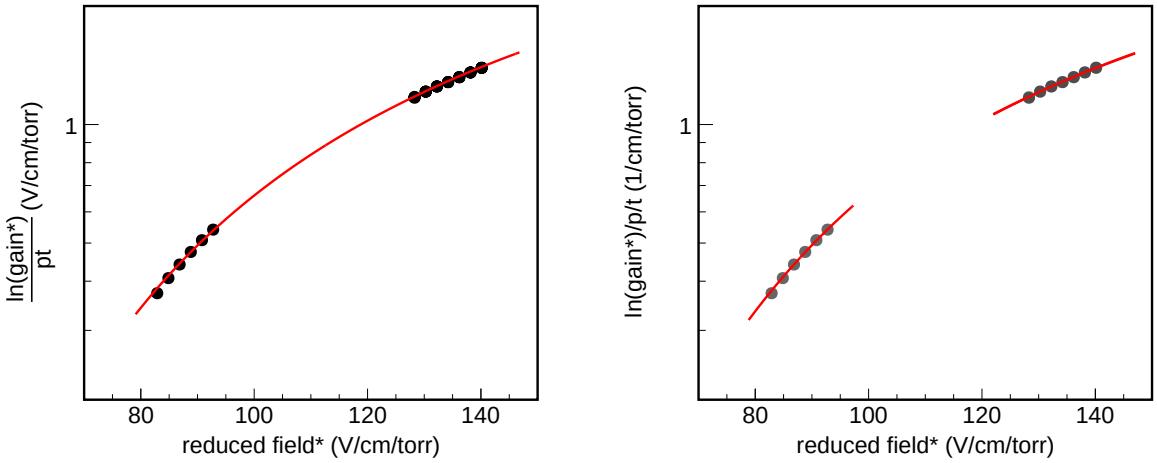

Figure 4.19: $ArCO_2$ data sets discussed plotted together. The red lines are fits of Eq. 4.3, see text for discuusion.

Table 4.4: Effective ionization potential measurements with $ArCO_2$. A and B are extracted from a χ^2 - minimization of Eq. 4.3.

Data set	Source energy (keV)	B/A
^{55}Fe - escape peak	2.87	29.4 ± 0.6
^{55}Fe - main peak	5.90	29.7 ± 0.6
^{210}Po	3000	26 ± 3
Combined	N/A	28.8 ± 0.6

It's interesting that the B/A values are in such agreement here as opposed to the values obtained in $HeCO_2$. The measured energies are very here different but the plots in Fig. 4.19 are only using the gain values, so it is not clear what would cause this. The resolution for the α-particles is much lower owing to the large number of primary charge carriers but, again, this should not be relevant in this plot. As mentioned above, if this data set contained lower reduced field measurements with the ^{55}Fe source, i.e. with THGEMs, they could then be compared with the points from the α-particle

source. It is suspected that they would not line up based on the $HeCO_2$ measurements and this could be disentangled, but this is left for further study.

4.5 SF_6: A Negative Ion (NI) gas

4.5.1 Overview

Negative ion gases have been gaining popularity within the directional dark matter community because of a few novel properties. As mentioned previously in Sec. 2.4.2, since the diffusion is much lower than with electron gases more of the recoil track information can be retained for longer drift lengths. CS_2 mixtures have been used successfully by the DRIFT collaboration [44], and recently many groups have started R&D with Sulfur Hexafluoride, SF_6. SF_6 has long been used by the electric power industry as a dielectric and insulator for HV work, and there is an abundance of literature about it. For directional dark matter experiments it is appealing because, unlike CS_2, it is non-toxic, and it has a large spin content in Fluorine which would allow for spin dependent limits to be set.

It still remains a bit of a mystery why gain is achievable in SF_6 at all [82] due to its high electronegativity. While it is true that to get gain in SF_6 a reduced field nearly an order of magnitude larger than in electron gases is needed, it is not clear that a typical GEM field should be strong enough to liberate an electron. However, many groups have measured gain in pure SF_6 [87] [93] [60].

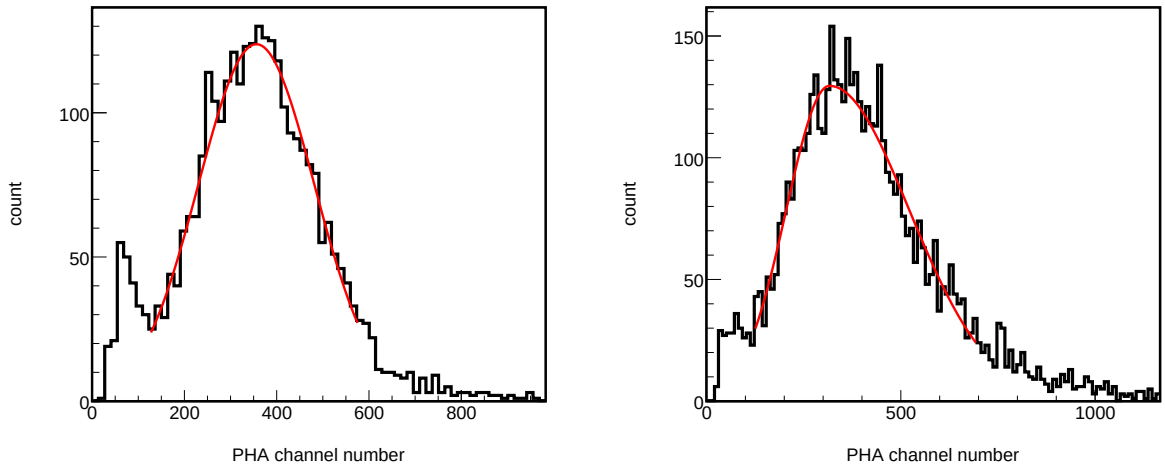

Figure 4.20: Typical THGEM high gain pulse height spectrum of ^{55}Fe in SF_6. Left: 20 torr Gaussian fit. Right: 40 torr modified Gaussian fit.

While a Gaussian distribution described the spectra at 20 torr adequately, a modified Gaussian was needed to properly model the spectra at 40 torr, and this seems to be a general phenomenon of

the gas as other groups have also seen this. The resolution is much worse than that of the electron gases studied and is due to the pulse heights varying more. By measuring the pulses individually some groups have seen lower resolutions [93] [87]. Table 4.5 shows the fit parameters extracted from Eqs. 4.1 and 4.2 for SF_6 and the large errors are from the large gain fluctuations in time.

4.5.2 Gain stability

As seen in Fig. 4.21, it was very difficult to maintain steady gain at any pressure and, because of the low pressure operation, the gas system had to be modified to allow for gas flow so a vacuum pump was connected to a 0.25" copper tube at the outlet of the vessel. The small diameter allowed for finer flow control allowing the pressure to stabilize.

The following is a timeline of the stability plots, taken at 40 torr, in Fig. 4.21: From left to right: 1) Between the first and second points a 40 torr gain study was completed. 2) Between the second point and mass of points in the middle, both 20 and 30 torr gain studies were completed. 3) The mass of points in the center is overnight. 4) In the empty space after the mass of points is when the vessel was pumped back down to vacuum to try and get the gain back to previous levels. 5) A drift and collection field study were attempted during the last gap between points on the right.

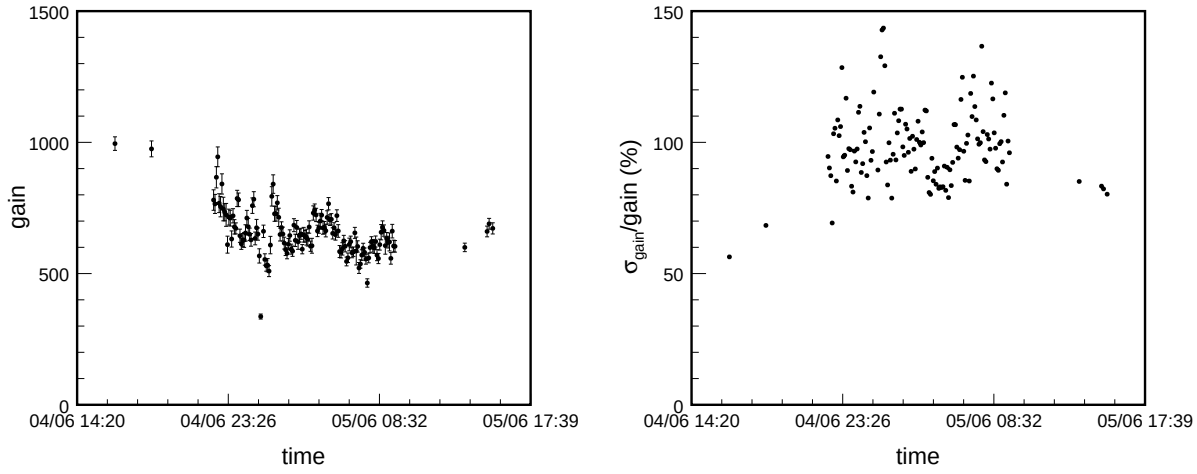

Figure 4.21: Gain stability curves for SF_6 data taken at 40 torr with the D^3 - Milli stage 1 THGEM setup, see text for discussion.

4.5.3 Gain and gain resolution

To measure the gain in pure SF_6 a ^{55}Fe radioactive source was used along with a W-value of 34.1 eV [75] resulting in 173 ion-pairs per photon produced. Unfortunately, due to the gain fluctuations we only present the 20 and 40 torr gain studies which were conducted as follows: The vessel was

pumped down to vacuum and flushed multiple times with the target gas and then refilled above 40 torr. Once gas flow was established, and the HV supplies turned on, the pressure was slowly lowered to the operating pressure. After the 40 torr study was complete the vessel was slowly pumped down to 20 torr, while decreasing the fields as necessary, and then the pressure was raised to 30 torr for an additional study. During the 20 torr study it was observed that not enough gas could be exchanged to counter the gain from decaying. While the 40 torr study witnessed the greatest stability and, although gain was achieved at 30 torr, the spectra were so degraded that they could not be fit properly.

As for the drift and collection studies, the rates varied wildly between spectra and it is not immediately clear at which field values the entire energy of the photon is being collected. If one requires the rates of all spectra to be nearly identical then only a few remain for analysis. Of the remaining, the fluctuations between adjacent spectra in time are of the order of those seen between spectra taken at different field values. So for the drift and collection fields it could be said, that once the rate stabilizes as a function of the field values, the gain and resolution are constant to within the fluctuations seen in time. All of the data presented here have at least those field values, see Table A.4 for all values.

It should also be noted that sparking was a major issue through all of these measurements and is what limits the detector from going to higher gain values. Once the sparking rate becomes high enough the avalanching field is essentially non-existent. So there is a fine balance to be struck between having enough voltage to see any signal and having too much which leads to very poor resolution, or no signal at all.

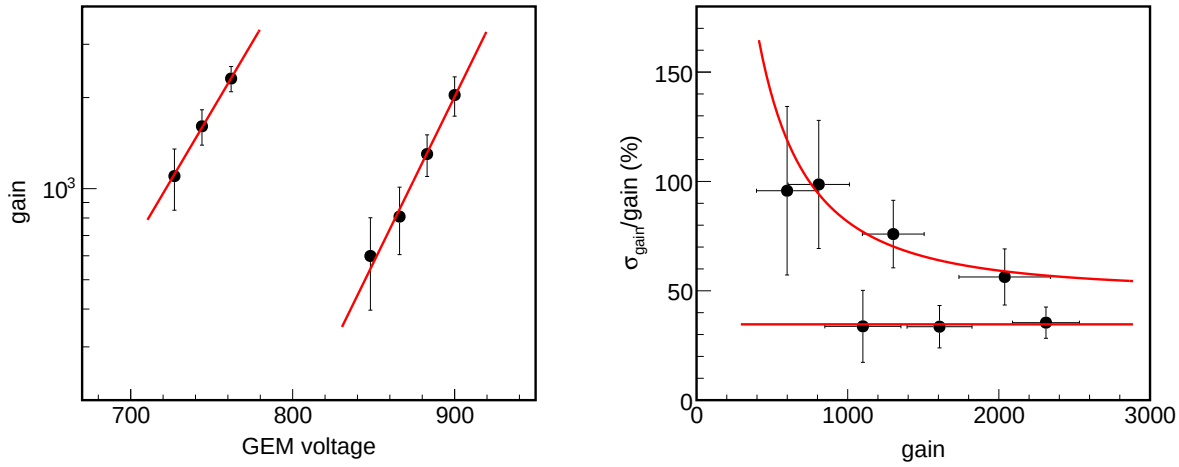

Figure 4.22: Left: Gain curves for 2 different pressures; 20 torr is on the left (lower voltage) and 40 torr is on the right (higher voltage). The vertical scale is one order of magnitude. Right: Gain resolution curves for SF_6. Lower resolution was achieved at 20 torr than with 40 torr but was not stable operation was not. Resolution values are consistent with what other groups have seen.

Table 4.5: Fit parameters characterizing the effective gain and resolution SF_6, defined by Eqs. 4.1 and 4.2. The * data set did not have measurements at low enough gain to converge Eq. 4.2 so a line was used instead.

Data set	V_1	V_2	a	b
20 torr*	391 ± 639	110 ± 197	N/A	34.7 ± 0.5
40 torr	598 ± 282	91 ± 94	$(6 \pm 3) \times 10^4$	50 ± 21

4.5.4 First Townsend coefficient

When compared to electron gases, SF_6 is in a much different area of parameter space in the plots in Fig. 4.23 which result in the fit parameters A and B having quite different values. However, when divided to get the effective ionization potential, B/A, they return values consistent with the W-value used, 34 eV, to within a factor of 2. While this is a large difference, it should be remembered that the errors on all the gain values are large and only a few points at each pressure were able to be measured.

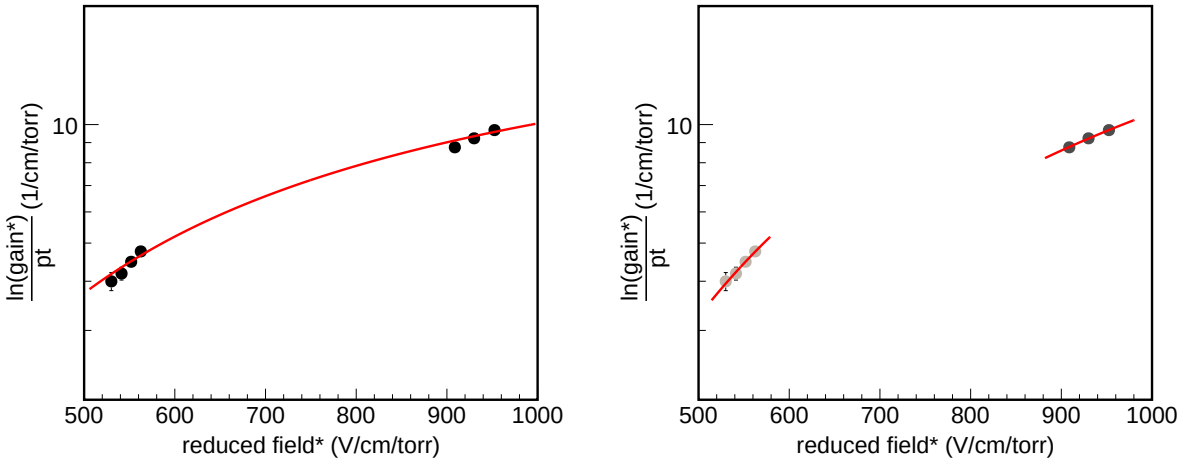

Figure 4.23: SF_6 data sets discussed plotted together. The 20 torr data set is the three points on the right at higher reduced field. The 40 torr data set are four point on the left. The red lines are fits of Eq. 4.3, to extract the fir parameters A and B, see text for discussion.

4.5.5 SF_6 remarks

While the author was able to achieve gain in SF_6 using THGEMs, it was never reproduced using thin GEMs and it remains unclear why this is the case. The reduced field is much higher in thin GEMs and all of the prototypes had a collection region, so recombination should occur regardless of the GEMs used. The exact mechanism of the detachment process is not well understood, but

Table 4.6: Effective ionization potential measurements with SF_6. A and B are extracted from a χ^2 - minimization of Eq. 4.3.

Data set	B/A
20 torr	25.9 ± 0.6
40 torr	17.1 ± 0.9
Combined	36.8 ± 0.7

this points to it having something to do with the amount of time spent in the avalanching field and not just the magnitude of the field. This needs further study.

While gain is achievable with SF_6, the high reduced field required and stability remain concerns, and it is not obvious that this gain would be achievable in a larger vessel with more outgassing. We generally seek higher gain than is realized here with SF_6 and there are a few reasons for this. With a higher signal/noise ratio, detector efficiency thresholds decrease, and higher gain increases the signal/noise ratio. It may be obvious that the detection threshold itself will decrease with higher gain, but event discrimination thresholds do as well, and it is likely certain directionality thresholds will also decrease. For instance, measuring the head-tail signal will be more efficient at a given recoil energy when more of the event ionization is measured than when less is.

The most ionization a detector can measure, for a given event, is all of it that was created in the primary interaction. When this is the case, we say the detector has high single electron efficiency because every single electron can be measured. For our detectors, outfitted with pixelized charge readout, a gain of $\approx$ 20k is needed to achieve high single electron efficiency [65]. This is due to the lateral extent of the ionization distribution extending over multiple pixels, and each pixel having a threshold of $\approx$ 2k. While a gain of 20k is achievable in various electron gases, it is much more difficult with SF_6, and this seems to be a general phenomenon of the gas. If, for whatever reason, high gains are not achievable in NI gases their role in future directional detectors may be limited. It is possible that the high single electron efficiency and gain stability of electron gases is more beneficial than the lower diffusion NI gases offer.

CHAPTER 5
DARK MATTER SEARCH WITH 3D PIXEL READOUT

5.1 Goal

In addition to achieving the lowest possible upper limit on the WIMP-nucleon scattering cross section, our ultimate goal is to achieve the lowest mass reach possible with our detectors. This is the most straightforward way to probe new parameter space with this type of detector. We also have the advantage of access to high definition pixel readouts which are capable of full 3D event reconstruction, see Fig. 3.1 for the coordinate system used in pixel chip measurements. The highly detailed reconstruction of recoil events in 3D allows for discrimination down to low energies, and this generally corresponds to lower WIMP mass. As a first step, we preform an analysis to set a cross section limit without using any angular information, and only a straight 3D line fit to the ionization distribution. This results in our first dark matter analysis with these detectors and is essentially a proof of concept. Roughly 5 times the amount of data used here is kept for unblinding after the angular distributions can be used.

5.2 Experimental setup: BEAST TPCs

Due to the high luminosity the upgraded SuperKEKB electron-positron collider is expected to achieve, large amounts of beam-induced backgrounds are expected near the interaction region. To ensure the success of the Belle II experiment these backgrounds need to be properly understood. A series of detector sub-systems, collectively known as BEAST II, was deployed prior to the Belle II operation to serve preform this background monitoring. One of the detector sub-systems was a series of eight small TPCs, Fig. 5.1 shows one, arranged in two groups of four symmetrically in azimuthal angle around the beam pipe, with one group forward, and one backward, of the interaction point. Their primary purpose was to measure the thermal neutron flux and distribution around the interaction point. Relevant dimensions are discussed next and more details can be found in Refs. [72] [62].

5.3 Data sets

5.3.1 Experimental data

For our purposes we note that the detectors were running continuously even when the beam and solenoid were turned off, and there was approximately 6 weeks of data taken with stable conditions. Data was taken at atmospheric pressure in $HeCO_2$ (70:30), and the TPCs operated with a double

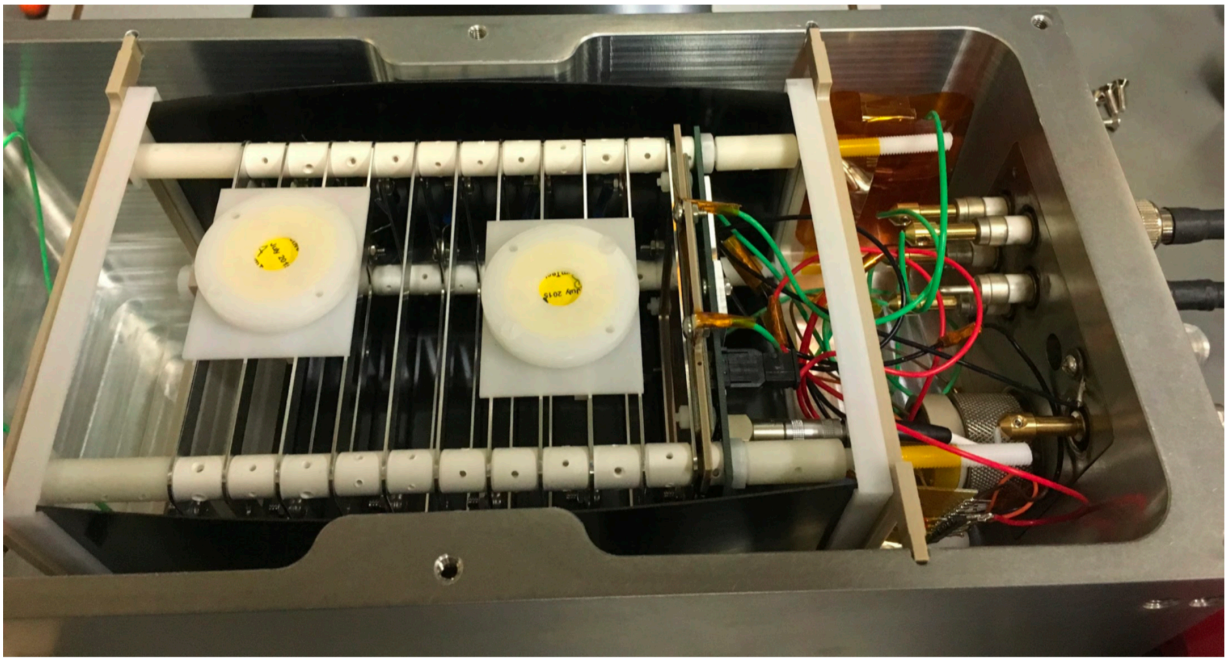

Figure 5.1: A BEAST TPC. It consists of an aluminum vacuum vessel, a 10cm field cage, and a FE-I4 readout. The two disks are α source holders, and the α-particles are used to monitor gain stability and can easily be vetoed.

thin GEM amplification stage, with an avalanche gain of ≈ 1500, and a FE-I4 pixel chip readout. Each TPC has a drift length of 10 cm for a fiducial volume of $10 \times 1.68 \times 2.0$ cm^3 TPC $\times$ 8 which results in a total fiducial volume of 268.8 cm^3. We use a 7.8 day subset, from July 18^{th} - 25^{th} 2018, of the six weeks to give an exposure of 2.44×10^{-5} kg $\times$ 7.8 days.

5.3.2 Monte Carlo samples

The group developed a full detector simulation to study the performance of multiple readouts, including high density pixel chips [24], and this framework used to generate nuclear and electron recoils. The Helium recoils and electron events were simulated using the event generating packages, TRIM [61] and [32], respectively. Both programs utilize specific gas configuration files which can be modified for an arbitrary mixture. DEGRAD has a 3D ionization distribution output while TRIM

was post-processed into a 3D distribution. TRIM was also configured to output all secondary collisions, which it does not do by default, because these need to be accounted for at low energies. Using these details, cascade particles can be reconstructed as well.

Once the primary distributions were developed, they were randomized in spatial position and "drifted" by adding a Gaussian smearing to the ionization distribution. The distribution were amplified with the respective diffusion that the avalanche process adds. They were then detected by pixels with the same dimensions as the FE-I4B, and noise and threshold effects were applied. Approximately 3000 electron events up to 30 keV and 3000 helium recoils up to 90 keV were simulated.

5.4 Analysis

5.4.1 Event reconstruction

Event reconstruction is detailed in Sec. 3.2.3. The specific drift field used in the BEAST TPCs is 530 V/cm and the drift velocity for $HeCO_2$ is calculated by Magboltz [32]. Once the data has been recored it goes through preprocessing stage where, using the coordinate system defined in Fig. 3.1, a straight line χ^2-minimization is preformed on every event. With this we have all the information needed to reconstruct the event. The event length, referred to as length when no ambiguity can arise, is defined as the difference between first and last pixel positions that went above threshold along the primary axis of the fit. The x, y and z coordinates are as described perviously. The angular coordinates, θ and ϕ, are defined in the chip coordinate, where θ is measured from chip $(x-y)$ plane to the positive z-axis and ϕ is measured from the positive x-axis. The recoil energy, referred to as energy when no ambiguity can arise, is reconstructed from the ToT converted to electron charge, defined previously, and the W-factor for the gas which is taken to be 35.075 eV/ion-pair for $HeCO_2$ (70:30) [98].

5.4.2 Event selection

Four selections to the data were applied to obtain the limit setting experimental sample. 1) Calibration α source selection (edge selection); 2) Maximum recoil energy, or WIMP mass, selection; 3) Absolute z selection; 4) Event length vs. energy (l/e) selection. The calibration source produced α-particles which cross the plane of the chip, as discussed above. The first selection requires all events be fully contained on the chip plane, so events that trigger pixels in either column 1 or column 80 or row 1 or row 336 are vetoed. There are thousands of these events and all are similar to the bottom track in Fig. 3.4. All plots shown below are understood to have this selection applied. Based on their distribution in the event length vs. event energy plane, see Fig. 5.3, the events that remain are largely electrons and some are nuclear recoils. The remaining selections are imposed to disentangle them and these selections are discussed in detail.

Maximum recoil energy (infinite WIMP mass) selection

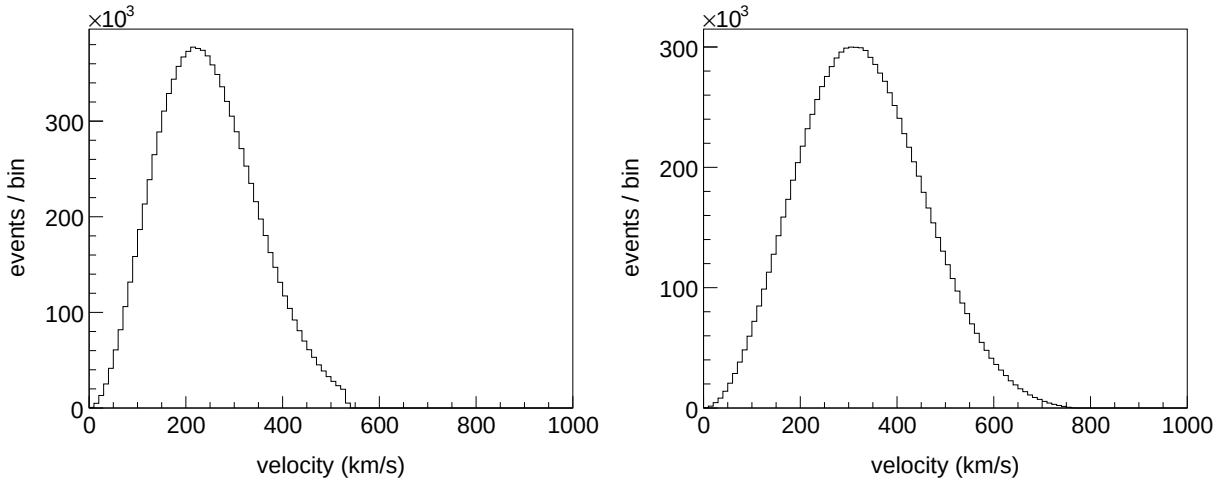

Figure 5.2: WIMP velocity distributions. Left: The WIMP velocity distribution in the galactic halo frame shown with the a galactic escape velocity cut off of 533 km/s. Right: Boosted to the Earth frame. This adds the galactic rotation velocity to the original halo distribution resulting higher energies due to the v^2 term.

Given an infinite mass WIMP we can construct a simple argument showing the maximum recoil a recoiling Helium nucleus can obtain from an elastic collision between the two. In this case the reduced mass is simply the mass of the Helium nuclei, and the maximum momentum exchange will be $2mv$ where v is the relative velocity between the WIMP and nucleus. This results in a maximum change in velocity to the Helium nucleus of $2v$ and thus a maximum recoil energy of $1/2(m)(2v)^2 = 2mv^2$. The galactic escape velocity is taken to be $\approx$ 533 km/s, [99], which when boosted to the lab frame is $\approx$ 750 km/s, see Fig. 5.2. This, along with the mass of a Helium nuclei $\approx$ 4 GeV/c^2, results is a maximum recoil energy of $\approx$ 50 keV expected in the detector. We obtain a precise value, by simulating one million WIMP velocity vectors and boosting them to the lab frame, of $E_r^{max} = 48.6$ keV. We relax this selection by 10% to keep from biasing our selection efficiency, see Fig. 5.6, which is discussed more in Sec. 5.4.3. The lower right plot in Fig. 5.3 is the MC and experimental data plotted as the length vs. energy with this selection applied. The other three plots are the MC and experimental data without this cut applied simply at different scales to illustrate key features, see the figure caption for more details.

Absolute z selection

Even though they are capable of 3D event reconstruction, TPCs have traditionally had one major drawback. The absolute position in the $x - y$ plane is generally known from the coordinates of the individual pixels or wires, however this is not the case in z. Because the z coordinate

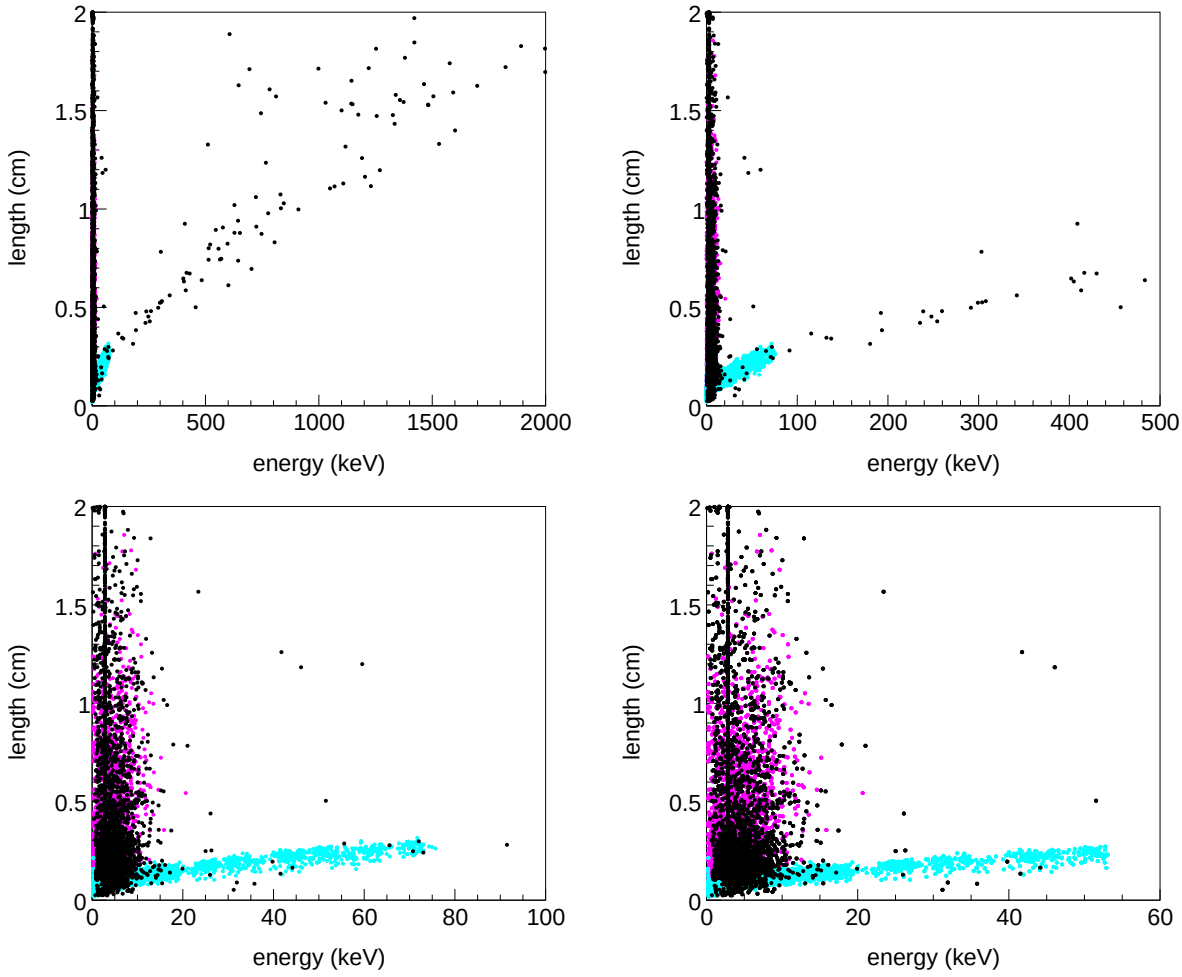

Figure 5.3: Event length vs. recoil energy for MC electrons (pink), MC Helium recoils (light blue), and experimental data (black). Top left, and right, and bottom left: Different scales of all data (only edge selection applied). Top plots show a larger energy range to emphasize the nuclear recoil band in experimental data extending diagonally from bottom left to top right. Bottom right: With infinite WIMP mass selection applied. In the bottom plots it is clear that above $\approx 12\,\mathrm{keV}$, selection of nuclear recoils should be near 100% efficient.

is reconstructed from timing information, relative to the start of ionization arrival on the readout plane, it is arbitrary. Without some other information it can't be known whether the event occurred high in z near the cathode plane, or low in z near the readout plane. Since many background events originate from either of these surfaces, it is crucial that experiments be able to discriminate and reject such events.

We use a method detailed in Ref. [72]. In summary, using the ionization tracks from the two calibration α-particle sources we are able to measure a difference in the width of the ionization distribution. The source located at a higher z position generates wider detected tracks than that

at the lower z position, and this extra width is due to diffusion as the ionization drifts through a longer distance. Because the absolute z position of these sources is known a relationship can then be established between the width of the ionization distribution and the z position in the detector. This method allows absolute z to be known within 1 cm, which is adequate for rejecting background events from the anode and GEM surfaces. It should be noted that work is still being done on this and the performance with very short tracks is not currently well understood.

Fig. 5.4 shows the absolute z selection. The top plot shows the distribution of absolute z in the experimental data and the redlines indicated the applied selection. There are 3604 (132) events before (after) this selection

Electron recoil rejection (length/energy selection)

Looking at the length vs. energy distribution after the absolute z selection, it is not immediately clear how to proceed. Given the differences in the 2D projection of the ionization onto the chip plane in Fig. 3.4, it's obvious that the charge is distributed differently for the electrons and Helium recoils. This is evident in the track length vs. energy plane above $\approx$ 10 keV where the Helium recoils band grows increasingly distinct from the electrons. We start by noting that the ratio of the number of events in experimental data to MC electrons remaining after the first three selections is 2.75:1. We choose the length/energy value such that if all the remaining events in data were electrons it would veto all but $\approx$ 1 event. This is a length/energy value of 0.0152 cm/keV and it is represented by the red line in the top left plot of Fig. 5.5, and the bottom left plot is the result of applying this selection.

This length/energy selection seems somewhat arbitrary and, for the sake of curiosity, an optimization study was performed which resulted in the plots on the right of The plots on the right of Fig. 5.5. The red line in the top right plot represents a slightly more relaxed length/energy selection value of 0.0192 cm/keV, and this value results in the best overall cross section limit. If obtaining the best overall limit is the goal then there is an optimization between the number of Helium recoils that are selected, which affects the efficiency, and the number experimental events allowed to remain in the final sample. This will be discussed in more detail in Sec. 5.4.3 but we note here that a length/energy of 0.0152 cm/keV (0.0192 cm/keV) leaves 16 (19) experimental events in the final sample. The resulting limits from the optimization study are shown in Fig. 5.12.

5.4.3 Efficiencies

As noted, the Monte Carlo Helium recoil and electron samples are generated up to 90 and 30 keV, respectively. One hundred events are generated for each one keV bin and this results in low statistics. Because of this, the efficiencies are handled differently for the two samples and is noted in their respective subsections below.

Helium recoils (signal efficiency)

The efficiency quoted here includes all of the simulated detector effects. This means that, even though one hundred events are generated per keV bin, not all of the one hundred events will be "detected". This is a result of the threshold of the pixel chip and, especially at low energy, there will be less than one hundred events in each bin. However, since this is a detector effect, we include this in our signal efficiency. So, our signal efficiency is the number of Helium recoils in each energy bin after applying a given selection divided by 100.

The top left plot in Fig. 5.6 shows the efficiency before selections and the top right is after the WIMP mass selection. The reason for relaxing the WIMP mass selection can be seen here: By vetoing higher recoil energy events the selection efficiency starts to become affected from the high energy side. The quenching factor, the fact that not all recoil energy becomes detected ionization, is also an issue, although for Helium it is fairly small, $\approx 10\%$ [24], at these energies. Given these issues we relax the selection by 10% to ensure we obtain a constant efficiency up to our desired recoil energy, E_{max}. The middle left plot in Fig. 5.6 shows the signal efficiency after the absolute z selection. The middle right (bottom) is then after a length/energy selection of 0.0152 cm/keV (0.0192 cm/keV). In the last two plots it can be seen that a 0.5 of maximum efficiency is reached at ≈ 15 keV, and these are the final efficiencies needed for the limit setting procedure. It should be noted that this is the true recoil energy Taken from Ref. the simulation, measured in keVr, whereas the actual detected energy, measured in keVee, of the events is always less due to quenching. This implies that these detectors are capable of achieving low energy thresholds when optimized for dark matter searches.

Electron recoils (rejection efficiency)

Do to the low statistics, we also quote an efficiency for electrons as opposed to a rejection factor. The top plot in Fig. 5.7 is with no selections applied. At lower energies, the threshold effect is again apparent, while at higher energies the electrons are likely leaving the fiducial volume resulting in a lower efficiency. In general, the electron tracks only have a high enough charge density to raise a pixel above threshold in areas where the trajectory is changing drastically, where there is a large curvature. As the electron energy increases the number of these areas contained within the fiducial volume decreases.

Of primary interest here is the effect of the length/energy selection and it's effect on rejecting the electrons. To avoid any confusion resultant from the the lower efficiency at higher electron energy discussed above, we define the efficiency differently for the electrons. We take the electron efficiency as the number of electrons remaining after a selection divided by the number of electrons "detected" in each energy bin. Thus the top plot in Fig. 5.7 is the only one where the number generated is used and its purpose is only for this discussion. By doing this the edge selection WIMP mass selection have very little effect and result in efficiencies near unity. We then start by showing

the efficiency after applying the absolute z selection, the bottom left plot in Fig. 5.7. The bottom right plot in Fig. 5.7 is after a length/energy selection of 0.0152 cm/keV. We note that an efficiency of zero implies that all electrons in that energy bin are rejected.

Fig. 5.8 illustrates the effect of different length/energy selection values. Each row is a different selection value, decreasing (fewer accepted electrons) from top to bottom. Each row consists of three plots: On the left is the length vs. energy with length/energy selection value indicated by the red line. In the middle is electron efficiency after applying the length/energy selection. And on the right is the Helium recoil selection (signal) efficiency after applying the length/energy selection. The specific values are listed in the figure caption. The two competing quantities in our limit setting procedure, discussed in Sec. 5.4.5, are the number of experimental events allowed by the length/energy selection, and the signal efficiency itself, specifically the lowest energy value at which it is non-zero. Of note is that the signal efficiency is roughly the same for the top four rows and then changes significantly in the fifth, as a result of encountering a larger portion of the recoil band. Essentially, once the entire recoil band is allowed, increasing the length/energy selection only allows for more experimental events while the efficiency remains constant.

The lowest energy reach of the efficiency will drive the cross section limit down to lower WIMP mass, so we want the to be as low as possible. Once this is achieved, increasing the selection value only allows for more experimental events (backgrounds) to containment the sample which drives the cross section limit upward. Thus the optimal value for the length/energy selection is the lowest value possible while still maintaining the lowest recoil energy reach, and is not simply whatever value rejects all the electron events. For us, this is a value of 0.0192 cm/keV which is illustrated in row four of Fig. 5.8. Row five is the length/energy selection discussed above.

Before moving on to the final event sample, there is an inefficiency that has not been discussed yet. The simulated events, both Helium recoils and electrons, were all generated from the middle of the pixel chip. As a result there are no events, or very few, which get vetoed by the edge selection. We make a simple argument: most of the Helium recoils in this energy range are $\approx$ 2mm in length, or less, and the chip is $\approx$ $(2\text{cm})^2$. So this is at most a 10% effect it can be corrected for in the future.

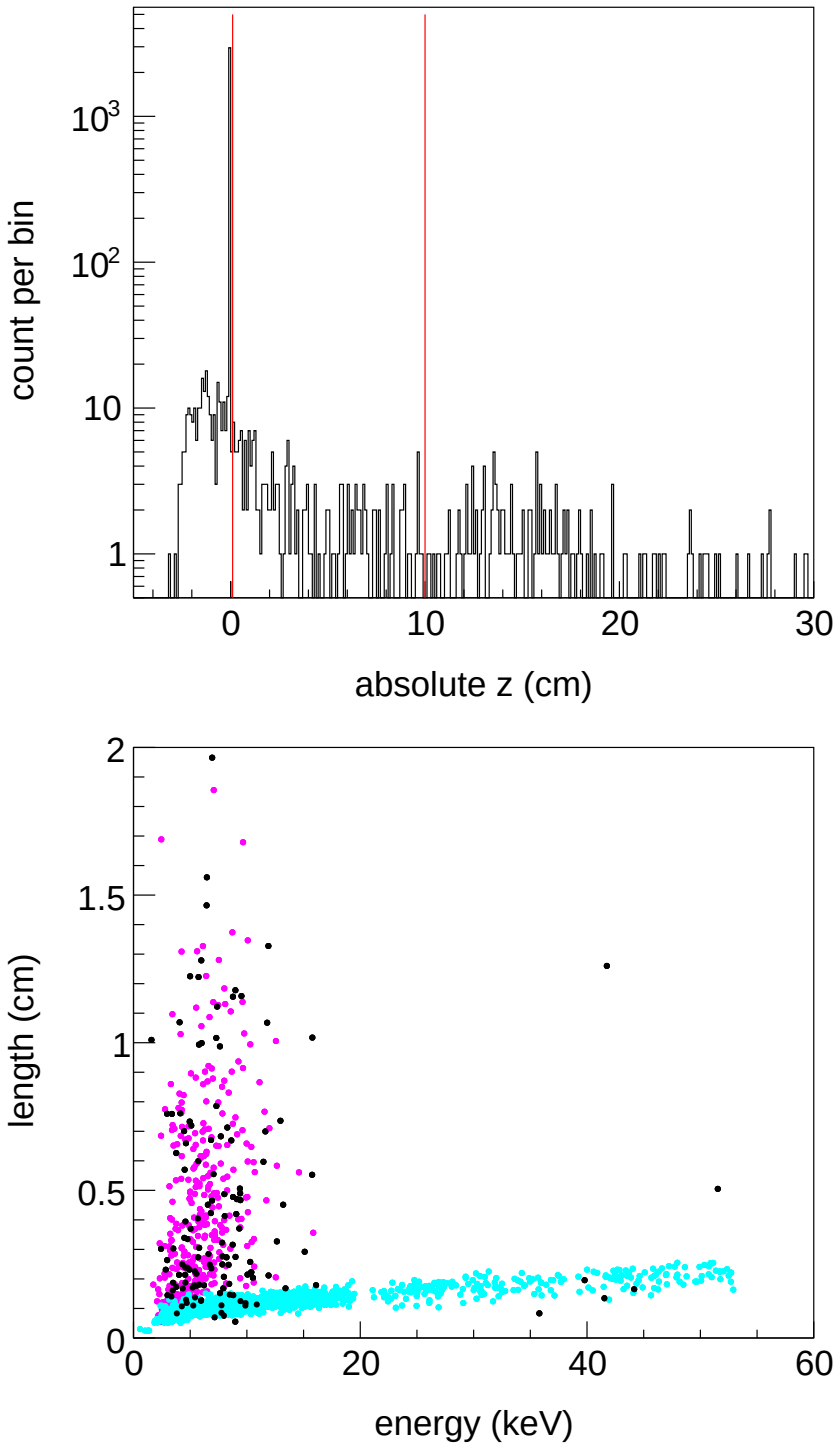

Figure 5.4: Absolute z selection. Top: Absolute z distribution of the experimental data after applying the edge and WIMP mass selections, note the log scale on the vertical axis. The red lines indicate the absolute z selection applied, events within the red lines are selected. Bottom: Length vs. energy distribution after applying the absolute z selection. Pink, cyan, and black are MC electrons, MC Helium recoils, and experimental data, respectively.

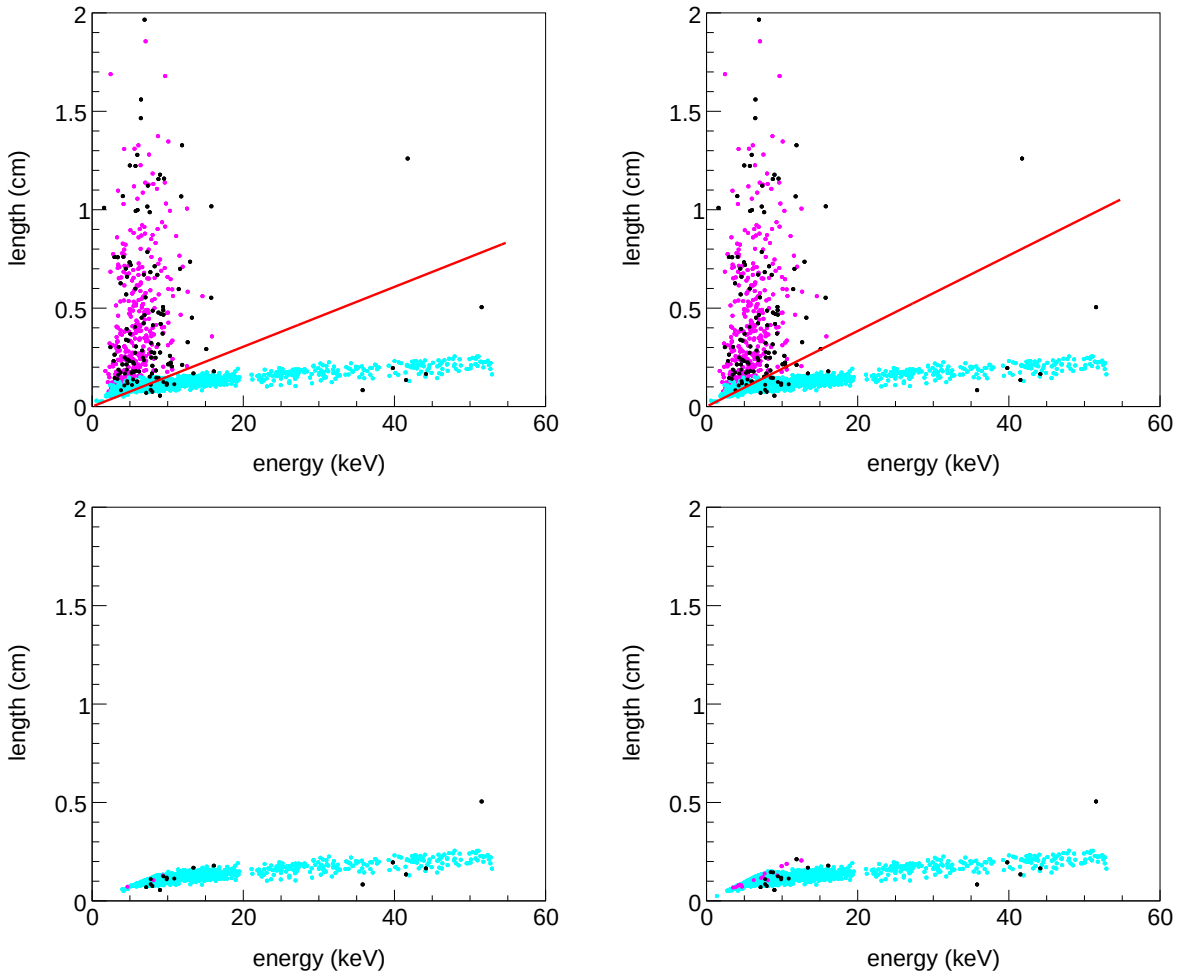

Figure 5.5: Length vs. energy plots. Top: After infinite WIMP mass and absolute z selections with length/energy selection value shown as red line. Bottom: Plots on the top with length/ energy selection applied. Left: Length/energy value of 0.0152 cm/keV. Right: Length/energy value of 0.0192 cm/keV. Energy is detected energy (keVee). Pink, cyan, and black are MC electrons, MC Helium recoils, and experimental data, respectively.

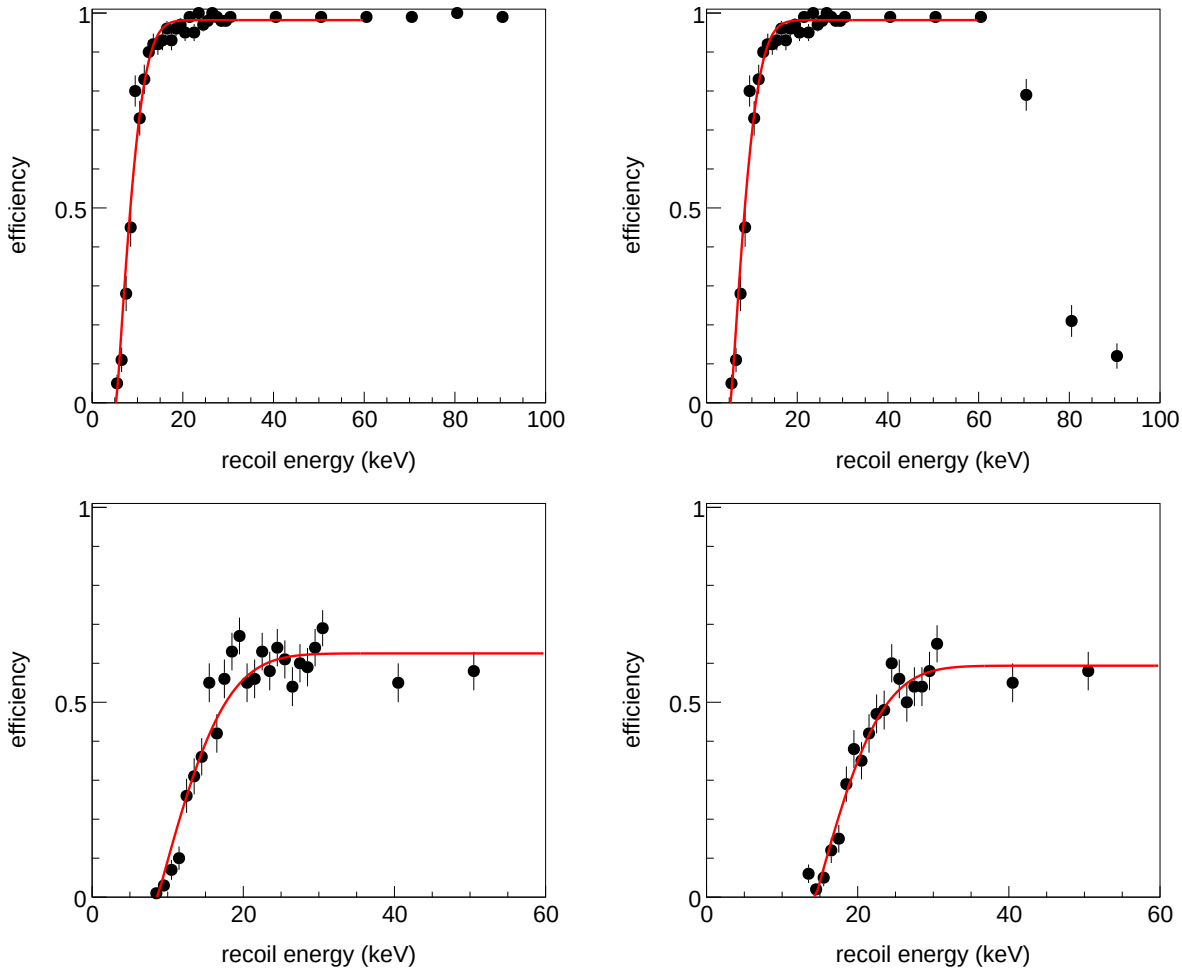

Figure 5.6: Signal efficiencies. Top left: Only edge selection applied. Top right: WIMP mass selection also applied. Bottom left: Absolute z selection also applied. Bottom right: Length/energy value of 0.0152 cm/keV selection also applied. This is the efficiency used in generated the cross section limit (black points) in Fig. 5.12.

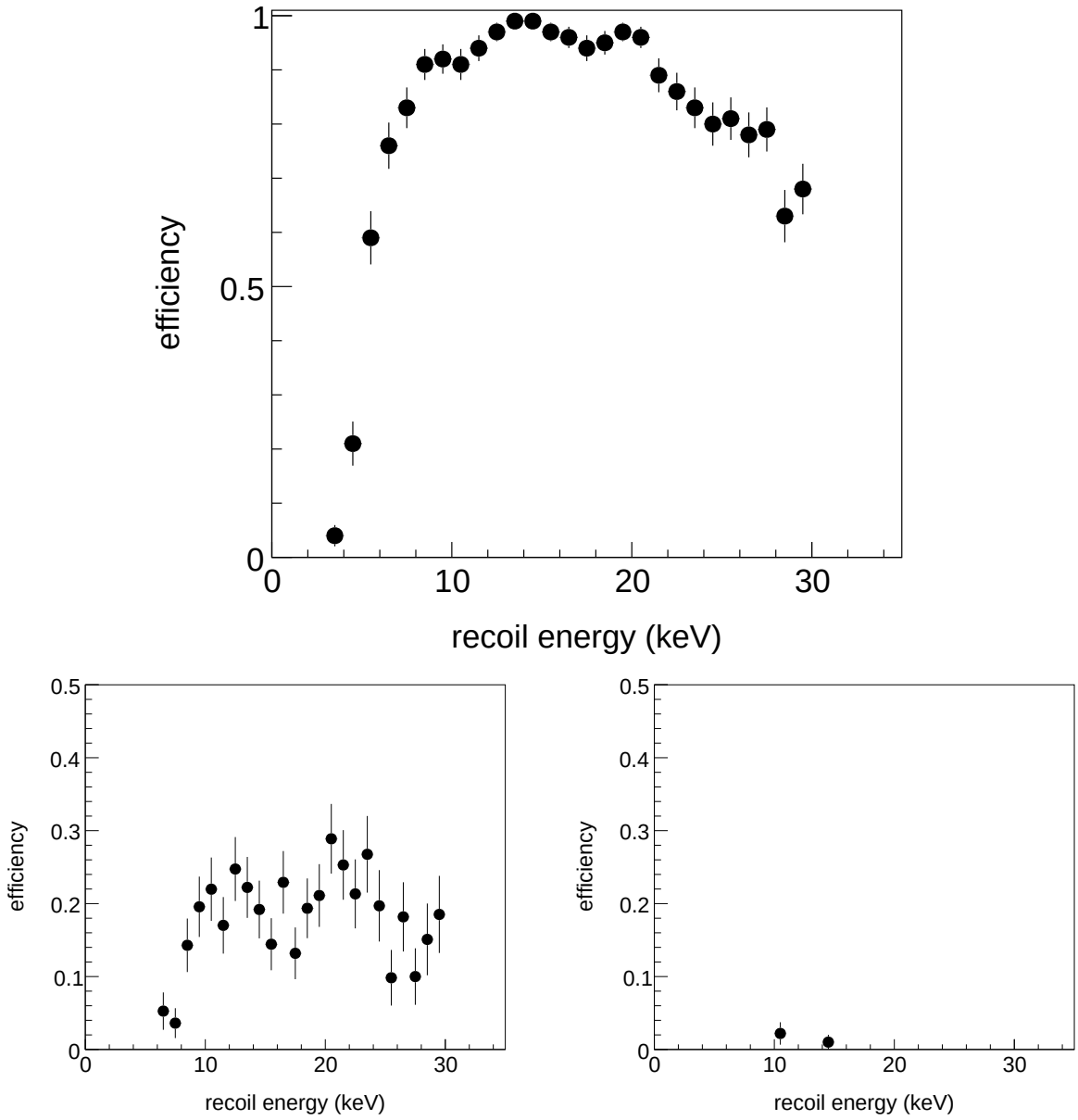

Figure 5.7: Electron recoil efficiencies. Top: No selections applied. Bottom left: Edge selection, WIMP mass selection, absolute z selection applied. Bottom right: Length/energy value of 0.0152 cm/keV selection also applied. Note that a value of 0 indicates that all electrons in that energy bin are rejected. See text for discussion.

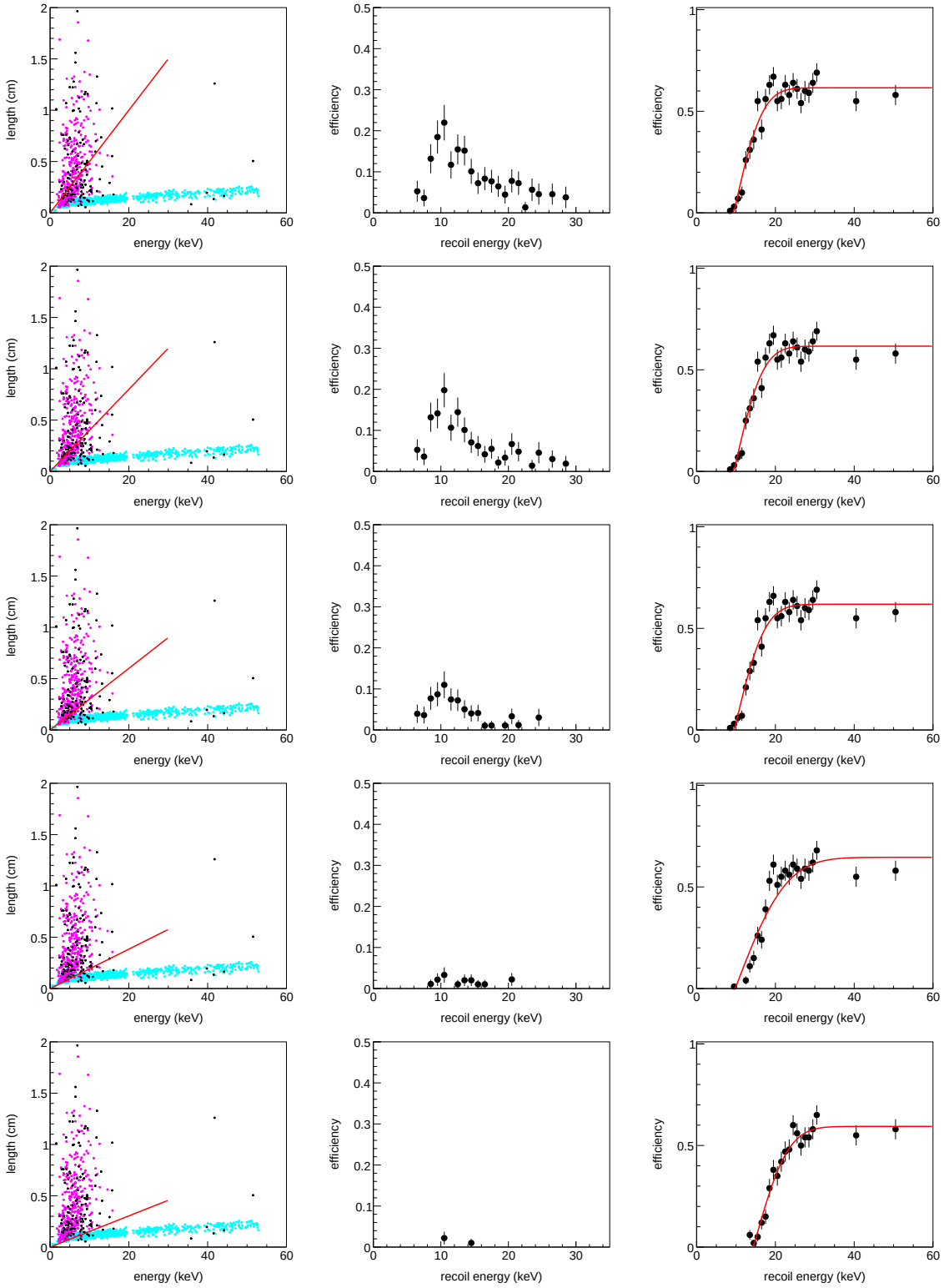

Figure 5.8: The effect on efficiency of varying the length/energy selection value. From top to bottom: 0.0500, 0.0400, 0.0300, 0.0192, 0.0152 cm/keV. Left; middle; right: length vs. energy; electron efficiency; helium recoil selection efficiency, respectfully. See text for discussion.

5.4.4 Final event sample

Fig. 5.9 shows the final samples used to set the limits in Fig. 5.12. We can note here that the limit is essentially computed based on the number of experimental events left in this final sample convolved with the signal efficiency described in Sec. 5.4.3. Ideally, we want zero events left in our sample but it seems that even with many more MC Helium recoils we would not be able to veto all the experimental events without several affecting the signal efficiency. The length/energy selection was made assuming all events were electrons. However, this is likely not true and the ones that remain are probably nuclear recoils, as this data was taken on the surface of the Earth and not shielded. Note there could be Carbon and Oxygen recoils as well, which have a lower length/energy than Helium. Also, referring back to the top plots in Fig. 5.3, recall the band of experimental nuclear extending out along the line of the MC Helium recoils.

Putting all this together leaves us with a couple of conclusions. 1) These detectors need to be somehow shielded, underground or otherwise. This will get rid of most of these higher energy recoil events 2) We need to come up with a better way to reject electrons at lower energies than the length/energy selection. This will allow a relaxation, or complete removal, of the length/energy selection and improve signal efficiency. The topology of the 3D event distribution, both charge and number of pixels, has not been used and this will likely prove to be a powerful discriminator. This is currently being studied. For now, we move to the setting of the cross section limit given these data.

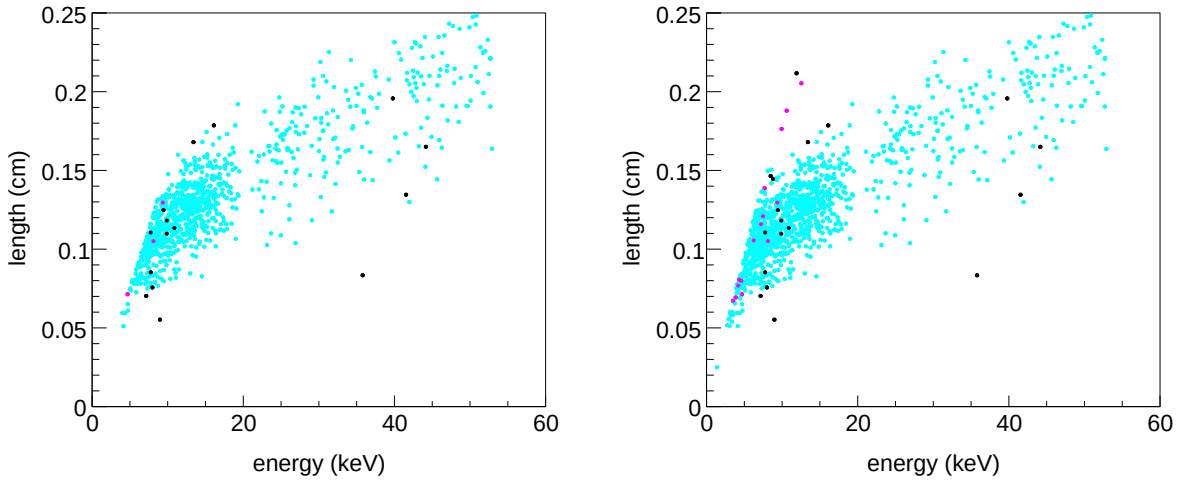

Figure 5.9: Final event sample. Top: With a length/energy selection value of 0.0152 cm/keV, 16 experimental events remain. Bottom: With a length/energy selection value of 0.0152 cm/keV, 19 experimental events remain. Pink, cyan, and black are MC electrons, MC Helium recoils, and experimental data, respectively.

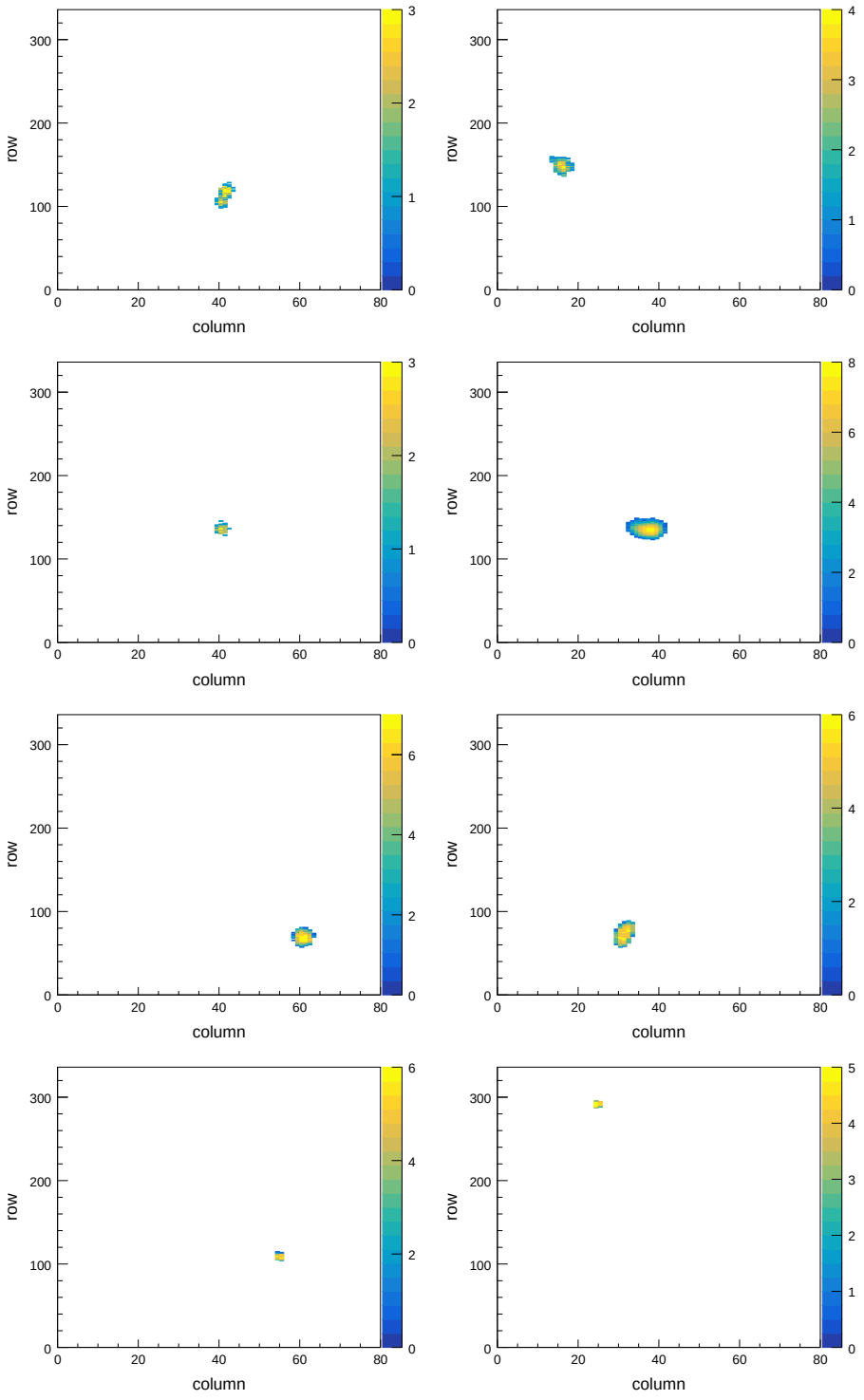

Figure 5.10: A subset of events passing selections for a length/energy selection value of 0.0192 cm/keV. Top row: MC electrons. Second row: MC Helium recoils. Last two rows: Experimental data. All experimental events passing selections, along with 3D displays, are located in Appendix D.

5.4.5 Spin Independent (SI) WIMP-nulceon scattering cross section limit setting procedure

We use the Poisson method for calculating the cross section upper limit which only relies on the number of experimental events remaining in the final sample. Assuming remaining events come from WIMP-nucleon interactions, the cross section must be at least a certain value. This is the value we calculate for the upper limit of the cross section. This method sets the weakest limit because, especially at low energies, detector backgrounds will artificially inflate the cross section and other methods will be explored in the future. For now a Poisson distribution is assumed, and to calculate the 90% confidence level we take the number of events remaining and set the Poisson distribution such that 90% of the distribution is above that number of events. Then the mean of the distribution, N, is then used to calculate the cross section at the 90% confidence level.

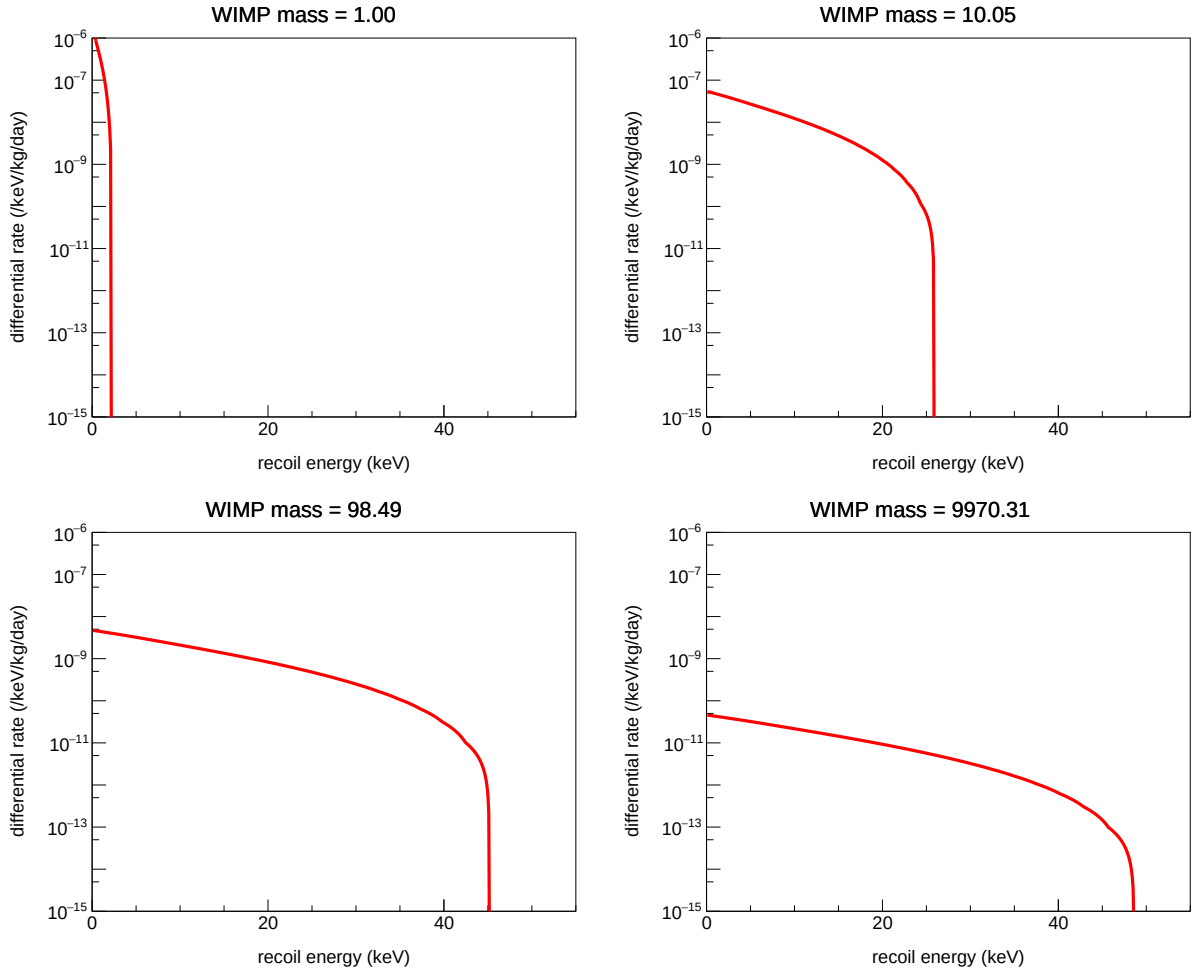

Figure 5.11: Expected differential event rate for scattering Helium with various WIMP masses. σ_t = 10^{-50} cm^2.

The procedure is as follows: 1) Calculate the rate, N_ϵ: 1a) Use Eqs. 2.17 and 2.21 to make the differential rate spectrum as in Fig. 5.11. 1b) Multiply this spectrum by the signal efficiency in Fig. 5.6. 1c) Integrate the resulting distribution to get N_ϵ. 2) Multiply N_ϵ by the exposure = 2.44×10^{-5} kg $\times$ 7.8 days. 3) Divide out by the "test" cross section, $\sigma_t = 10^{-50}$ cm^2, used to calculate the differential rate spectrum. 4) Divide by N given from the Poisson distribution. The resulting quantity is the inverse of the 90% confidence level upper limit on the spin independent WIMP-nucleon scattering cross section, $\sigma_{\chi n}$. We can write:

$$\sigma_{\chi n} = \frac{\sigma_t N}{N_\epsilon(\text{exposure})} \tag{5.1}$$

5) Repeat for many WIMP masses. Again, this sets weakest limit but other methods will be explored in the future, including the maximum gap method [112] and using the angular distribution of the events. There is a method called the maximum patch method which combines the two [78]. There is also the method of using the angular distribution of the remaining events and transforming it into the galactic frame, which would set the strongest limit. Once in the galactic frame it could be compared against various distributions, but terrestrial backgrounds should be isotropic, or very close to, in galactic coordinates. It could be compared with the path the Sun takes to claim, or refute, a neutrino signal, or against the expected WIMP dipole signal to claim, or refute, a WIMP signal.

5.4.6 Result

The top plot in Fig. 5.12 shows the result. We quote our best 90% exclusion limit as 1.05×10^{-32} cm^2 at a WIMP mass of 32.1 GeV/c^2 for a length/energy selection value of 0.0152 cm/keV (black points). We quote our best 90% exclusion limit as 6.90×10^{-33} cm^2 at a WIMP mass of 28.1 GeV/c^2 for a length/energy selection value of 0.0192 cm/keV (red points).

The bottom plot in Fig. 5.12 shows the upper cross section limit for twenty five different values of the length/energy selection starting with the most restrictive value of 0.0130 cm/keV (black points) which vetos all but one MC electron event. The length/energy selection value then increases to 0.0214 cm/keV in steps of 0.04 cm/keV where the stagnation of the detector efficiency has occurred, and the increasing number of remaining experimental events causes the limit to increase further. We discuss these results within the context of the direct, and directional, detection field in the following conclusion.

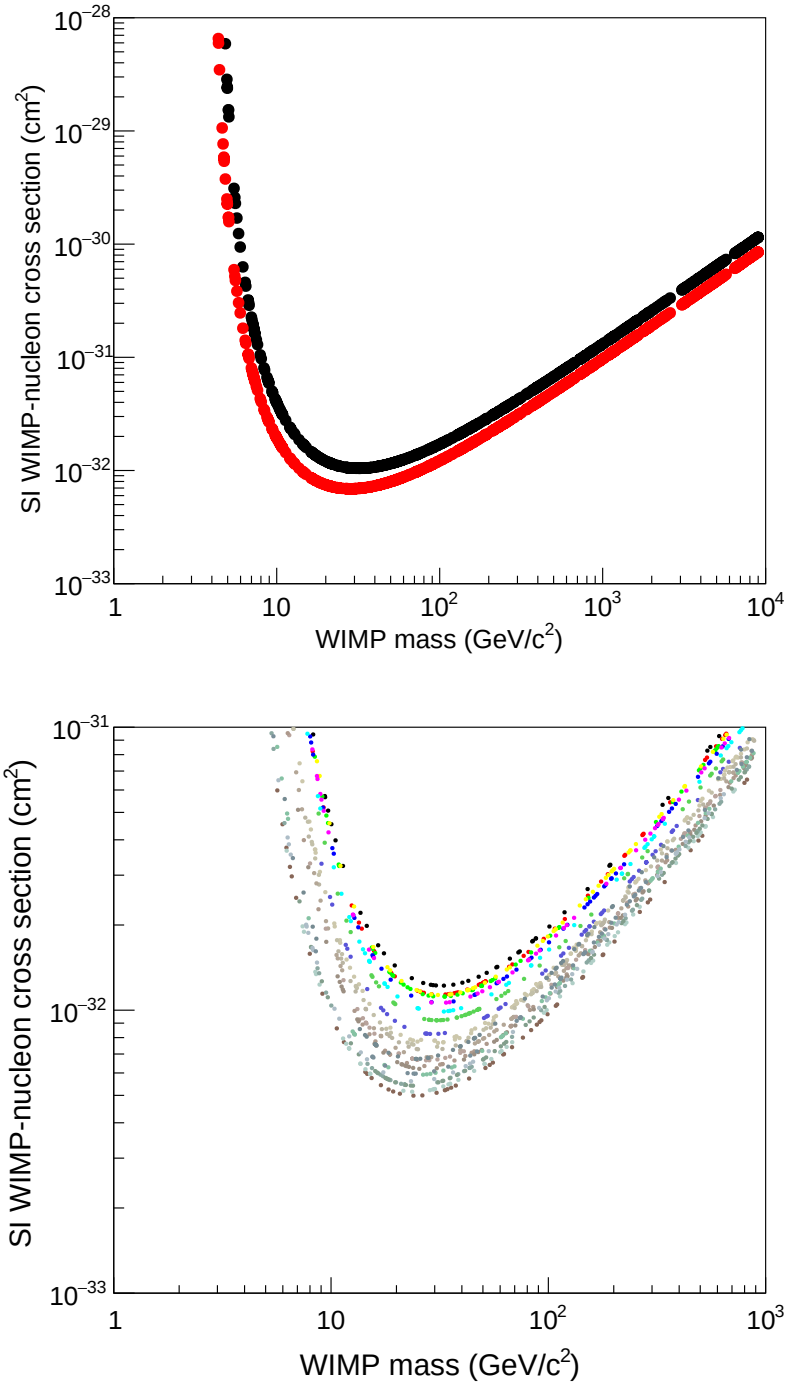

Figure 5.12: Spin independent WIMP-nucleon scattering cross section upper limits (90% confidence level). Top: Black (red) is for a length/energy selection value of 0.0152 cm/keV (0.0192 cm/keV). Bottom: Optimization study of the length/energy selection. Cyan points are for a length/energy selection value of 0.0152 cm/keV. The dark brown points (lowest cross section values) are for a length/energy selection value of 0.0192 cm/keV. The black points, a length/energy selection value of 0.0130 cm/keV, leave just one MC electron event in the final sample.

CHAPTER 6
RESULT COMPARISON, OUTLOOK, AND CONCLUSION

6.1 Comparing cross section results and larger directional detectors

The bottom plot in Fig. 6.1 shows a comparison of the best existing experimental results and a proposed directional detector. The proposed detector target material is a mix of SF_6, which allows for negative ion drift and increases the target mass, and Helium (^{4}He), which allows for lower mass reach. The different modes, "search mode" and "directional mode", correspond to different proportions of Helium. The directional mode assumes 740 torr of Helium, with a nuclear recoil threshold of 1 keV, and 20 torr of SF_6, with a nuclear recoil threshold of 3 keV for Fluorine. The search mode increases the SF_6 proportion to 200 torr, where less discrimination is exchanged for an increase of a factor of 10 in exposure . The live time is three years. One of the stated goals of this project, being proposed by the CYGNUS collaboration [24], is to start probing into the parameter space covered by the neutrino floor.

We note the minimum cross section for XENON1T falls at a WIMP mass of $\approx$ 30 GeV/c^2, which is very near where our minimum falls as well. We stress that our limit was set using neutron detectors and had the gain simply been increased to 15k from 1500, or the pressure lower than 1.0 atm., we would see our minimum move to a lower WIMP mass. This is important because the neutrino floor rapidly rises around 10 GeV/c^2 and this is quite possibly where the first coherent neutrino scattering signal [12] will be measured by a dark matter experiment.

We can immediately note that a 1000 kg detector running for three years would place our limit 10 orders of magnitudes lower. This mentioned because our TPCs were optimized for fast neutron detection, running with low gain and no background shielding. Once optimized for a dark matter search this technology will prove competitive. Further methods of discrimination are also being explored and the 3D ionization distributions will likely provide powerful event discrimination. In the end, the directional information of the events will be ultimate discriminator and any surviving the rudimentary selections imposed here will be transformed back into galactic coordinates and compared against an isotropic distribution. Background events are not necessarily a showstopper for detectors with directional capabilities because of this.

The top plot in Fig. 6.1 shows two additional limit curves in addition to the two presented in Sec. 5.4.5. The light gray curve is the result of the edge, WIMP mass, and absolute z being applied, but then setting the number of experimental backgrounds surviving to zero and not applying a length/energy selection. This justification for this is that during a proper dark matter search, these detectors would be underground or shielded in some other way. The absolute z selection

vetos backgrounds coming from detector components, and what remains after could be effectively shielded against.

The dark gray curve is provided here for speculative purposes, as it is at least slightly unrealistic. It is the result of applying only the edge selection and also assuming zero experimental backgrounds, which is the efficiency curve in the upper right of Fig. 5.6. While the number of backgrounds from internal detector components will likely not be zero, it is certainly possible that the current number would significantly decrease if the materials were optimized for a low-background dark matter search. This would improve the efficiency of the absolute z selection at lower energies. It is also possible that the absolute z efficiency will also be improved using more sophisticated fitting methods.

The message here is that if we properly optimized for a dark matter search, the mass reach of these detectors will fall somewhere in between these two gray curves. This coupled with 10 orders of magnitude in exposure would already make this a competitive technology, and this is without the aid of any angular event distributions. To gain a sense of 10 orders of magnitude in exposure we can make the following rough statement: Our current fiducial volume is $\approx 1\,\mathrm{cm}^2$ (readout) $\times$ $10\,\mathrm{cm}$ (drift) $\times$ 8 (detectors) $\approx 100\,\mathrm{cm}^3$. A detector with $1\,\mathrm{m}^2$ pixel readout and a 1 m negative ion drift running for three years would set a cross section limit roughly 7 orders of magnitude lower than our current limits.

6.2 Remarks on the gain

As mentioned in Sec. 4.5.5, it is not yet clear what the ideal target gas would be for a large TPC seeking directional capabilities. Sulfur Hexafluoride (SF_6), a Negative Ion (NI) gas, offers low diffusion allowing for low pressure operation, and long recoil tracks, but achieving high stable gain is difficult, at best. Electron gases offer high gain, and high single electron efficiency, but diffusion is also higher making low pressure operation more difficult. More experimental results from negative ion gases are likely needed before any final determination can be made.

Gas mixtures with SF_6 are currently under study [24], including $HeSF_6$ which would allow for longer recoils via the Helium content, while maintaining the larger mass and unpaired spin from the Fluorine content. A study similar to the one discussed in Secs. 4.3.4 - 4.3.6 for SF_6 would be useful. The gain vs. reduced field parameter could be mapped out which could inform the optimum gain value to operate with. It could also help determine if the gain resolution values seen here are to be expected, or if certain reduced field values might allow for better performance with NI gases.

6.3 Final summary

We have discussed our detectors, gaseous Time Projection Chambers (TPCs) with Gas Electron Multiplier (GEM) charge amplification and pixel charge readout, in detail. And how this combi-

nation of technologies results in the detailed 3D vector reconstruction of ionization distributions resulting from interactions of the target nuclei and incoming particles. We have tried to stress how important these types of measurements are to the directional detector community, and the impact they could have on the direct dark matter detection community at large.

We have also discussed the gain and gain resolution of these detectors in detail, and the role these quantities have in producing effective measurements. Different GEM-based gain stages were studied allowing for a description of gain data over a broad detector operational parameter space. The gain resolution and avalanche variance were also studied, and discussed, in relation to the energy resolution, indicating the viability of future detector measurements. We also discussed the relationship between the energy resolution and selections involving the energy and the head-tail measurement. Different gases were studied, including our first gain measurements with SF_6, a negative ion gas, including their possible role as the directional detection effort continues to move forward. And finally, we presented our first WIMP-nucleon scattering cross section limit with these detectors, and discussed what still needs to be done and what the field at large plans to accomplish.

The search for dark matter remains an exciting field and, with the next generation liquid noble gas detectors already funded, the next decade will likely see an encounter with the neutrino floor. Regardless of what happens beyond this, directional detectors will undoubtably serve a role. As we move past discovery, into BSM physics, their importance to the field will only continue to increase.

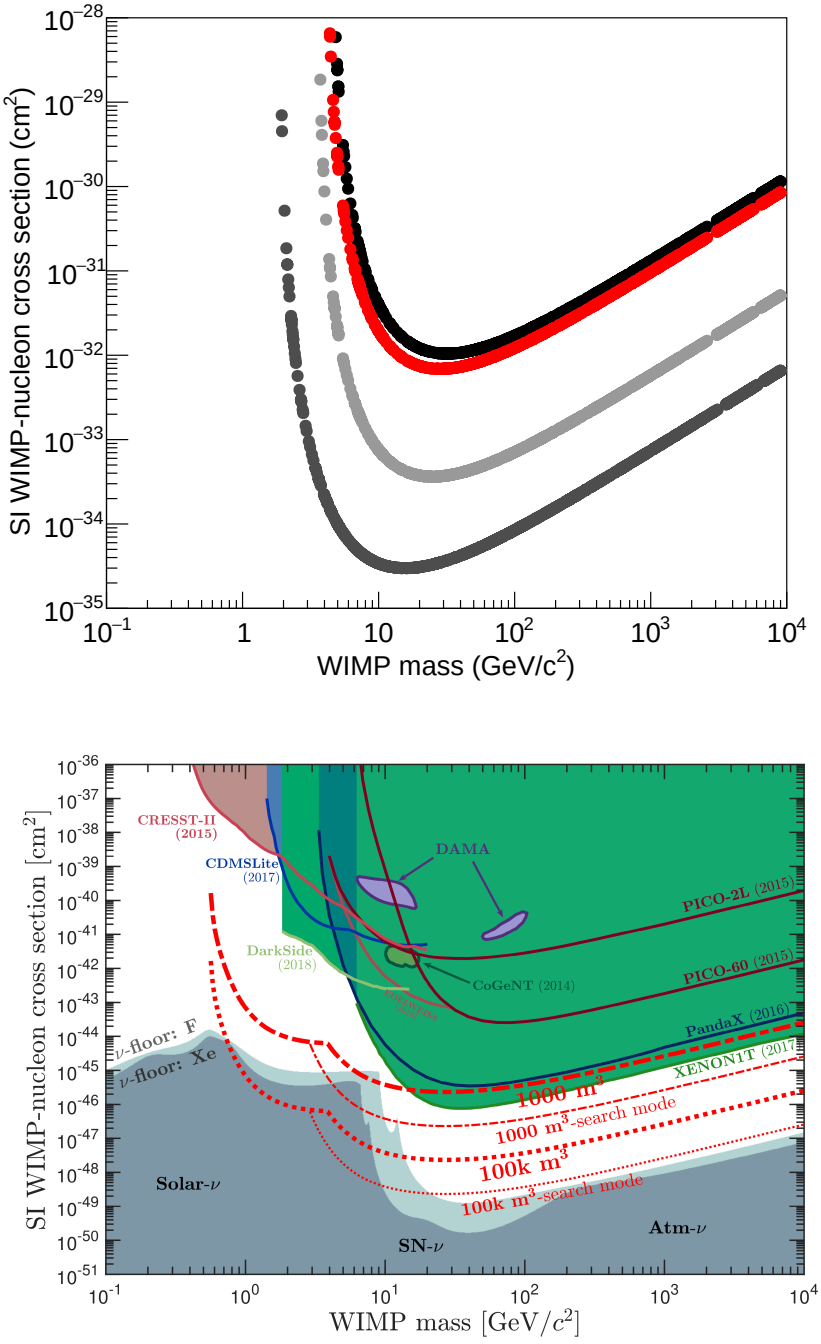

Figure 6.1: Top: Our quoted limits from Sec. 5.4.6 along with two speculative ones. Light gray: Zero background assumed with no length/energy selection applied. Dark Gray: Zero background assumed with only the edge selection applied. Bottom: Comparison of a new directional detector concept with existing limits. The red lines represent a proposed directional detector discussed in Ref. [24]. See text for discussion.

APPENDIX A
D^3 PROTOTYPES OPERATIONAL PARAMETERS

A.1 Power schemes and field cage properties

Table A.1: D^3 - prototype field cage properties; dimensions in cm.

Prototype	power scheme	cathode	ring material (shape) (count)	ring OD	ring ID	ring thickness
D^3 - Micro	single HV channel to cathode	copper mesh	N/A (N/A) (0)	N/A	N/A	N/A
D^3 - Milli1	resistive divider	copper plate	copper (circular) (4)	22.86	19.84	0.159
D^3 - Milli2 - thin	single HV channel to cathode and rings (one each)	aluminum mesh	aluminum (rectangular w/ rounded edges) (2)	6.976	5.576	0.081
D^3 - Milli2 - THGEM	resistive divider	aluminum mesh	aluminum (rectangular w/ rounded edges) (4)	6.976	5.576	0.081

A.2 Dimensions

Table A.2: D^3 - prototype dimensions (cm).

Prototype	Drift	Transfer1	Transfer2	Collection
D^3 - Micro	0.92	0.28	N/A	0.22
D^3 - Milli1 - triple	4.92	0.28	0.28	0.23
D^3 - Milli1 - THGEM	5.14	N/A	N/A	0.18
D^3 - Milli2 - thin	4.53	0.13	N/A	0.16
D^3 - Milli2 - THGEM	4.72	0.09	N/A	0.13

A.3 Data sets

Table A.3: D^3 data set descriptions. ^{55}Fe photon energy is $\approx 5.9\,keV$

Prototype	GEM scheme	Gas (proportion) (%)	Pressure (torr)	Source (energy)	Abbreviation
D^3 - Micro	double thin GEMs	$ArCO_2$ (70:30)	760	^{55}Fe	a1
D^3 - Micro	double thin GEMs	$ArCO_2$ (70:30)	760	^{210}Po ($\approx 4\,MeV$)	a2
D^3 - Micro	double thin GEMs	$HeCO_2$ (70:30)	760	^{55}Fe	h1
D^3 - Milli1	triple thin GEMs	$HeCO_2$ (70:30)	760	^{55}Fe	h2
D^3 - Milli1	single THGEM	$HeCO_2$ (70:30)	760	^{55}Fe	ht1
D^3 - Milli1	single THGEM	$HeCO_2$ (70:30)	570	^{55}Fe	ht2
D^3 - Milli1	single THGEM	$HeCO_2$ (70:30)	380	^{55}Fe	ht3
D^3 - Milli1	single THGEM	SF_6 (100)	20	^{55}Fe	s1
D^3 - Milli1	single THGEM	SF_6 (100)	40	^{55}Fe	s2
D^3 - Milli2	double thin GEMs	$HeCO_2$ (70:30)	760	^{55}Fe	h3
D^3 - Milli2	double THGEMs	$HeCO_2$ (70:30)	760	^{55}Fe	ht4

A.4 Electric fields

Table A.4: D^3 E-field values for gain study data sets defined in Tab A.3. Since the transfer and collection fields are proportional to V_{GEM}, all values are given for the highest V_{GEM} in the data set. Drift fields are held constant for gain studies.

Data set abbr.	Drift field (V/cm)	GEM field(s) 1:2:3 (kV/cm)	Reduced GEM field(s) 1:2:3 (V/cm/torr)	Transfer field(s) 1:2 (V/cm)	Collection field (V/cm)
a1	805	112 : 102	147 : 134	2935	3983
a2	882	74 : 67	97 : 88	1943	2637
h1	575	114 : 103	149 : 135	2977	4039
h2	509	74 : 75 : 75	97 : 99 : 99	1758 : 1706	2163
ht1	469	37	49	N/A	3046
ht2	291	33	58	N/A	1581
ht3	239	26	70	N/A	2160
s1	283	20	976	N/A	1594
s2	499	23	564	N/A	1842
h3	491	88 : 86	115 : 113	3383	3151
ht4	500	33 : 31	43 : 41	2465	2211

A.5 Voltages

Table A.5: D^3- prototype voltages. All values are factors of V_{GEM}.

Prototype	V_{GEM1}	$V_{transfer1}$	V_{GEM2}	$V_{transfer2}$	V_{GEM3}	$V_{collection}$
D^3 - Micro - double thin	0.52	0.77	0.48	N/A	N/A	0.82
D^3 - Milli1 - triple thin	0.33	0.44	0.34	0.43	0.33	0.44
D^3 - Mill1 - single THGEM	1.00	N/A	N/A	N/A	N/A	0.82
D^3 - Milli2 - double thin	0.50	0.50	0.49	N/A	N/A	0.60
D^3 - Milli2 - double THGEM	0.51	0.09	0.48	N/A	N/A	0.11

APPENDIX B
DRIFT FIELD STUDY

A drift field study was done with the D^3 - Milli stage 2 thin GEM setup. $HeCO_2$ at 1 atm. $V_{GEM} = 868$ for this study.

The plot on the left of figure B.1 is well described by:

$$G = 10^{a-b/V_D} \tag{B.1}$$

The plot on the right of figure B.1 is well described by:

$$\sigma_G/G = \sqrt{(c/V_D)^2 + d^2} \tag{B.2}$$

The following fit parameters are extracted:

$a = 3.702 \pm 0.005$
$b = 48 \pm 2$
$c = 4.0 \pm 0.2 \times 10^3$.
$d = 11.3 \pm 0.4$

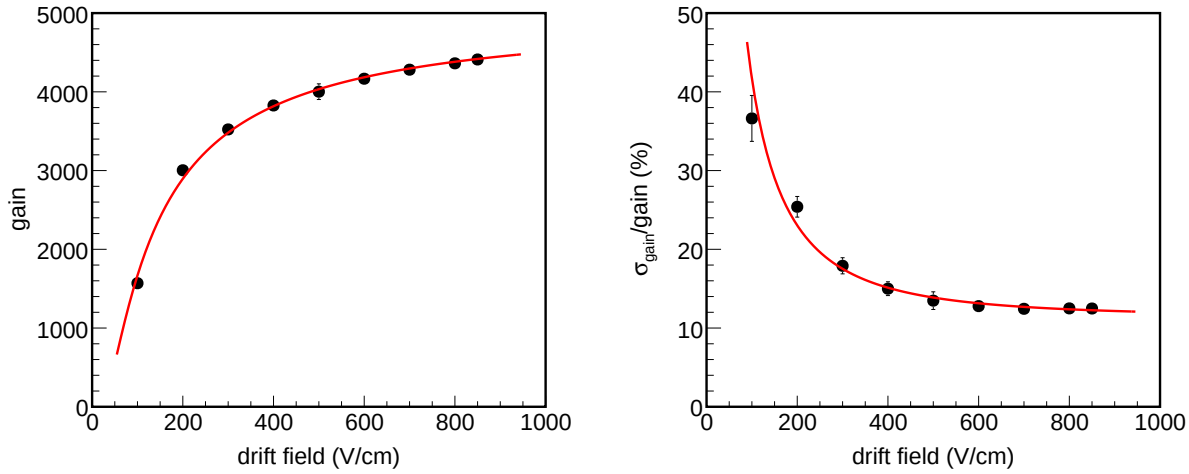

Figure B.1: Gain and resolution vs drift field for the D^3 - Milli stage 2 double GEM setup. Left: Gain vs. drift field. Right: Gain resolution vs. drift field.

APPENDIX C
AVALANCHE VARIANCE FOR OTHER GASES

Following Legler's model as with $HeCO_2$, we can compute χ and f_0 for $ArCO_2$ and SF_6.

Avalanche variance - $ArCO_2$

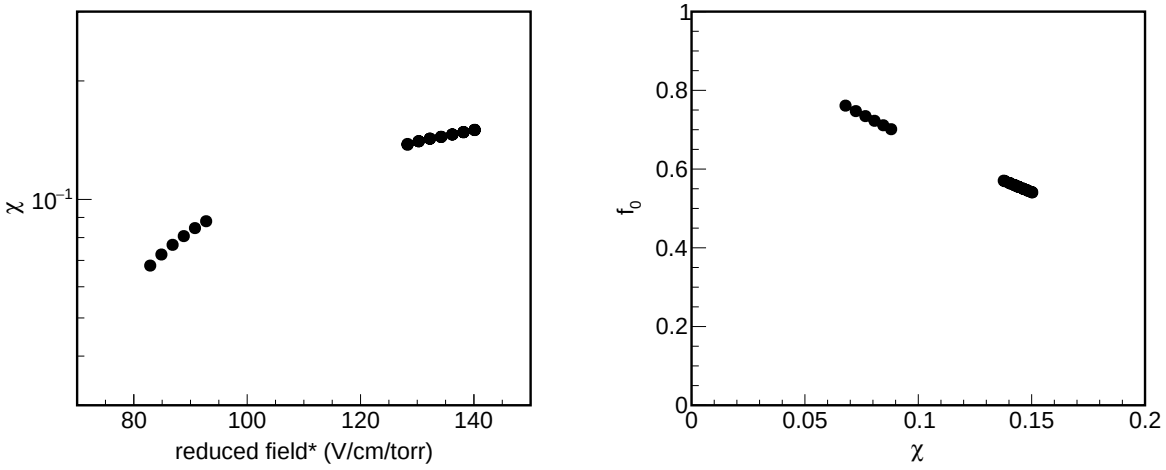

Figure C.1: Left: χ vs reduced field. Right: f_0 vs. chi. $ArCO_2$.

Avalanche variance - SF_6

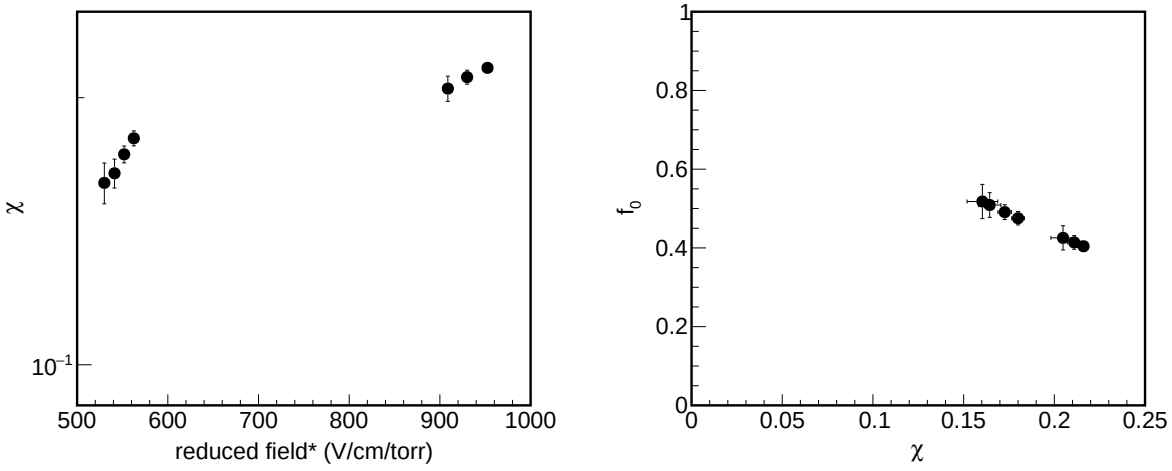

Figure C.2: Left: χ vs reduced field. Right: f_0 vs. chi. SF_6.

APPENDIX D
EXPERIMENTAL EVENTS PASSING ALL SELECTIONS

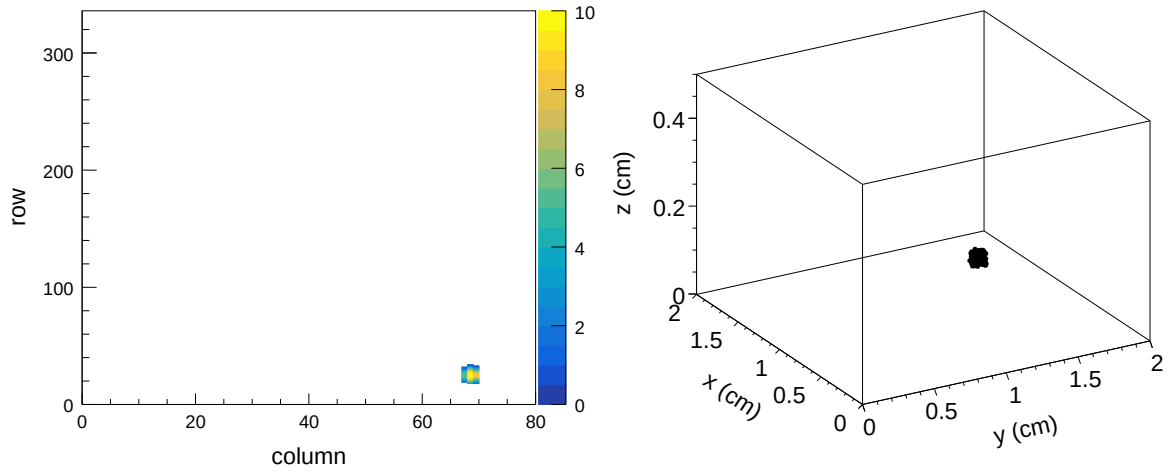

Figure D.1: Events passing all selections for a length/energy selection value of 0.0192 cm/keV.

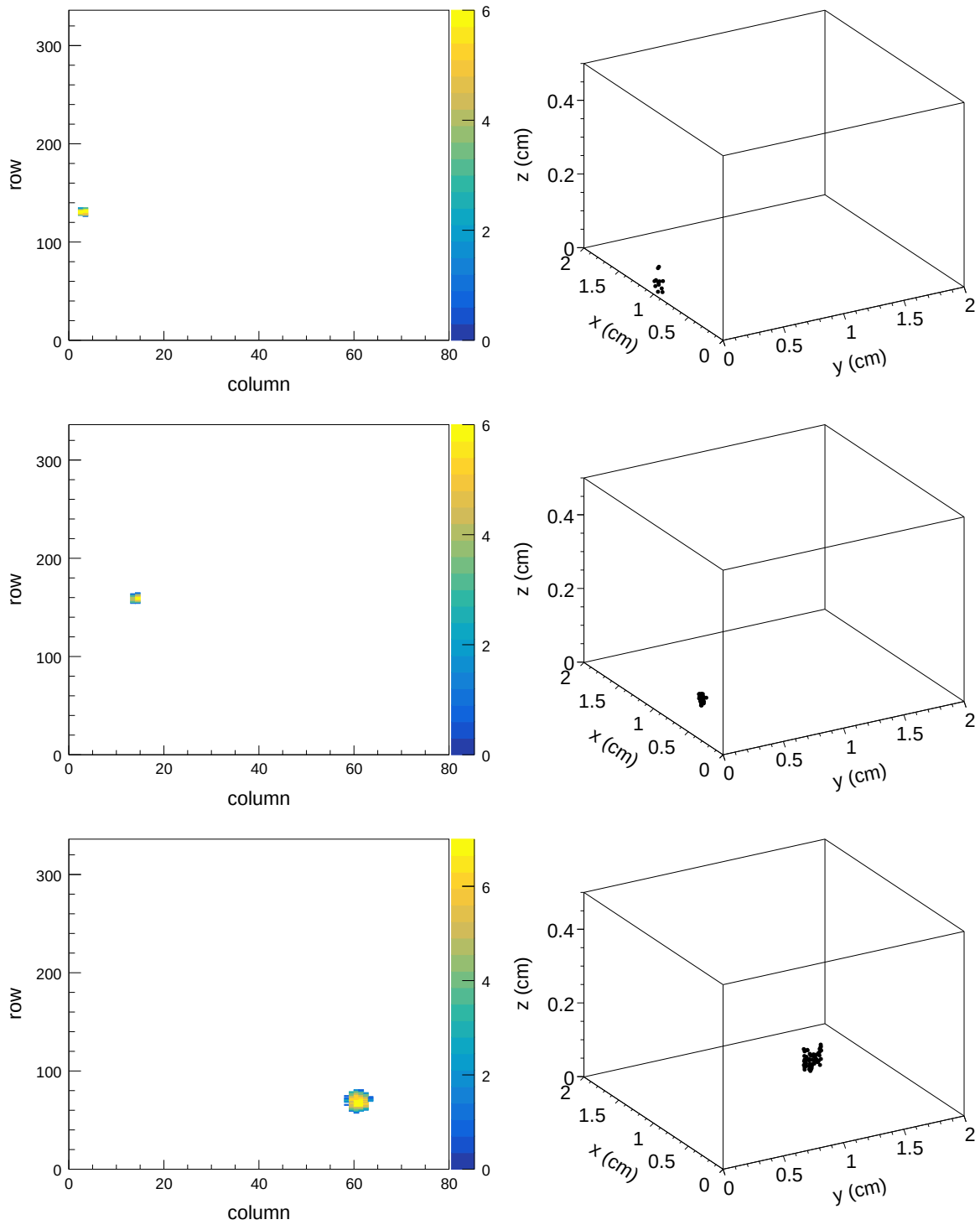

Figure D.2: Events passing all selections for a length/energy selection value of 0.0192 cm/keV.

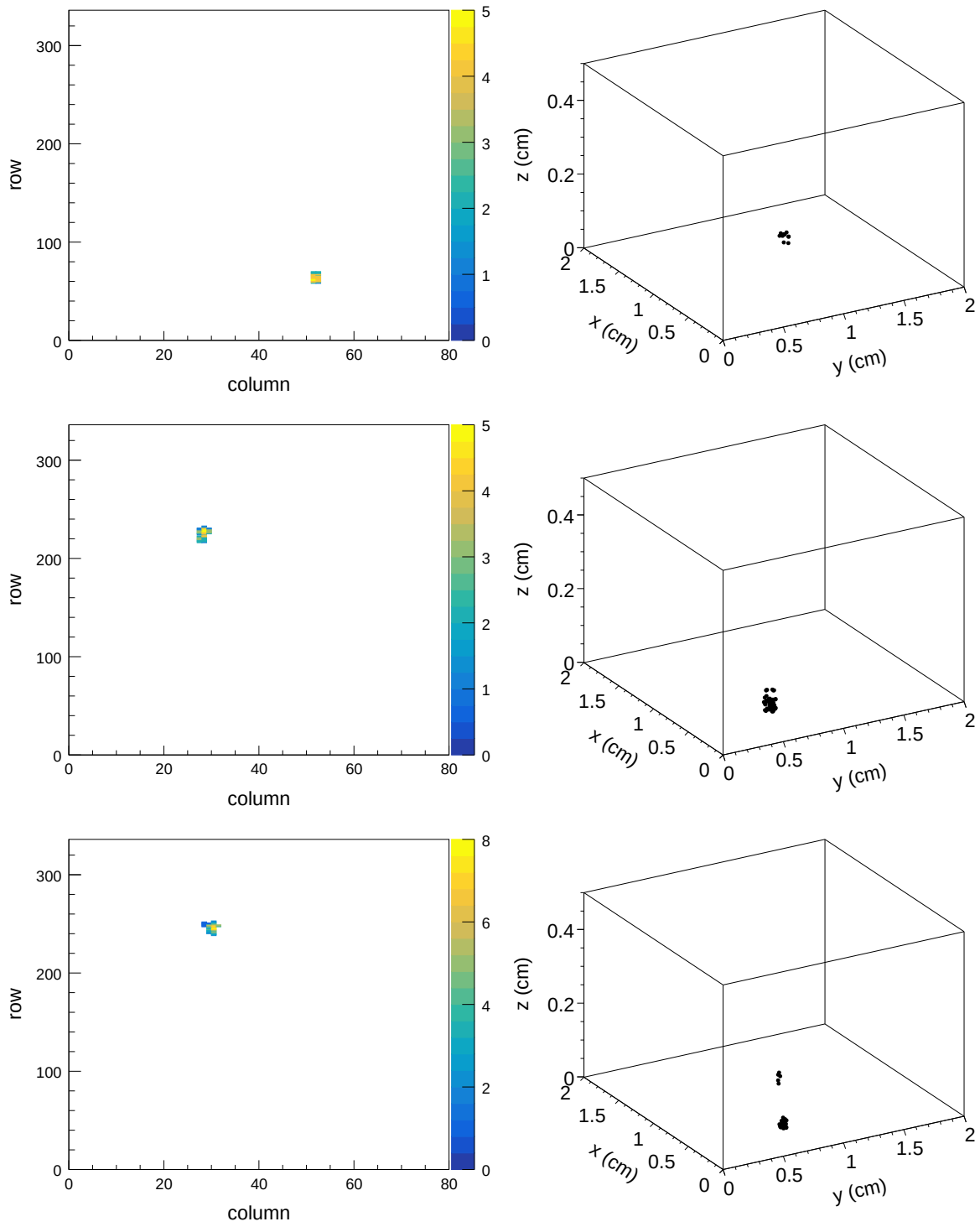

Figure D.3: Events passing all selections for a length/energy selection value of 0.0192 cm/keV.

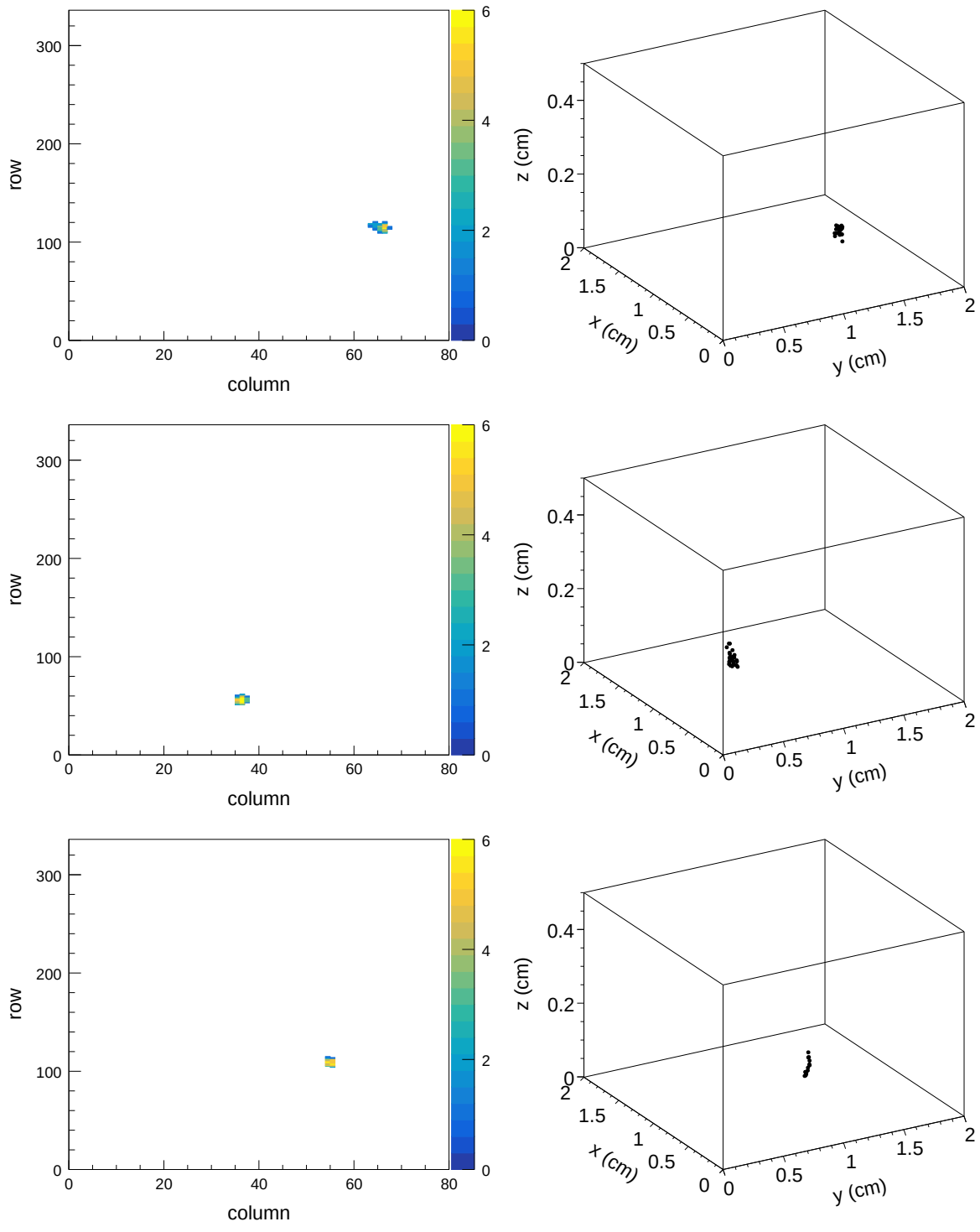

Figure D.4: Events passing all selections for a length/energy selection value of 0.0192 cm/keV.

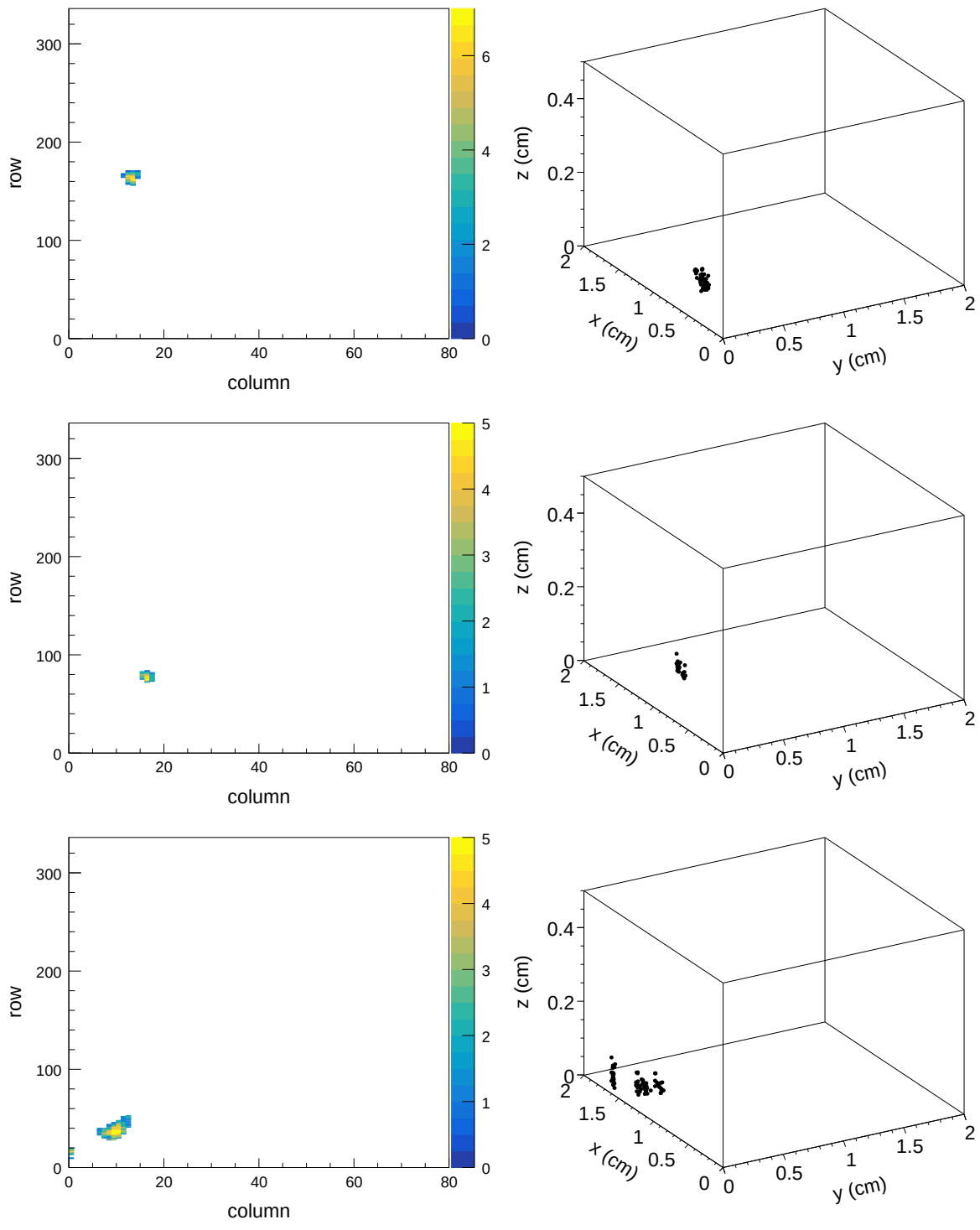

Figure D.5: Events passing all selections for a length/energy selection value of 0.0192 cm/keV.

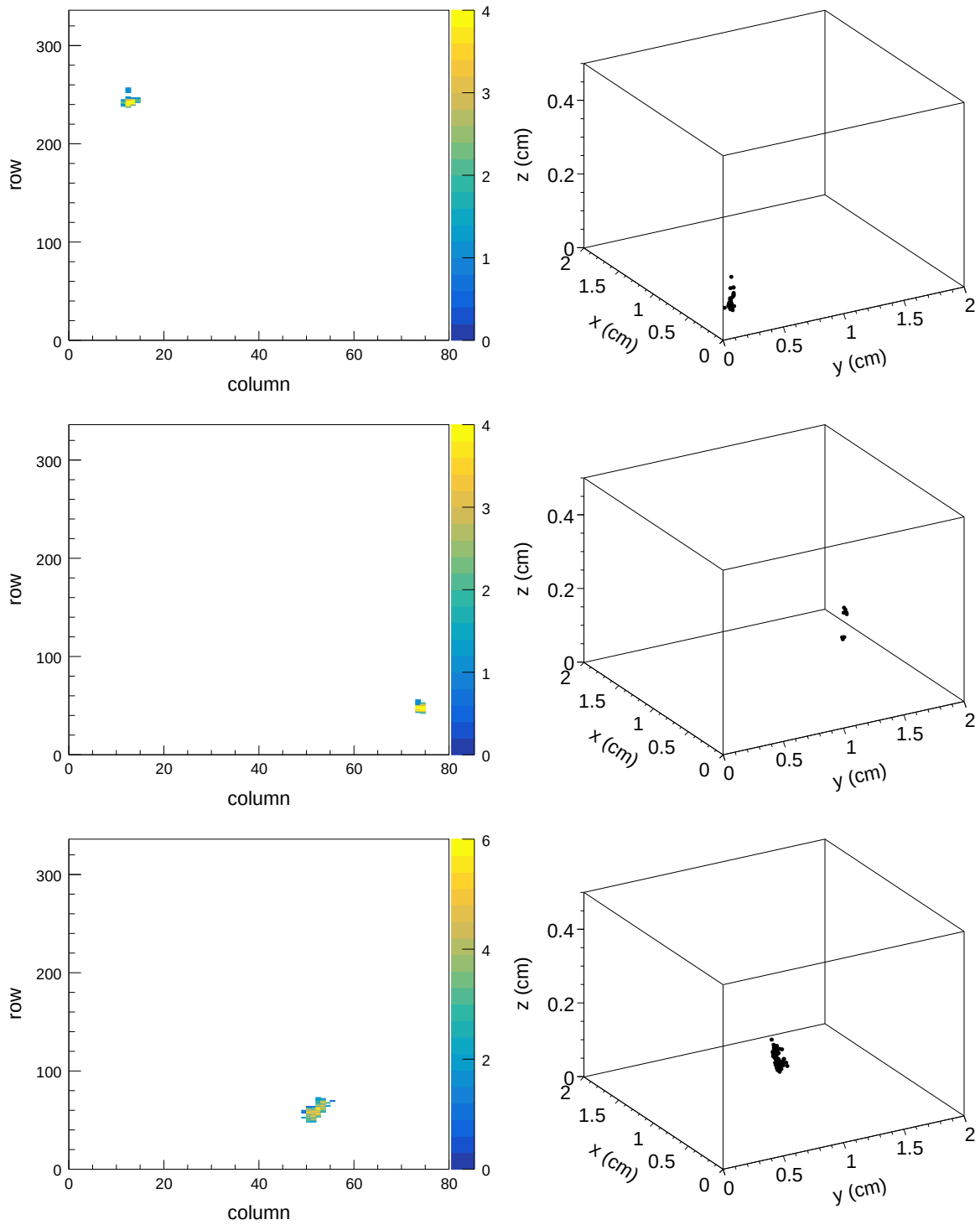

Figure D.6: Events passing all selections for a length/energy selection value of 0.0192 cm/keV.

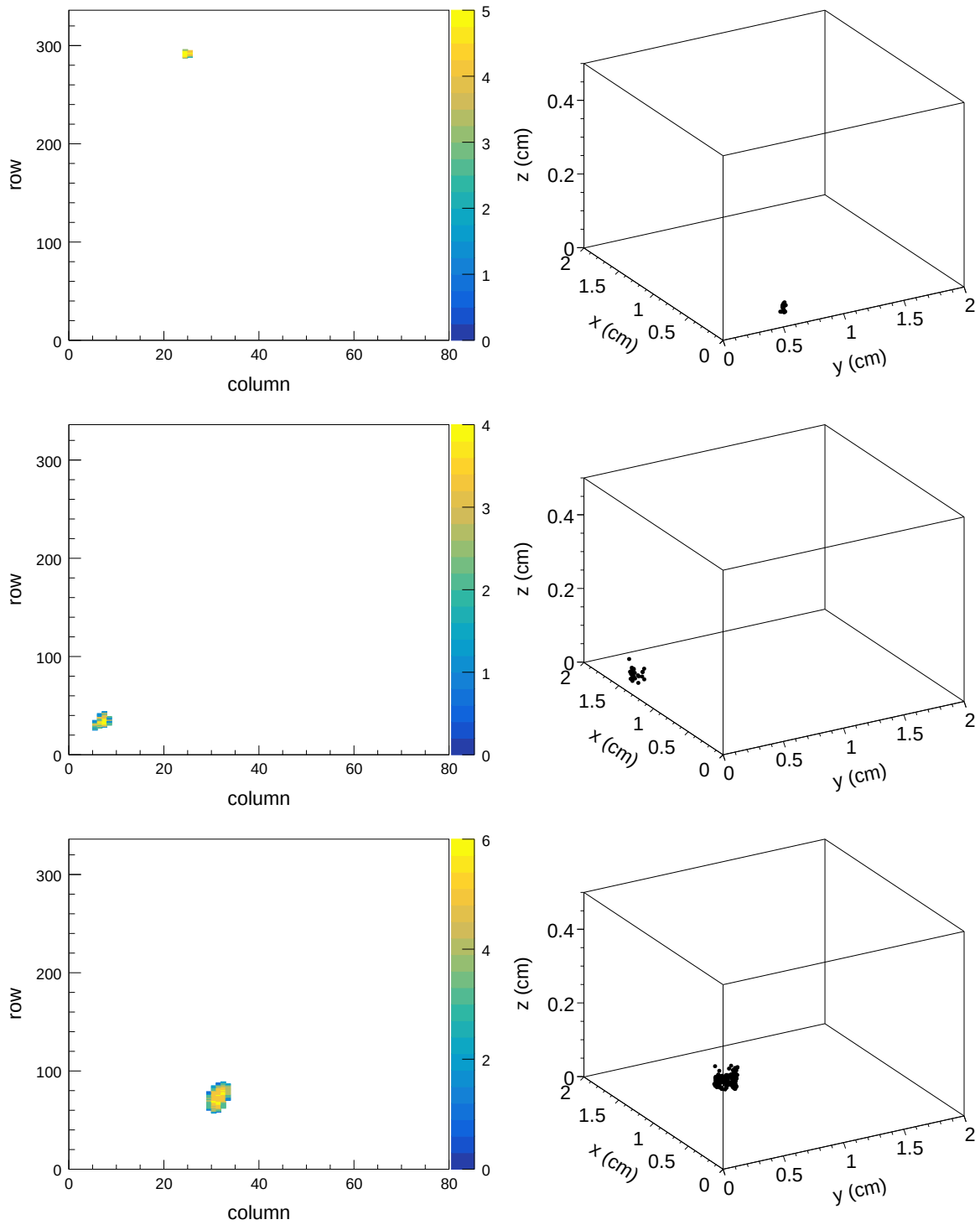

Figure D.7: Events passing all selections for a length/energy selection value of 0.0192 cm/keV.

BIBLIOGRAPHY

[1] Garfield++ webpage at CERN. https://garfieldpp.web.cern.ch/garfieldpp/.

[2] G. Aad et al. ATLAS pixel detector electronics and sensors. *JINST*, 3:P07007, 2008.

[3] C. E. Aalseth et al. DarkSide-20k: A 20 tonne two-phase LAr TPC for direct dark matter detection at LNGS. *Eur. Phys. J. Plus*, 133:131, 2018.

[4] R. P. Adak et al. Long-term stability test of a triple GEM detector. *JINST*, 11(10):T10001, 2016.

[5] P. A. R. Ade et al. Planck 2015 results. XIII. Cosmological parameters. *Astron. Astrophys.*, 594:A13, 2016.

[6] N. Aghanim et al. Planck 2018 results. VI. Cosmological parameters. 2018.

[7] R. Agnese et al. Low-mass dark matter search with CDMSlite. *Phys. Rev.*, D97(2):022002, 2018.

[8] R. Agnese et al. Results from the Super Cryogenic Dark Matter Search Experiment at Soudan. *Phys. Rev. Lett.*, 120(6):061802, 2018.

[9] S. Ahlen et al. First Dark Matter Search Results from a Surface Run of the 10-L DMTPC Directional Dark Matter Detector. *Phys. Lett.*, B695:124–129, 2011.

[10] Z. Ahmed et al. Dark Matter Search Results from the CDMS II Experiment. *Science*, 327:1619–1621, 2010.

[11] D. S. Akerib et al. Results from a search for dark matter in the complete LUX exposure. *Phys. Rev. Lett.*, 118(2):021303, 2017.

[12] D. Akimov et al. Observation of Coherent Elastic Neutrino-Nucleus Scattering. *Science*, 357(6356):1123–1126, 2017.

[13] G. D. Alkhazov. Statistics of electron avalanches and ultimate resolution of proportional counters. *Nucl. Instrum. Meth.*, 89:155–165, 1970.

[14] M. C. Altunbas, K. Dehmelt, S. Kappler, B. Ketzer, L. Ropelewski, F. Sauli, and F. Simon. Aging measurements with the gas electron multiplier (GEM). *Nucl. Instrum. Meth.*, A515:249–254, 2003. [,37(2001)].

[15] P. A. Amaudruz et al. First results from the DEAP-3600 dark matter search with argon at SNOLAB. *Phys. Rev. Lett.*, 121(7):071801, 2018.

[16] C. Amole et al. Dark Matter Search Results from the PICO-60 C_3F_8 Bubble Chamber. *Phys. Rev. Lett.*, 118(25):251301, 2017.

[17] G. Angloher, M. Bauer, I. Bavykina, A. Bento, C. Bucci, C. Ciemniak, G. Deuter, F. von Feilitzsch, D. Hauff, P. Huff, C. Isaila, J. Jochum, M. Kiefer, M. Kimmerle, J.-C. Lanfranchi, F. Petricca, S. Pfister, W. Potzel, F. Pröbst, F. Reindl, S. Roth, K. Rottler, C. Sailer, K. Schäffner, J. Schmaler, S. Scholl, W. Seidel, M. v. Sivers, L. Stodolsky, C. Strandhagen, R. Strauß, A. Tanzke, I. Usherov, S. Wawoczny, M. Willers, and A. Zöller. Results from 730 kg days of the CRESST-II Dark Matter search. *European Physical Journal C*, 72:1971, April 2012.

[18] Takahiko Aoyama. Generalized gas gain formula for proportional counters. *Nuclear Instruments and Methods in Physics Research Section A: Accelerators, Spectrometers, Detectors and Associated Equipment*, 234(1):125 – 131, 1985.

[19] E. Aprile et al. First Dark Matter Search Results from the XENON1T Experiment. *Phys. Rev. Lett.*, 119(18):181301, 2017.

[20] S. Archambault et al. Constraints on Low-Mass WIMP Interactions on ^{19}F from PICASSO. *Phys. Lett.*, B711:153–161, 2012.

[21] E. Armengaud et al. Final results of the EDELWEISS-II WIMP search using a 4-kg array of cryogenic germanium detectors with interleaved electrodes. *Phys. Lett.*, B702:329–335, 2011.

[22] E. Baracchini, G. Cavoto, G. Mazzitelli, F. Murtas, F. Renga, and S. Tomassini. Negative Ion Time Projection Chamber operation with SF_6 at nearly atmospheric pressure. *JINST*, 13(04):P04022, 2018.

[23] E. Barbosa de Souza et al. First search for a dark matter annual modulation signal with NaI(Tl) in the Southern Hemisphere by DM-Ice17. *Phys. Rev.*, D95(3):032006, 2017.

[24] J. B. R. Battat et al. CYGNUS: Feasibility of a nuclear recoil observatory with directional sensitivity to dark matter and neutrinos.

[25] J. B. R. Battat et al. First background-free limit from a directional dark matter experiment: results from a fully fiducialised DRIFT detector. *Phys. Dark Univ.*, 9-10:1–7, 2015.

[26] Laura Baudis. Direct dark matter detection: the next decade. *Phys. Dark Univ.*, 1:94–108, 2012.

[27] K. G. Begeman, A. H. Broeils, and R. H. Sanders. Extended rotation curves of spiral galaxies: Dark haloes and modified dynamics. *Mon. Not. Roy. Astron. Soc.*, 249:523, 1991.

[28] E. Behnke et al. First Dark Matter Search Results from a 4-kg CF_3I Bubble Chamber Operated in a Deep Underground Site. *Phys. Rev.*, D86(5):052001, 2012. [Erratum: Phys. Rev.D90,no.7,079902(2014)].

[29] Lars Bergstrom. Dark Matter Candidates. *New J. Phys.*, 11:105006, 2009.

[30] R Bernabei, P Belli, A Bussolotti, F Cappella, V Caracciolo, M Casalboni, R Cerulli, C J Dai, A d'Angelo, A Di Marco, H L He, A Incicchitti, H H Kuang, M Laubenstein, X H Ma, A Mattei, F Montecchia, C Palazzesi, P Prosposito, X D Sheng, R G Wang, and Z P Ye. Performances of the new high quantum efficiency pmts in dama/libra. *Journal of Instrumentation*, 7(03):P03009, 2012.

[31] R. Bernabei et al. DAMA/LIBRA results and perspectives. *Bled Workshops Phys.*, 17(2):1–7, 2016. [EPJ Web Conf.136,05001(2017)].

[32] S. Biagi. Magboltz webpage at CERN. http://magboltz.web.cern.ch/magboltz/.

[33] Walter Blum, Luigi Rolandi, and Werner Riegler. *Particle detection with drift chambers*. Particle Acceleration and Detection. 2008.

[34] Timothy D. Brandt. Constraints on MACHO Dark Matter from Compact Stellar Systems in Ultra-Faint Dwarf Galaxies. *Astrophys. J.*, 824(2):L31, 2016.

[35] K. Broni. W values and Fano factors for electrons in rare gases and rare gas mixtures. *Ionizing Radiation (Hoshasen)*, 1998.

[36] J. Bryne. Statistics of electron avalanches in the Proportional Counter. *Nucl. Instrum. Meth.*, 1962.

[37] L. M. Capparelli, G. Cavoto, D. Mazzilli, and A. D. Polosa. Directional Dark Matter Searches with Carbon Nanotubes. *Phys. Dark Univ.*, 9-10:24–30, 2015. [Erratum: Phys. Dark Univ.11,79(2016)].

[38] Riccardo Catena. Dark matter directional detection in non-relativistic effective theories. *JCAP*, 1507(07):026, 2015.

[39] Douglas Clowe, Marusa Bradac, Anthony H. Gonzalez, Maxim Markevitch, Scott W. Randall, Christine Jones, and Dennis Zaritsky. A direct empirical proof of the existence of dark matter. *Astrophys. J.*, 648:L109–L113, 2006.

[40] The FE-I4B Collaboration. The FE-I4B Integrated Circuit Guide. https://indico.cern.ch/event/261840/contributions/1594374/attachments/462649/641213/FE-I4B_V2.3.pdf

[41] Xiangyi Cui et al. Dark Matter Results From 54-Ton-Day Exposure of PandaX-II Experiment. *Phys. Rev. Lett.*, 119(18):181302, 2017.

[42] Nicola D'Ambrosio et al. Nuclear emulsions as a very high resolution detector for directional dark matter search. *JINST*, 9(01):C01043, 2014.

[43] Yuri I. Davydov. On the first Townsend coefficient at high electric field. *IEEE Trans. Nucl. Sci.*, 53:2931–2935, 2006.

[44] E. Daw et al. The DRIFT Directional Dark Matter Experiments. *EAS Publ. Ser.*, 53:11–18, 2012.

[45] Ward Diethorn. *A methane proportional counter system for natural radiocarbon measurements*. United States Atomic Energy Commission, Technical Information Service, 03 1956.

[46] Andrzej Drukier, Katherine Freese, Alejandro Lopez, David Spergel, Charles Cantor, George Church, and Takeshi Sano. New Dark Matter Detectors using DNA or RNA for Nanometer Tracking. 2012.

[47] D. Dujmic et al. Observation of the 'head-tail' effect in nuclear recoils of low-energy neutrons. *Nucl. Instrum. Meth.*, A584:327–333, 2008. [Erratum: Nucl. Instrum. Meth.A592,123(2008)].

[48] A.von Engel. *Ionized Gases*. AIP-Press, 01 1994.

[49] J. Engel, S. Pittel, and P. Vogel. Nuclear physics of dark matter detection. *Int. J. Mod. Phys.*, E1:1–37, 1992.

[50] G F. Knoll. *Radiation Detection and Measurement*. New York, John Wiley and Sons, Inc., 1979. 831 p., 01 2000.

[51] M Felizardo, T A Girard, T Morlat, A C Fernandes, A R Ramos, and J G Marques. Recent results from the simple dark matter search. *Journal of Physics: Conference Series*, 375(1):012011, 2012.

[52] Jonathan L. Feng. Dark Matter Candidates from Particle Physics and Methods of Detection. *Ann. Rev. Astron. Astrophys.*, 48:495–545, 2010.

[53] A. Liam Fitzpatrick, Wick Haxton, Emanuel Katz, Nicholas Lubbers, and Yiming Xu. The Effective Field Theory of Dark Matter Direct Detection. *JCAP*, 1302:004, 2013.

[54] Katherine Freese, Brian Fields, and David Graff. Limits on stellar objects as the dark matter of our halo: nonbaryonic dark matter seems to be required. *Nucl. Phys. Proc. Suppl.*, 80:0305, 2000.

[55] Paolo Gondolo. Recoil momentum spectrum in directional dark matter detectors. *Phys. Rev.*, D66:103513, 2002.

[56] Anne M Green. Astrophysical uncertainties on the local dark matter distribution and direct detection experiments. *J. Phys.*, G44(8):084001, 2017.

[57] Kim Griest, Agnieszka M. Cieplak, and Matthew J. Lehner. Experimental Limits on Primordial Black Hole Dark Matter from the First 2 yr of Kepler Data. *Astrophys. J.*, 786(2):158, 2014.

[58] Michael Hedges. *Performance and First Deployment of Novel 3D Nuclear Recoil Detectors*. PhD thesis, Hawaii, U., 2018-12.

[59] Y H Hilal and L G Christophorou. The energy to produce an electron-ion pair in sf 6 and sf 6 /n 2 gas mixtures. *Journal of Physics D: Applied Physics*, 20(7):975, 1987.

[60] Ikeda, Tomonori, Miuch, Kentaro, Ochi, Atsuhiko, Yakabe, Ryota, Hashimoto, Takashi, Taishaku, Ryosuke, Snowden-Ifft, Daniel P., Gauvreau, Jean-Luc, Tanimori, Toru, Takada, Atsushi, and Nakamura, Kiseki. Study of negative-ion tpc using for directional dark matter search. *EPJ Web Conf.*, 174:02006, 2018.

[61] P. Biersack J. F. Ziegler. The stopping and range of ions in matter. Pergamon Press, New York, http://www.srim.org/.

[62] I. Jaegle et al. Design and production of the BEAST microTPC directional neutron detectors, publication in preparation.

[63] Gerard Jungman, Marc Kamionkowski, and Kim Griest. Supersymmetric dark matter. *Phys. Rept.*, 267:195–373, 1996.

[64] Bradley J. Kavanagh. New directional signatures from the nonrelativistic effective field theory of dark matter. *Phys. Rev.*, D92(2):023513, 2015.

[65] T. Kim, M. Freytsis, J. Button-Shafer, J. Kadyk, S.E. Vahsen, and W.A. Wenzel. Readout of tpc tracking chambers with gems and pixel chip. *Nuclear Instruments and Methods in Physics Research Section A: Accelerators, Spectrometers, Detectors and Associated Equipment*, 589(2):173 – 184, 2008.

[66] M. Kimura and T. Naka. Submicron track readout in fine-grained nuclear emulsions using optical microscopy. *Nucl. Instrum. Meth.*, A680:12–17, 2012.

[67] J.T. Knipple. NASA materials outgassing site. https://outgassing.nasa.gov/.

[68] Adam Latosinski, Krzysztof A. Meissner, and Hermann Nicolai. Axions without Peccei-Quinn Symmetry. 2010.

[69] W. Legler. Die Statistik der Elektronenlawinen in eleltronegativen Gasen, bei hohen Feldstärken und bei großer Gasverstärkung. *Zeitschrift Naturforschung Teil A*, 16:253–261, March 1961.

[70] J. D. Lewin and P. F. Smith. Review of mathematics, numerical factors, and corrections for dark matter experiments based on elastic nuclear recoil. *Astropart. Phys.*, 6:87–112, 1996.

[71] P. M. Lewis et al. First Measurements of Beam Backgrounds at SuperKEKB. 2018.

[72] P. M. Lewis, S. E. Vahsen, I. S. Seong, M. T. Hedges, I. Jaegle, and T. N. Thorpe. Absolute Position Measurement in a Gas Time Projection Chamber via Transverse Diffusion of Drift Charge. *Nucl. Instrum. Meth.*, A789:81–85, 2015.

[73] Hao Liu and Ti-Pei Li. Improved CMB Map from WMAP Data. *arXiv e-prints*, page arXiv:0907.2731, July 2009.

[74] Jianglai Liu, Xun Chen, and Xiangdong Ji. Current status of direct dark matter detection experiments. *Nature Phys.*, 13(3):212–216, 2017.

[75] I Lopes, H Hilmert, and W F Schmidt. Ionisation of gaseous and liquid sulphur hexafluoride by 60 co -radiation. *Journal of Physics D: Applied Physics*, 19(6):L107, 1986.

[76] Jay N. Marx and David R. Nygren. The Time Projection Chamber. *Phys. Today*, 31N10:46–53, 1978.

[77] F. Mayet et al. Measurement of the electron drift velocity for directional dark matter detectors. *J. Phys. Conf. Ser.*, 469:012006, 2013.

[78] F. Mayet et al. A review of the discovery reach of directional Dark Matter detection. *Phys. Rept.*, 627:1–49, 2016.

[79] F. Mayet, O. Guillaudin, C. Grignon, C. Koumeir, D. Santos, P. Colas, and I. Giomataris. Micromegas μTPC for direct Dark Matter search with MIMAC. In *Journal of Physics Conference Series*, volume 179 of *Journal of Physics Conference Series*, page 012011, July 2009.

[80] Ben Morgan, Anne M. Green, and Neil J. C. Spooner. Directional statistics for WIMP direct detection. *Phys. Rev.*, D71:103507, 2005.

[81] K. Nakamura et al. Low pressure gas study for a direction-sensitive dark matter search experiment with MPGD. *JINST*, 7:C02023, 2012.

[82] David Nygren. personal communication.

[83] Ciaran A.?J. O'Hare, Christopher McCabe, N. Wyn Evans, GyuChul Myeong, and Vasily Belokurov. Dark matter hurricane: Measuring the S1 stream with dark matter detectors. *Phys. Rev.*, D98(10):103006, 2018.

[84] M. Oreglia. *A Study of the Reactions $\psi' \to \gamma\gamma\psi$*. PhD thesis, SLAC, 1980.

[85] C. Patrignani et al. Review of Particle Physics. *Chin. Phys.*, C40(10):100001, 2016.

[86] R. D. Peccei and Helen R. Quinn. CP Conservation in the Presence of Instantons. *Phys. Rev. Lett.*, 38:1440–1443, 1977. [,328(1977)].

[87] N. S. Phan, R. Lafler, R. J. Lauer, E. R. Lee, D. Loomba, J. A. J. Matthews, and E. H. Miller. The novel properties of SF_6 for directional dark matter experiments. *JINST*, 12(02):P02012, 2017.

[88] John Preskill, Mark B. Wise, and Frank Wilczek. Cosmology of the Invisible Axion. *Phys. Lett.*, B120:127–132, 1983. [,URL(1982)].

[89] Surjeet Rajendran, Nicholas Zobrist, Alexander O. Sushkov, Ronald Walsworth, and Mikhail Lukin. A method for directional detection of dark matter using spectroscopy of crystal defects. *Phys. Rev.*, D96(3):035009, 2017.

[90] D Santos, J Billard, G Bosson, J L Bouly, O Bourrion, Ch Fourel, C Grignon, O Guillaudin, F Mayet, J P Richer, A Delbart, E Ferrer, I Giomataris, F J Iguaz, J P Mols, C Golabek, and L Lebreton. Mimac: A micro-tpc matrix for directional detection of dark matter. *Journal of Physics: Conference Series*, 309(1):012014, 2011.

[91] F. Sauli. GEM: A new concept for electron amplification in gas detectors. *Nucl. Instrum. Meth.*, A386:531–534, 1997.

[92] F. Sauli. Gaseous detectors fundamentals - edit 2011 conference presentation, 31 Jan. - 10 Feb. 2011.

[93] Andrew Scarff. *Developments Towards a Scaled-Up One-Dimensional Directional Dark Matter Detector*. PhD thesis, Sheffield U., 2017-11.

[94] H. Schlumbohm. Zur Statistik der Elektronenlawinen im ebenen Feld. III. *Zeitschrift fur Physik*, 151:563–576, October 1958.

[95] G Sciolla and C J Martoff. Gaseous dark matter detectors. *New Journal of Physics*, 11(10):105018, 2009.

[96] Ilsoo Seong. *Search for a Light Higgs Boson and Low Mass Dark Matter at the Belle Experiment*. PhD thesis, Hawaii, U., 2017-07.

[97] A. Sharma. Gaseous detectors: Then and now. *NATO Sci. Ser. II*, 123:273–339, 2003.

[98] Archana Sharma. Properties of some gas mixtures used in tracking detectors. 1998.

[99] A. Siebert. Status and results from the RAVE survey. 2012.

[100] J. Silk et al. *Particle Dark Matter: Observations, Models and Searches*. Cambridge Univ. Press, Cambridge, 2010.

[101] D. P. Snowden-Ifft, C. J. Martoff, and J. M. Burwell. Low pressure negative ion time projection chamber for dark matter search. *Phys. Rev. D*, 61:101301, Apr 2000.

[102] Peter Sorensen, Mike Heffner, Adam Bernstein, Josh Renner, and Melinda Sweany. Towards energy resolution at the statistical limit from a negative ion time projection chamber. *Nucl. Instrum. Meth.*, A686:106–111, 2012.

[103] David N. Spergel. Motion of the earth and the detection of weakly interacting massive particles. *Phys. Rev. D*, 37:1353–1355, Mar 1988.

[104] Patrick Stengel. personal communication.

[105] M. Tanabashi et al. Review of Particle Physics. *Phys. Rev.*, D98(3):030001, 2018.

[106] Toru Tanimori, Hidetoshi Kubo, Kentaro Miuchi, Tsutomu Nagayoshi, Reiko Orito, Atsushi Takada, and Atsushi Takeda. Detecting the wimp-wind via spin-dependent interactions. *Phys. Lett.*, B578:241–246, 2004.

[107] T. Uchida and M. Tanaka. Development of tcp/ip processing hardware. In *2006 IEEE Nuclear Science Symposium Conference Record*, volume 3, pages 1411–1414, Oct 2006.

[108] S. E. Vahsen, M. T. Hedges, I. Jaegle, S. J. Ross, I. S. Seong, T. N. Thorpe, J. Yamaoka, J. A. Kadyk, and M. Garcia-Sciveres. 3-D tracking in a miniature time projection chamber. *Nucl. Instrum. Meth.*, A788:95–105, 2015.

[109] Jui-Jen Wang. MiniCLEAN Dark Matter Experiment. 2017.

[110] A. Williams and R.I. Sara. Parameters affecting the resolution of a proportional counter. *The International Journal of Applied Radiation and Isotopes*, 13(5):229 – 238, 1962.

[111] Alex Wright. The DarkSide Program at LNGS. In *Particles and fields. Proceedings, Meeting of the Division of the American Physical Society, DPF 2011, Providence, USA, August 9-13, 2011*, 2011.

[112] S. Yellin. Finding an upper limit in the presence of an unknown background. *Phys. Rev. D*, 66:032005, Aug 2002.

[113] F. Zwicky. Die Rotverschiebung von extragalaktischen Nebeln. *Helv. Phys. Acta*, 6:110–127, 1933. [Gen. Rel. Grav.41,207(2009)].